

Phenomenological modelling and simulation of ferroelectric ceramics

von der Fakultät Maschinenbau
der Technischen Universität Dortmund
zur Erlangung des akademischen Grades

Doktor-Ingenieur (Dr.-Ing.)

genehmigte Dissertation

von

Maniprakash Subramanian

aus Thoothukudi

Referent:	Prof. Dr.-Ing. A. Menzel
Korreferenten:	Prof. Dr.-Ing. A. Arockiarajan Jun-Prof. B. Kiefer, Ph.D.
Tag der Einreichung:	25.11.2015
Tag der mündlichen Prüfung:	15.03.2016

© Maniprakash Subramanian 2016

This work is subject to copyright. All rights are reserved, whether the whole or part of the material is concerned, specifically the rights of translation, reprinting, reuse of illustrations, recitation, broadcasting, reproduction on microfilm or in any other way, and storage in data banks. Duplication of this publication or parts thereof is permitted in connection with reviews or scholarly analysis. Permission for use must always be obtained from the author.

Alle Rechte vorbehalten, auch das des auszugsweisen Nachdrucks, der auszugsweisen oder vollständigen Wiedergabe (Photographie, Mikroskopie), der Speicherung in Datenverarbeitungsanlagen und das der Übersetzung.

“No man should escape our universities without knowing how little he knows.”

J. Robert Oppenheimer

Acknowledgements

*“Assistance given by those who ne’er received our aid,
Is debt by gift of heaven and earth but poorly paid”*

Thiruvalluvar

I would like to express my sincere and deep gratitude to my advisor Professor Andreas Menzel. Without his consistent motivation and guidance, the presented work would not be achievable. His patience and supporting character are not just helpful in the success of this thesis, but also a contribution to my life lessons.

Furthurmore, I would like to thank Professor A. Arockiarajan for his generosity in providing time and source for the contribution of experimental investigation in this work. In this collaborative research, his provisions on experimental data were consistent with the schedule which motivates me to cope up with the timetable. I also thank him for agreeing to act as the co-referee. And I would like to thank Professor B. Kiefer for serving as the third referee. I also would like to thank Professor Ralf Denzer for the fruitful discussions I had with him. His creative suggestions were very helpful for my work. And I would like to express my gratitude to my guru, Professor M. S. Sivakumar, who always inspired me to run towards my interests.

Next, I would like to thank all my colleagues at the Institute of Mechanics and all my friends for their help and delightful company. Specially, I wish to acknowledge the timely administrative help extended by Kerstin Walter and outstanding assistance in proof-reading various manuscripts by Christina McDonagh. I would like to thank Matthias Weiss for all his help. Special thanks to my room-mate Rolf Berthelsen and my wing-mate Dinesh Kumar for all their help throughout my stay in Dortmund. I am thankful to Dr. Jayabal Kaliappan for his assistance in the initial days of my work. I am also grateful to Dr. R. Jayendiran and Y. Mohan for helping on getting the experimental results presented in this dissertation. In addition, I would like to gratefully acknowledge the financial support by the NRW Graduate School of Energy Efficient Production and Logistics and partial financial support by the German Research Foundation (DFG).

I am truly grateful to my father P. Subramanian and my mother S. Manimegalai for their eternal love and support.

Dortmund, March 2016

Maniprakash Subramanian

Zusammenfassung

In dieser Arbeit werden vier verschiedene phänomenologische Modelle zur Beschreibung des Verhaltens ferroelektrischer Materialien vorgestellt, im Rahmen der Finiten Elemente Methode eingebunden und anhand repräsentativer numerischer Beispiele validiert. Das erste Modell dient zur Erfassung der ratenabhängigen dielektrischen Hysterese- und Schmetterlingskurve von Ferroelektrika. Die zugehörigen Materialparameter werden mit Hilfe experimenteller Daten kalibriert. Bei dem zweiten Ansatz handelt es sich um ein „multi-surface“ Modell, welches kleine und große Hystereseschleifen sowie asymmetrische Schmetterlingskurven abbilden kann. Die Auswirkung von äußeren mechanischen Lasten auf die beiden Hysterese- und Schmetterlingskurven wird im dritten Modell untersucht. Dabei stehen ferroelastische Hysterese- und Schmetterlingskurven, mechanische Depolarisation und anisotrope Umklappvorgänge im Fokus. Thermische Depolarisation und antiferroelektrisches Hystereseverhalten werden im vierten Modell betrachtet. Abschließend wird das erste Modell zur Simulation von ferroelektrischen Kompositen verwendet. Dabei wird sowohl ein einfacher Homogenisierungsansatz als auch ein Finite Elemente basierter Ansatz vorgestellt. Numerische Simulationsergebnisse beider Zugänge werden bei verschiedenen elektrischen Anregungsfrequenzen mit experimentellen Daten und untereinander verglichen.

Abstract

In this work, four different phenomenological models are introduced and related simulation results are presented. The models are developed such that these can be implemented in a finite element framework. The first model captures rate dependent ferroelectric behaviour of dielectric hysteresis and butterfly hysteresis at different loading rates. The material parameters of the model are calibrated based on experimental data. In the second model, a multi-surface approach is established in order to calculate minor and major ferroelectric hysteresis loops as well as asymmetric butterfly hysteresis. The third model captures the effects of external stresses on ferroelectric hysteresis. In addition to that, the model is also formulated to capture the ferroelastic hysteresis, mechanical depolarisation as well as anisotropic switching behaviour. To capture the thermal depolarisation behaviour as well as antiferroelectric hysteresis, another model is introduced and further simulation results are presented. To extent the ferroelectric models to capture the effective behaviour of ferroelectric composites, a simple homogenisation

approach is applied. Following that, a finite element homogenisation approach is used to obtain the effective behaviour of ferroelectric composites. Thereafter, the experimental data for piezocomposites at different electrical loading frequencies and the results obtained for both simulation approaches are compared.

Publications

The following peer-reviewed journal articles were submitted during the progress of this thesis and essentially contribute to this thesis. The original articles are partially modified wherever it is considered meaningful, for instance, to indicate interconnections, to specify details and avoid unnecessary repetitions.

Chapter 3 and 7: S. Maniprakash, R. Jayendiran, A. Menzel, A. Arockiarajan: *Experimental investigation, modelling and simulation of 1-3 ferrocomposites*, Mechanics of Materials, 94:91–105, 2016.

Chapter 4: S. Maniprakash, A. Arockiarajan, A. Menzel: *A Multi-surface model for ferroelectric ceramics - application to cyclic electric loading with changing maximum amplitude*, Philosophical Magazine, 2016. doi:10.1080/14786435.2016.1161861.

The articles were prepared in collaboration with two and three co-authors. The author of this thesis contributed essential aspects with regard to the outline of the theory, carried out the numerical implementation and simulations completely, performed the experimental investigation presented in chapter 4 and contributed essential parts to the preparation of all of the papers listed above. All the experimental investigations in this work were performed at the Department of Applied Mechanics at the Indian Institute of Technology Madras.

Contents

1	Introduction	3
1.1	Smart materials	3
1.2	Piezoelectric materials	3
1.3	Linear piezoelectric behaviour	5
1.4	Linear three-dimensional constitutive relations	6
1.5	Non-linear ferroelectric behaviour	7
1.5.1	Dielectric hysteresis	9
1.5.2	Butterfly hysteresis	10
1.5.3	Mechanical depolarisation	10
1.5.4	Rate dependent behaviour	12
1.5.5	Thermal effects	12
1.6	Ferroelectric composites	13
1.6.1	1-3 composites	14
1.7	Motivation for this work	15
1.8	Notation	16
2	Literature review	17
2.1	Experimental studies	17
2.2	Ferroelectric constitutive models	19
2.2.1	Micromechanical models	20
2.2.2	Phenomenological models	21
2.3	Models for piezocomposites	24
2.4	Motivation and scope based on the literature review	26
2.5	Organisation of the work	27
3	A single surface model for ferroelectric ceramics	29
3.1	Fundamental governing equations	29
3.1.1	Balance of linear momentum	29
3.1.2	Balance of electric charges	30
3.2	Thermodynamic framework of constitutive modelling	30
3.2.1	Strain driven model	31
3.2.2	Stress driven model	32
3.3	Constitutive model for bulk PZT	33
3.4	Results	36
3.5	Summary and conclusions	40

4	A multi-surface model for ferroelectric ceramics	41
4.1	Motivation for multi-surface model and experimental data	41
4.2	Constitutive model	43
4.2.1	Energy functions and flux terms	45
4.2.2	Evolution equations of internal variables	46
4.2.3	Graphical illustration of the multi-surface model	47
4.3	Simulation of ferroelectric behaviour	51
4.3.1	Parameter identification based on experimental data for ferroelectric hysteresis at different loading levels	51
4.3.2	Simulation of decaying offset polarisation of an electrically fatigued specimen	52
4.3.3	Polarisation rotation test	54
4.4	Summary and conclusion	54
5	An anisotropic switching model including external stress effects	63
5.1	Thermodynamical modelling framework	63
5.1.1	Ferroelastic switching	64
5.1.2	Ferroelectric switching and mechanical depolarisation	65
5.1.3	Irreversible part of the free energy	66
5.1.4	Integration algorithm	66
5.2	Numerical results	66
5.2.1	Purely electrical loading	68
5.2.2	Purely mechanical loading	68
5.2.3	Electromechanical loading	71
5.2.4	Polarisation rotation	72
5.3	Summary and conclusion	72
6	A temperature dependent model for ferroelectric ceramics	75
6.1	Introduction	75
6.2	Constitutive model	75
6.2.1	Energy and flux terms	76
6.2.2	Evolution of internal variable	76
6.2.3	Dissipation inequality	77
6.3	Numerical simulation of ferroelectric behaviour	78
6.3.1	Hardening function	79
6.3.2	Results	79
6.4	Temperature dependent ferroelectric model	82
6.4.1	Hardening function	82
6.4.2	Numerical simulation of thermal depolarisation	82
6.4.3	Simulation of ferroelectric hysteresis	83
6.5	Summary and conclusion	83
7	Simulation of 1-3 piezocomposites	85

7.1	Homogenisation methods	85
7.1.1	Voigt assumption	85
7.1.2	Reuss assumption	86
7.1.3	Simple homogenisation approach	87
7.2	Homogenisation algorithm for nonlinear behaviour	88
7.3	Finite element homogenisation procedure	89
7.4	Simulation results	90
7.5	A comparative study between two approaches	94
7.6	Summary and conclusion	95
8	Summary and future work	97
A	Notes on the finite element formulation	99
	Bibliography	101

1 Introduction

1.1 Smart materials

Among various materials around us, there are few which are distinguished due to their special behaviours. For example, shape memory alloys change their crystal structures with respect to the temperature, resulting in a changing shape of the material from a macroscopic viewpoint. This shape change in the material could be designed such as to have a mechanical actuation and could thus be used as a solid state heat engine as it converts heat energy into mechanical energy. This unique behaviour can be used in applications such as civil structures, robotics, etc. [58]. The same material under different ambient temperature condition could recover a mechanical strain of more than 10% which is known as super-elastic behaviour. This behaviour is also known as pseudoelastic behaviour due to the existence of hysteresis loops in the stress-strain curve. This behaviour is used in applications like vibration damping, stents, etc. Magnetorheological fluid (MRF) is one of the smart materials which exists in liquid form. This MRF could change its viscosity under a varying magnetic field. Magnetorheological elastomers (MRE) are polymers which change their stiffness under varying magnetic fields. In active vibration control applications, the dynamic properties of the suspension system made of MRF and MRE, are modified desirably by external magnetic field to achieve the controlled dynamic behaviour. Such materials which can significantly change their physical properties are called smart materials. Potential applications of such materials attracted the research community to do engineering studies of these materials. One of these materials which falls into this category for its strong interaction between electrical and mechanical fields is called piezoelectric material.

1.2 Piezoelectric materials

Piezoelectricity is derived from the Greek language – 'piezo' means press and electric means amber, a source of electric charge. Piezoelectric material responds electrically for a mechanical stimuli, which is called direct piezoelectric effect, and mechanically for an electrical stimuli, which is called converse piezoelectric effect. These special behaviour

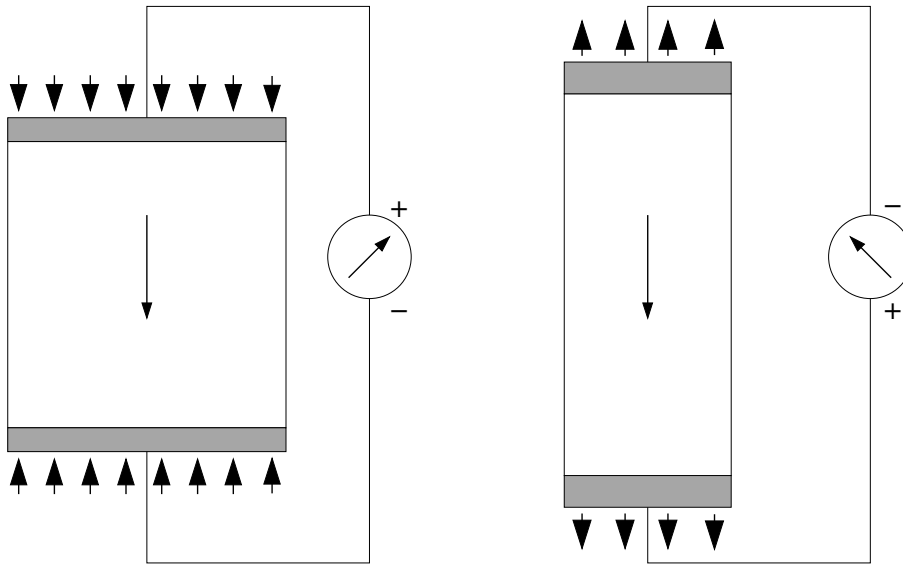


Figure 1.1: Direct piezoelectric effect.

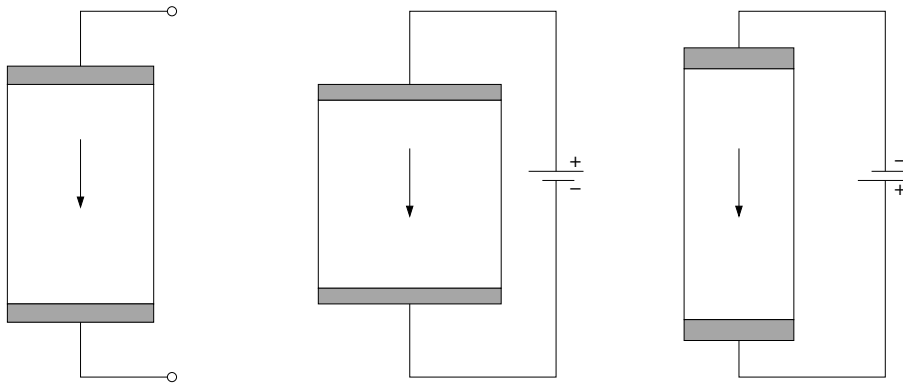


Figure 1.2: Converse piezoelectric effect.

are schematically shown in Fig 1.1 and 1.2. For the direct piezoelectric effect, material exerts surface charges when it is subjected to external stresses. The direction of flow of surface charges depends on the poling direction of the material and on the sense of the external stresses. For the converse piezoelectric effect, the material exerts a mechanical strain by applying an electric field. The strain will be compressive or tensile which again depends on the poling direction⁴.

This electromechanical coupling is linear within a certain loading range. This strong coupling behaviour can be identified by using a piezoelectric coupling factor. This piezoelectric coupling factor (k) is defined as the square root of the ratio of electrical energy converted to mechanical energy per given electrical energy or as the square root

⁴The piezoelectric material is electrically poled in nature. The direction from negative to positive charge is known as poling direction.

of the ratio of mechanical energy converted to electrical energy per given mechanical energy. The value of k is 0.7 or more [53] for piezoelectric materials. Another notable factor of this material is its response time. The response time of the material is observed to be very small which is advantageous for control applications. Degradation of material property under electric fatigue is little, making it reliable during its life cycle.

Due to its strong electromechanical coupling behaviour, less response time and high reliability, it could be used for various applications such as sensors and actuators. For example, in load cells, displacement sensors, etc., a voltage exerts in these devices which is proportional to measuring mechanical load or displacement as an output signal for calibration and measurement. In actuator applications, the given input signal in terms of voltage can be used for actuation output. It could also be used for some closed loop feedback control applications such as active vibration control, structural health monitoring, etc. As an example, the amount of fuel injection can be controlled to improve fuel efficiency and also to reduce emission by using fuel injectors with stacked piezoelectric actuators. This control system senses the NO_x, carbon monoxide etc. from the emission and gives the actuation signal accordingly.

1.3 Linear piezoelectric behaviour

In order to understand the mechanism behind this behaviour, let us consider a unit cell of one of these materials, e.g. BaTiO₃ or PZT, see Fig. 1.3. Even in the absence of an electric field, there is a separation between positive and negative charges. Due to this separation, an electrical dipole is present in the material. When the electric field is applied, due to Coulomb forces, the displacement between charges vary and the variation depends on the applied electric field. Thus, the applied electric field varies the electric dipole moment and therefore, the electric displacement. The change in electric displacement due to the applied electric field is given as

$$D = P + \epsilon_0 E = \epsilon_0 [1 + \chi_e] E = \epsilon E \quad (1.1)$$

where P is the polarisation, ϵ_0 is the electric permittivity of free space, χ_e is the electric susceptibility¹ and ϵ is the dielectric constant. Due to the change in displacement between charges under the electric field, there exerts a mechanical strain on a macroscopic scale. The relation between the exerted strain and the applied electric field is given as follows

$$\varepsilon = d E \quad (1.2)$$

where ε represents the strain and d represents the piezoelectric coupling coefficient. Similarly under external stress, the material undergoes a change in mechanical displac-

¹For piezoelectric material, the electrical susceptibility is in the order of 10^3 , which leads to the approximation $D \approx P$.

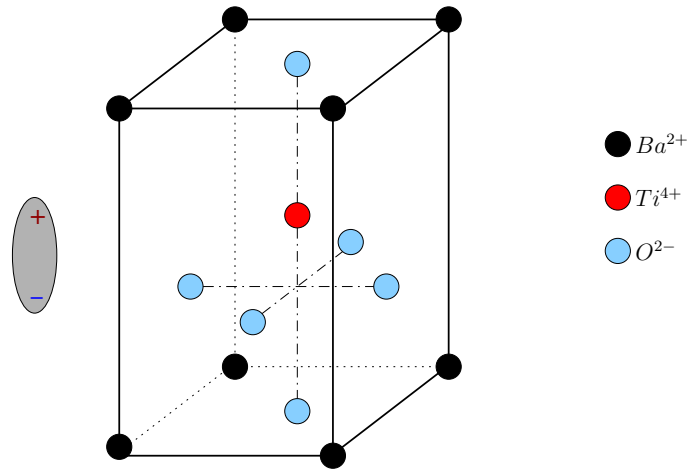


Figure 1.3: Tetragonal piezoelectric unit-cell as an electric dipole, [59].

ment. As a result, there exerts a change in displacement between charges. Thus the applied stress gives an electric displacement along with the strain. This behaviour under external stress can be represented as,

$$\varepsilon = \mathbf{C} \sigma \quad (1.3)$$

$$D = d^* \sigma \quad (1.4)$$

where σ is the stress, d^* is the piezoelectric coefficient² and \mathbf{C} is the compliance.

1.4 Linear three-dimensional constitutive relations

The constitutive relation of piezoelectric material is anisotropic in nature. There exists a four fold symmetry along the poled direction. Due to this, the material properties in two orthogonal directions lateral to poled directions coincide. By considering \mathbf{e}_3 as a poled direction, the constitutive relation can be represented using a matrix form with Voigt notation as in eq.(1.5). Due to the four fold symmetry, the properties in the direction along \mathbf{e}_1 and \mathbf{e}_1 are the same. In the polycrystalline material, there is a rotational symmetry along a poled direction in macroscopic scale. Therefore, it is

²The piezoelectric coupling coefficients d in eq.(1.2) and d^* in eq.(1.4) are numerically identical. This comes from the principle that within the reversible electromechanical regime, there exists an energy potential Ψ . This energy potential is independent of the loading path. So that

$$d^* = \frac{\partial^2 \Psi}{\partial \sigma \partial E} = \frac{\partial^2 \Psi}{\partial E \partial \sigma} = d .$$

commonly considered as transversely isotropic with the plane of isotropy being normal to the poled direction,

$$\begin{bmatrix} \varepsilon_1 \\ \varepsilon_2 \\ \varepsilon_3 \\ \varepsilon_4 \\ \varepsilon_5 \\ \varepsilon_6 \\ D_1 \\ D_2 \\ D_3 \end{bmatrix} = \begin{bmatrix} C_{11} & C_{12} & C_{13} & 0 & 0 & 0 & 0 & 0 & d_{31} \\ C_{12} & C_{11} & C_{13} & 0 & 0 & 0 & 0 & 0 & d_{31} \\ C_{13} & C_{13} & C_{33} & 0 & 0 & 0 & 0 & 0 & d_{33} \\ 0 & 0 & 0 & C_{44} & 0 & 0 & 0 & d_{15} & 0 \\ 0 & 0 & 0 & 0 & C_{44} & 0 & d_{15} & 0 & 0 \\ 0 & 0 & 0 & 0 & 0 & C_{66} & 0 & 0 & 0 \\ 0 & 0 & 0 & 0 & d_{15} & 0 & \epsilon_{11} & 0 & 0 \\ 0 & 0 & 0 & d_{15} & 0 & 0 & 0 & \epsilon_{11} & 0 \\ d_{31} & d_{31} & d_{33} & 0 & 0 & 0 & 0 & 0 & \epsilon_{33} \end{bmatrix} \begin{bmatrix} \sigma_1 \\ \sigma_2 \\ \sigma_3 \\ \sigma_4 \\ \sigma_5 \\ \sigma_6 \\ E_1 \\ E_2 \\ E_3 \end{bmatrix}. \quad (1.5)$$

However, this consideration is not valid in a single crystal piezoelectric material.

1.5 Non-linear ferroelectric behaviour

The linear piezoelectric behaviour is limited to a certain range of an applied electric field or mechanical loading. Beyond this limit, it behaves non-linearly and this non-linear behaviour is referred to as ferroelectric behaviour. This non-linear behaviour arises from the polycrystal nature of piezoelectric material. In a polycrystal piezoelectric material, the polarised crystals are oriented in different directions. In case of randomly oriented polarisation directions at the level of the single crystals, the macroscopic polarisation obtained by averaging the polarisation contribution over the entire region of the polycrystalline material results in negligible effective polarisation. In order to obtain the polarisation effect in the material for a specified direction, the crystals need to be oriented towards that direction. The process to orient the crystals to the favorable direction is called *poling*.

In a piezoelectric material with a tetragonal crystal structure, a unit cell can have six possible variants as shown in Fig. 1.4. A region of crystals contains single variant is called *domain*. Fig. 1.5 shows a piezoelectric polycrystal structure and the schematic sketch of the same. In this picture, arrows represent the direction of polarisation or dipole direction. Domains which distinguish the region from its adjacent region by its direction of polarisation are shown in thin lines, where the grain boundaries are shown in thick lines.

By applying an external electric field, the crystals in the domain will switch from one variant to another, see Fig. 1.6. This phenomenon of reorientation is called *domain switching*. As each of the variants have different polarisation direction and different dimensions in a particular axis, the change in domain from one variant to another gives macroscopically a change in polarisation and strain. This switching phenomena is irreversible and thus the material behaves non-linear during this process. This non-

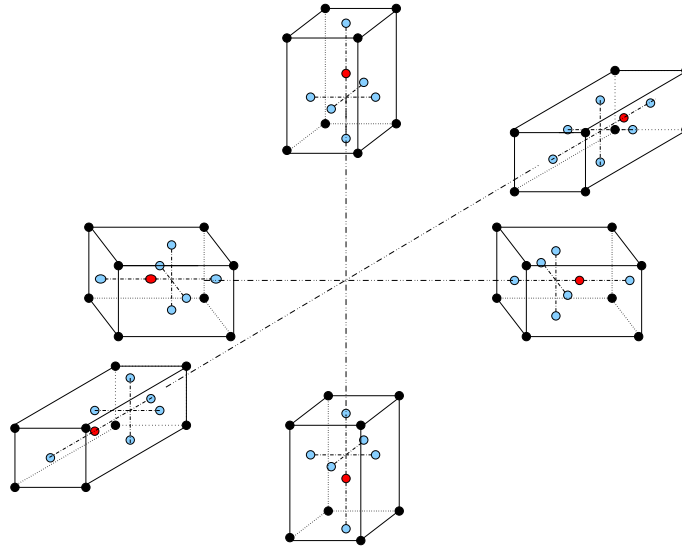


Figure 1.4: Six variants of a tetragonal crystal structure.

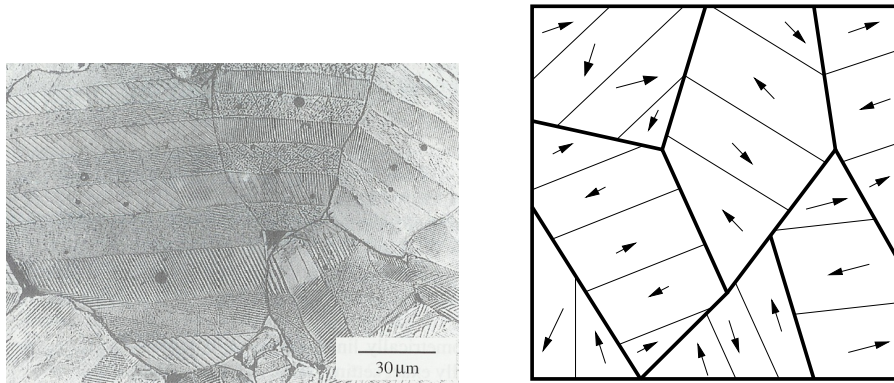


Figure 1.5: A polycrystalline grain structure [3] and a schematic picture of a polycrystal grain structure.

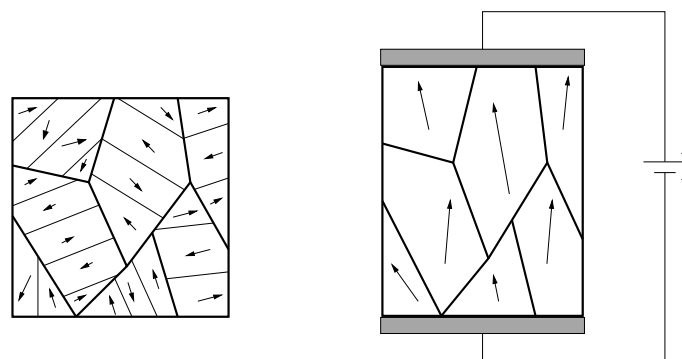


Figure 1.6: Schematic picture of the orientation of domains under an applied electrical field.

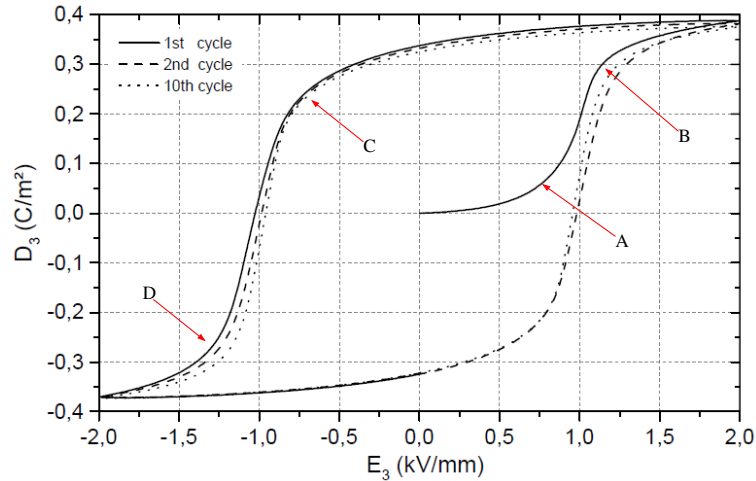


Figure 1.7: Experimental results of dielectric hysteresis behaviour [124].

linear behaviour is referred to as *ferroelectricity*⁴. During the domain switching process, permanent strains will be generated. This nonlinearity can be seen by observing the change in strains or electric displacement with respect to external stresses or electric fields.

1.5.1 Dielectric hysteresis

At the unpoled stress free state, the material's configuration can be identified with the origin in the graph as shown in Fig. 1.7. Upon applying an electric field, there will be a change in electric displacement. This change in electric displacement is due to the displacement of electric charges and is linear and reversible until it reaches point A. By further increasing the electric field beyond this point, the material obtains remnant polarisation due to domain switching. The direction of the polarisation is along the applied electric field. The electric field at this point is called coercive electric field E_c . The remnant polarisation then increases until it saturates at point B. There it reaches the maximum remnant polarisation. By reversing the electric field from point B, the electric displacement decreases linearly until it reaches point C. From point C, upon decreasing the electric field, the polarisation domains reverse their direction. Thus the remnant polarisation decreases. This switching occurs until the remnant polarisation is saturated in the negative direction. The point at this state is referred to as D. Further reversal of the electric field in the positive direction changes the remnant polarisation and it thus reaches point A and completes the hysteresis loop.

⁴The term ferroelectricity derives from the term ferromagnetism due to the analogy between their behaviour.

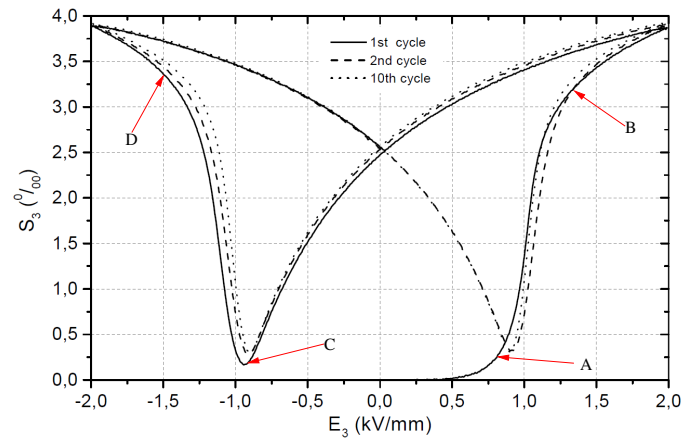


Figure 1.8: Experimental results of butterfly hysteresis behaviour [124].

1.5.2 Butterfly hysteresis

The ferroelectric hysteresis behaviour could also be observed in the electric field vs strain curve, which is known as butterfly hysteresis, Fig. 1.8. When the electric field is applied on the unpoled state of material, which is referred to the origin in the graph, no change in strain will be observed until the electric field reaches a coercive electric field at point A. Then the material starts domain switching and thus there will be a change in strain. This exerted strain is the additive decomposition of reversible part and irreversible part. The irreversible strain is referred to as remnant strain. The remnant strain evolves until the material reaches the saturation state of domain switching which is referred to as point B. Once the material reaches this saturation state, it will show a linear change in strain with respect to the applied electric field. However, reversing the electric field to a certain magnitude switches the domain in the reverse direction. As a result, the remnant strain is reduced until it reaches a point given as point C. At this point, the remnant strain becomes zero and after this point, the strain starts to increase. The point where the domains start switching in the reverse direction is given as point C. During this domain switching, the material exerts a positive strain. Switching becomes saturated at point D and behaves linearly for the applied electric field. The sign of change in strain with respect to electric field is opposite between the states from B to C and from A to D. This is due to the fact that the direction of polarisation is opposite between the states from B to C and from A to D.

1.5.3 Mechanical depolarisation

When external compressive stresses are applied upon the polarised material along the poling direction, the material undergoes depolarisation. This is called mechanical depolarisation. Fig. 1.9 represents experimental result of this behaviour. In a polarised material, ideally all the domains are oriented in the poling direction. This state is rep-

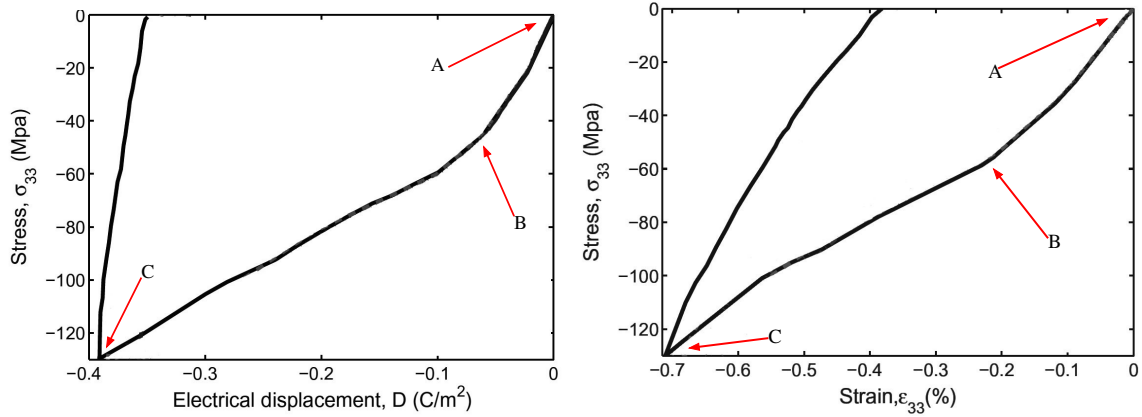


Figure 1.9: Experimental results of ferroelastic behaviour [57].

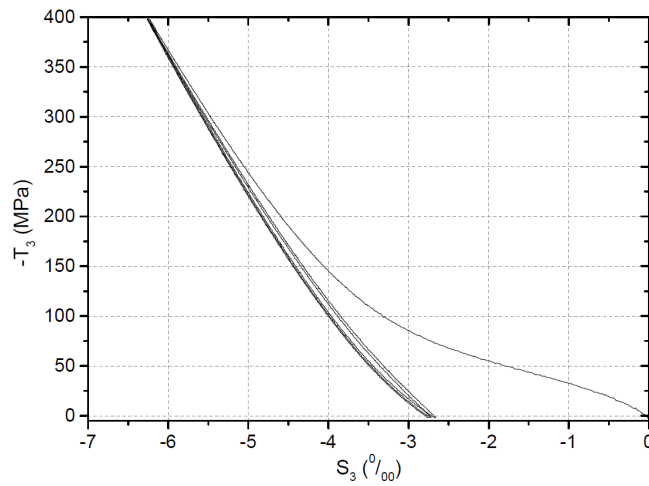


Figure 1.10: Experimental results of ferroelastic behaviour [124].

resented as A. Upon applying compression stress, the material behaves linearly until it reaches point B. Compressing the material beyond this point starts a domain switching towards the perpendicular plane to the poling direction. The domain switching from poling direction to its perpendicular plane is called 90° domain switching and the domain switching to the opposite direction is called 180° domain switching. This switching reduces the remnant polarisation and also the remnant strain of the material which has been exerted during the poling process. This non-linear switching continues until it reaches point C. At point C the domains which were oriented towards the loading direction switch to the other orthogonal direction, and thus the remnant polarisation will be zero at this point. By reducing the load from point C, one can observe a linear behaviour in the stress-strain curve.

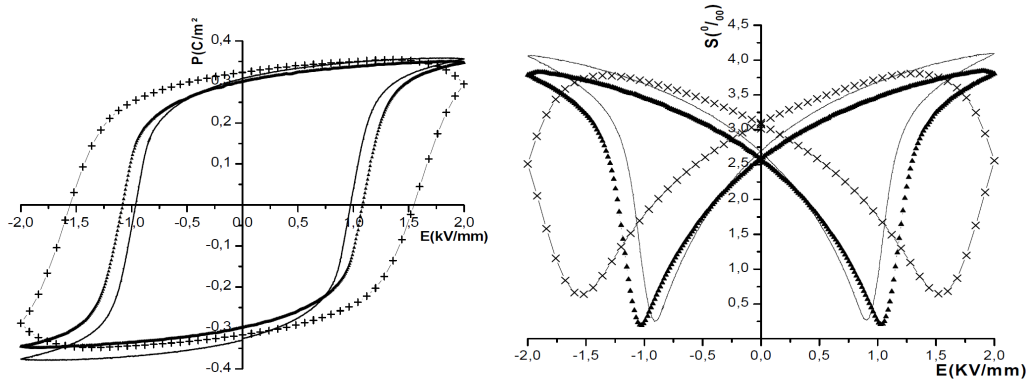


Figure 1.11: Rate dependent ferroelectric behaviour [125].

Mechanical loading on ferroelectric material causes non-linear hysteresis stress strain behaviour even without any changes in the polarisation. This behaviour is called ferroelasticity. Fig. 1.10 shows experimental result of compressive stress vs strain of the unpoled ferroelastic material. Upon applying the compressive stress, the domain along the direction of the applied stress will have a 90° domain switching. This switching results in an irreversible strain. This switching until all the domains along the loading direction are switched to the perpendicular plane. Upon further loading, the material shows elastic behaviour without any irreversible deformation.

1.5.4 Rate dependent behaviour

The rate of loading is found to have a profound effect on the ferroelectric behaviour. As the frequency of electrical loading increases, the coercive electric field of the hysteresis loop also increases. Furthermore, the saturation behaviour in ferroelectric hysteresis vanishes as the frequency increases. This rate effect could also be observed in the butterfly hysteresis loop. In a butterfly hysteresis loop, the change in total strain in a cyclic loading decreases. A schematic depiction of this behaviour can be seen in Fig. 1.11. This behaviour is due to the fact that, at higher rate of loading, the time taken for the domain switching process becomes comparable with the time taken for one complete cycle of loading. As a result, at higher frequencies, even before the completion of domain switching process, the external loading reverses the applied direction and consequently attenuates the completion of domain switching. Due to this fact, as the frequency of loading increases, the process of domain switching reduces. A notable reduction of polarisation and strain is therefore observed as the frequency of loading increases.

1.5.5 Thermal effects

As the ambient temperature of the material rises, a notable change can be observed in the ferroelectric behaviour. From Fig. 1.12, it can be observed that the increase in

temperature decreases the coercive electric field as well as the saturation polarisation. As the material's temperature rises to a certain temperature, the tetragonal crystal structure of the ferroelectric ceramics change their crystal structure into a cubic phase. This phase change temperature is called Curie temperature. The phase change effect can be observed in the experimental results of differential scanning calorimetry, Fig. 1.13 (d). Close to this temperature, the ferroelectric hysteresis behaviour is observed to have a double hysteresis loop, Fig. 1.13 (c). This effect is called antiferroelectric hysteresis. Upon further increasing the temperature above Curie temperature, the behaviour is observed to have no hysteresis effect.

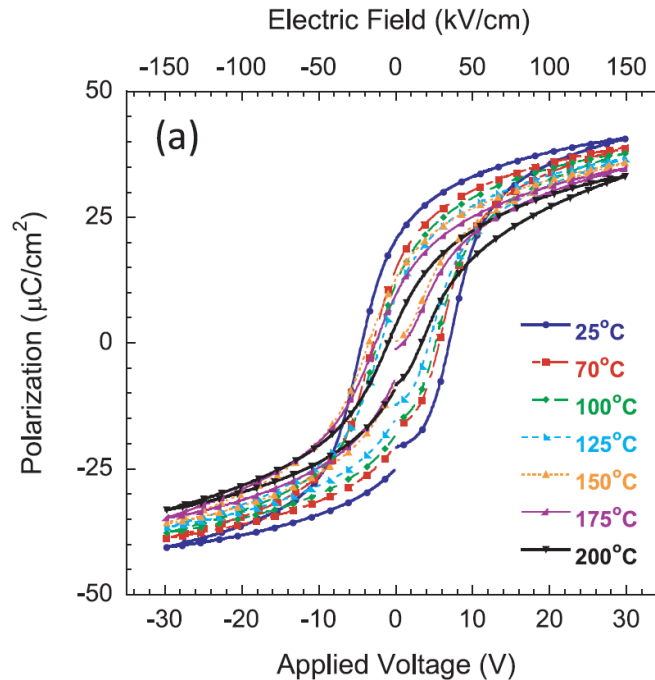


Figure 1.12: Temperature dependent ferroelectric behaviour [78].

1.6 Ferroelectric composites

Ferroelectric materials have a potential for many electro-mechanical applications such as sensors and actuators. However, they have some limitations due to their brittle nature. Because of that, these materials have some short comings like premature failure, difficulties to attach in curved structures, etc. To overcome these difficulties, piezoelectric composites are designed. Composites possibly give the advantageous characteristics of individual components. In piezoelectric composites, structural properties such as stiffness, deflection, fatigue life are improved and extend their application regime. These composites are classified, generally, based on the type of constituent material, spatial

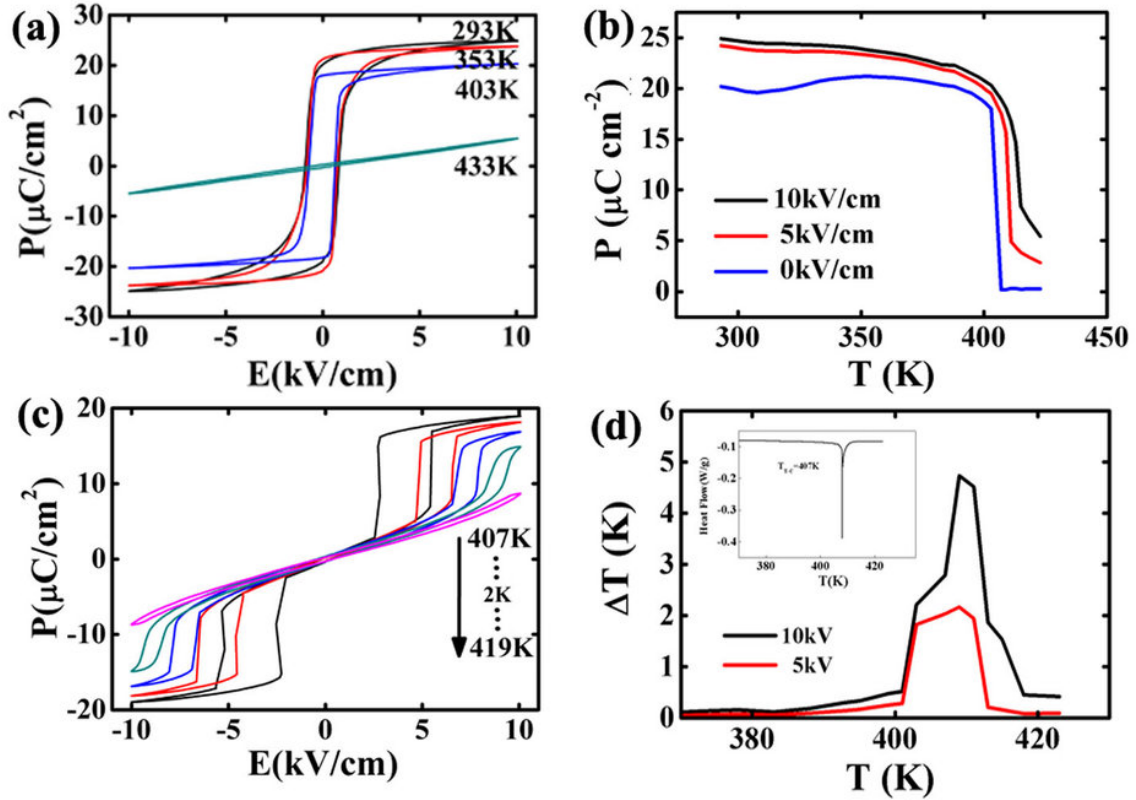


Figure 1.13: Temperature dependent ferroelectric behaviour [8].

arrangement of material phases and also based on the type of electrode used for the actuation [17]. Based on the required properties, epoxy or other polymers are generally used as the matrix material. According to the spatial arrangement of the piezoelectric material, the composites are classified as particulate, fibrous and laminar. Composites are also classified as n-m composites [89], where n and m are integers that represent the number of material flow of piezoelectric and matrix material respectively. For example, 1-3 composites, 2-2 composites, etc. In fiber composites, one can have different cross-sections such as rectangular fibers, round fibers and hollow fibers based on the advantages of different manufacturing techniques [66, 118]. Electrodes in the composites are classified as areal electrodes and interdigitated electrodes. Interdigitated electrodes have been introduced by Hagood et al. [44] to increase the electromechanical coupling by applying the electric field along the fiber direction. Active fiber composites and macrofiber composites are examples of interdigitated electrodes.

1.6.1 1-3 composites

Among various classifications of piezocomposites, 1-3 composites are one of the popular types of composites. Fig. 1.14 shows the schematic representation of 1-3 composites.

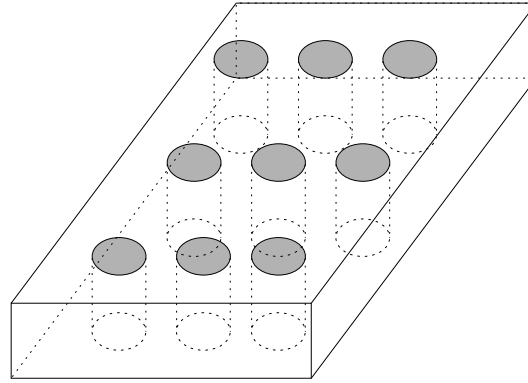


Figure 1.14: 1-3 composite.

In this composite, the piezoelectric fibers are embedded in a polymer matrix material. The fibers are poled along the axial direction of the fiber and electrodes are attached to the surface of the fibers. Due to the ease of poling and various advantages over monolithic material, the composite has been studied to a larger extent than other two phase piezoelectric composites.

The *dice and fill* fabrication technique is used for manufacturing 1-3 composites. By applying this technique, a solid piezoceramic disk will be grooved. This piezoceramic material will be poled before grooving. The grooved space will be filled with epoxy resin or any matrix material. Thereafter, the filled resin will be cured by bringing it to room temperature. Finally, the remaining ceramic base will be ground to form a required composite shape. Electrodes are then attached to the surface for the actuation. The *arrange and fill* technique is another technique used to manufacture the composite. By applying this technique, the fibers are arranged inside a mold and filled with epoxy resin and let to solidify. Here, the electroding and poling will be carried out once the composite is cut for the required dimensions.

1-3 composites have advantages such as low density, high sensitivity, high electrical capacitance, strong piezoelectric response in both transmit and receive operations, wide energy transformation band width, better damage resistance to mechanical shock and vibration, tailored acoustic impedance, etc. [75, 95] This composite is used for various applications such as piezoelectric tactile sensors, vibration energy harvesters, acoustic transducers, inertial sensors, pulse-echo ultrasonic transducer arrays, hydrophones, etc. [73, 104, 115].

1.7 Motivation for this work

Piezoelectric materials and their composites are useful as sensors. These materials could be used for large strain actuation applications. Due to their reliability and micro-second response, the material is also very useful in control applications. Because of the impor-

tance of ferroelectric materials and their composites in engineering applications, a well structured mathematical model needs to be developed. The development of such a model will be useful for application engineers who engineer this material for their applications in efficient and effective manner. Requirements of some applications can be such that the materials will undergo multiaxial loading. The response of the material in poling direction is different from the response of the material in the direction perpendicular to the poling direction. For such multiaxial loading applications, the uniaxial constitutive model is not sufficient, and therefore a three dimensional constitutive model needs to be developed which should also incorporate the anisotropic behaviour. Switching behaviour is a main phenomena in ferroelectric materials. Therefore, the nonlinear response of the material needs to be integrated in the model. From considering the importance of the material behaviour and the requirements of the constitutive model, developing a three-dimensional nonlinear ferroelectric constitutive model for ferroelectric material is a significant contribution in this field of research. Due to the advantages of ferroelectric composites over bulk material, it is also essential to develop a model to capture the behaviour of ferrocomposites. With these motivation factors, in this work, different three-dimensional nonlinear ferroelectric constitutive models are proposed to capture the influence of electrical loading rate, electrical loading amplitude, electromechanical loading and thermal loading. Also, homogenisation techniques are discussed for ferroelectric behaviour of composites to predict their effective properties.

1.8 Notation

The notations used in this work are briefly summarised for the reader's convenience. Cartesian basis vectors in a three-dimensional Euclidean space are denoted by $\{\mathbf{e}_i\}$ with $i = 1, 2, 3$. Tensors of first, second, third and fourth order are expressed in terms of their coefficients $[\bullet]_i$ and use of Einstein's summation convention is made, i.e. vectors are represented as $\mathbf{u} = u_i \mathbf{e}_i$, second order tensors read $\mathbf{S} = S_{ij} \mathbf{e}_i \otimes \mathbf{e}_j$, third order tensors take the form $\mathbf{e} = e_{ijk} \mathbf{e}_i \otimes \mathbf{e}_j \otimes \mathbf{e}_k$, and fourth order tensors are denoted as $\mathbf{T} = T_{ijkl} \mathbf{e}_i \otimes \mathbf{e}_j \otimes \mathbf{e}_k \otimes \mathbf{e}_l$, respectively. Inner tensor products between tensors of different order are denoted as the scalar products $\mathbf{u} \cdot \mathbf{v} = u_i v_i$ and $\mathbf{S} : \mathbf{T} = S_{ij} T_{ij}$, as well as $\mathbf{S} \cdot \mathbf{u} = S_{ij} u_j \mathbf{e}_i$ and $\mathbf{e} : \mathbf{T} = e_{ijk} T_{jk} \mathbf{e}_i$, together with $\mathbf{e} \cdot \mathbf{u} = e_{ijk} u_k \mathbf{e}_i \otimes \mathbf{e}_j$ and $\mathbf{T} : \mathbf{S} = T_{ijkl} S_{kl} \mathbf{e}_i \otimes \mathbf{e}_j$. Outer tensor products, also known as dyadic products, are represented as $\mathbf{u} \otimes \mathbf{v} = u_i v_j \mathbf{e}_i \otimes \mathbf{e}_j$ and $\mathbf{S} \otimes \mathbf{u} = S_{ij} u_k \mathbf{e}_i \otimes \mathbf{e}_j \otimes \mathbf{e}_k$ as well as $\mathbf{S} \otimes \mathbf{T} = S_{ij} T_{kl} \mathbf{e}_i \otimes \mathbf{e}_j \otimes \mathbf{e}_k \otimes \mathbf{e}_l$. Moreover, use of non-standard outer products is made, namely $\mathbf{S} \overline{\otimes} \mathbf{T} = S_{ik} T_{jl} \mathbf{e}_i \otimes \mathbf{e}_j \otimes \mathbf{e}_k \otimes \mathbf{e}_l$ and $\mathbf{S} \underline{\otimes} \mathbf{T} = S_{il} T_{jk} \mathbf{e}_i \otimes \mathbf{e}_j \otimes \mathbf{e}_k \otimes \mathbf{e}_l$ as well as $[\mathbf{S} \overline{\otimes} \mathbf{v}] = S_{ik} v_j \mathbf{e}_i \otimes \mathbf{e}_j \otimes \mathbf{e}_k$. The second-order identity tensor \mathbf{I} and the fourth-order symmetric tensor \mathbf{I}^{sym} are defined as $\mathbf{I} = \delta_{ij} \mathbf{e}_i \otimes \mathbf{e}_j$ and $\mathbf{I}^{\text{sym}} = \frac{1}{2} [\mathbf{I} \overline{\otimes} \mathbf{I} + \mathbf{I} \underline{\otimes} \mathbf{I}]$ with the Kronecker delta symbol $\delta_{ij} = \mathbf{e}_i \cdot \mathbf{e}_j$. The fourth order deviatoric projection tensor is given as $\mathbf{P} = \mathbf{I}^{\text{sym}} - \frac{1}{3} \mathbf{I} \otimes \mathbf{I}$.

2 Literature review

Piezoelectric material has been extensively studied by the researchers with respect to its potential on active control applications. This chapter provides an overview on the literature on various experimental studies conducted on bulk as well as on composites of piezoelectric materials to understand their different kind of behaviour and properties under various loading conditions. Thereafter, different ferroelectric material models, proposed to simulate their behaviour, and several homogenization methods suggested to obtain the effective properties of piezocomposites are reviewed.

2.1 Experimental studies

Various experimental setups and methods were used to predict the piezoelectric and ferroelectric behaviour of the material [1, 36, 110, 124]. Linear range material parameters are obtained with the resonator method by exciting the material to resonance and anti-resonance frequencies. Non-linear behaviour patterns in general are studied using uniaxial cyclic electric fields. Triangular cyclic electric fields are commonly applied for this study. The range of the applied electric field reaches upto $\pm 2.5\text{KV/mm}$. That requires high voltage even for this specimen. In order to avoid arcing due to such high voltage, the experimental setup is immersed in a silicon oil bath. The shape of ferroelectric material is chosen for the requirement of the experiment. The material is then cut from bulk ceramics and electroded on two opposite faces to apply electrical loading. The Sawyer tower circuit is used to measure the electrical displacement. Displacement sensors such as strain gauge, LVDT or laser vibrometer are chosen based on the required accuracy and suitability to the experimental setup. Huber et al. [48] studied the polarisation rotation behaviour. In this study, a block of specimen is cut from a plate of poled ferroelectric material with the faces of the blocks cut at differing angles to the poling direction. The authors used this experiment to study the change in polarisation with the electric field for various angles from the poling direction.

Experiments under mechanical loading are quite challenging due to the brittle nature of the material. The report of Hwang et al. [51] describes the experimental setup for electromechanical loading to study its nonlinear ferroelectric behaviour under constant stress. A servo-hydraulic device is set up to apply a constant mechanical load and a load cell is used to determine the external stresses. Some studies are motivated based on temperature dependence of the material behaviour. In [56], the authors used a ring

heater with a PID controller to study the behaviour at constant temperature. For such experimental setups, a thermocouple is one of the commonly used temperature sensor.

As an actuator with complicated shapes, piezoelectric material can undergo high compressible stresses. Behaviour patterns at high stresses are studied to understand the permanent deformation and performance degradation during such loading condition [67]. Studies on this aspect revealed the inelastic nature of this material in stress strain behaviour [68] which is referred as ferroelastic behaviour. Soft doped piezoelectric materials, which are characterized by high relative permittivity are observed to have this ferroelastic behaviour prominent than hard doped piezoelectric materials. Hence, it has been suggested that hard PZTs can be used for high stress levels without depoling or permanent strain. From the stress-strain curve of polycrystalline barium titanate, it was noticed that the material has lower strength during tension than during compression [112]. This observation gave the motivation to study the nonsymmetrical deformation of the PZT. It is observed that the value of plastic strain is double in tensile loading compared to compressive loading for the same stress value [37]. In another study, increasing compression load resulted in decreasing remnant polarisation [18]. Further studies under compression stress also showed a reduction in the dielectric hysteresis and butterfly hysteresis [126].

Recent studies have shown that the ferroelectric properties of piezoelectric material are highly influenced by the grain size of the material. In the work of Arlt et al. [4], for barium titanate ceramics, it was observed that the decrease in grain sizes less than $10\ \mu\text{m}$ decreases the width of ferroelectric 90° domains. Therefore, decreasing grain size increases the dielectric constant of the material. For the material with very fine sized grain ($> 0.7\ \mu\text{m}$), the dielectric constant starts reducing. From the experimental work of Zhou et al. [123], the decrease in grain size distorts the tetragonal lattice structure and as a result reduces the heat of phase transition as well as the Curie temperature. Liu et al. [76] conducted the experimental studies on ferroelectric films for a relationship between coercive electric field and grain size. According to their observation, the coercive value increases by decreasing the grain size until it reaches a critical grain size and then it starts decreasing rapidly. It has also been observed that the dependency of coercive value with the grain size increases as the film thickness decreases.

Studies on thermal effects of ferroelectric materials are important to improve the know for design of the material for applications like fuel injector or other high temperature actuation systems. The study [74] reported that there is an increase in dielectric constant with respect to temperature. Various non-linear behaviour patterns of piezoelectric material at high temperature are reported in the literature. At high temperatures the material has been observed to have low ferroelectric hysteresis effect [39]. It has also been observed to have low ferroelastic hysteresis [117]. These experimental results were the motivation to propose temperature dependent domain switching models [102]. Above the Curie temperature materials undergo a phase change which results in depolarisation. Such thermal depolarisation due to phase change is studied by Gonzalez-Abreu et al. [41]. In this work, the authors tested the phase change temperature for various lead

free ferroelectric ceramics and also presented the change in polarisation with respect to temperature. Ma et al. [78] studied the PLZT material for temperature effects on ferroelectric behaviour. From their observation, the value of coercive electric field decreases as the temperature increases. In the work of Bai et al. [8], the ferroelectric hysteresis is observed to have a double hysteresis antiferroelectric behaviour as the temperature gets close to the Curie temperature. The behaviour at high frequency of loading varies from low frequency loading. This loading rate dependency on ferroelectric properties is reported in [124]. According to their findings, ferroelectric domain switching is more prominent for lower frequencies of loading than for higher frequency.

In addition to bulk PZT studies, considerable experimental research has been performed on piezocomposites. Experimental setups used for ferroelectric materials are used for measuring the behaviour of composites as well. Experimental studies on pillar shaped PZT composites showed that the material parameters not only depend strongly on the type and volume of matrix material but also on the spatial distribution of the PZT pillars [45]. From the experimental studies of Furukawa et al. [113] on piezocomposites with epoxy resin as a matrix, the dielectric constant is noticed to have strong temperature dependence for high volume fractions of the matrix. Dynamic properties of the material are important for high frequency applications like sound attenuation. Grewe et al. [42] showed that the acoustic properties of particle filled composites depend on the particle type, the particle size, the volume fraction of the filler, the polymer matrix type, and the adhesion properties between matrix and the filler. An attempt to study the influence of fine (10-50 μm) piezofibers showed a reduction in material constants. The reason behind such results were reported due to the damage of piezo fiber during the poling process [109]. Non-linear behaviour of 1-3 composites has been studied by Jayendiran et al. [55]. In their study, a reduction in the ferroelectric hysteresis nature of the composite by increasing the volume fraction of the fiber is observed. Piezocomposites also have a similar reducing effect of ferroelectric hysteresis as the temperature increases [56].

2.2 Ferroelectric constitutive models

To design an actuation system for certain applications, a mathematical model for the constitutive behaviour of the material has to be established. There are various references in the literature that deal with the constitutive modelling of ferroelectric materials to predict the non-linear behaviour of these materials. Various methods are used throughout the literature based on the scale of the material under consideration. In atomic scale models, atoms of a unit cell and the interaction between them are considered for the system of analysis. The works [24, 38, 116] used ab initio calculations via quantum mechanical principles for solving the fundamental interactive forces between atoms in the crystal structure. To imply the quantum mechanical principles, the Schrodinger equation is solved for such system. However, it is highly demanding to solve this problem even for a small system. The Density Functional Theory (DFT) is commonly used

to reformulate this problem in order to overcome its complexity. Even though this first principle study is not able to describe the ferroelectric behaviour, it could be used to study phase change properties, electromechanical properties, optical and magnetic properties of the material, which are helpful in developing relatively large scale models. Other than atomic scale models, ferroelectric models are commonly classified as micromechanical and phenomenological ones.

2.2.1 Micromechanical models

Micromechanical models consider the interaction between domains and grains. In micromechanical models, the constitutive behaviour of a single crystal is taken into account. The effective behaviour of a ceramic polycrystal is obtained by averaging a large number of crystals with different orientation. Hwang et al. [51] introduced this method to simulate the electromechanical behaviour of the switching process. In this study, a tetragonal crystal structure is considered and therefore the domain switches within six possible variants of the crystal structure. The driving force for this switching phenomena is obtained based on work energy criteria for a given electromechanical load. 10,000 grains are considered with random orientation, and the stress and electric field that are applied to all these grains are considered to be homogenised by using the Reuss approximation. The calculated spontaneous strains and polarisation of each grain with respect to their individual coordinates are then transformed to a global coordinate system. The resulting strains and polarisation in the global coordinates are then averaged to model the macroscopic ferroelectric effect. The simulation results gave insight of the ferroelectric hysteresis, butterfly hysteresis and mechanical depolarisation. [83] considered grain orientation parameterized as a function of Euler angles. The quantity of internal variable such as remnant polarisation and strain in orientation space render a related macroscopic contributions. Equation for switching criteria in this work is considered so as to comply with transversely isotropic symmetry of material properties.

Models discussed previously did not consider interaction between the grains. This interaction gives an additional contribution to work energy potential in the switching criteria and this additional contribution is denoted as interaction energy. This interaction energy in the system considered in [81] is calculated using the mean field theory. [23, 52] used this interaction energy in the switching criteria for their model. In addition thereto, [23] extended the previous micromechanical work by considering the crystal structure change between rhombohedral and tetragonal systems. A study on accounting the switching phenomena between these two crystal structure in PZN is shown in [92]. Six variants of tetragonal structure and eight rhombohedral variants were considered for domain switching. Furthermore, the authors considered a saturation in linear piezoelectric effects at large applied electric field. In [22], the authors extended this model to capture the antiferroelectric effect. Huber et al. [49] extended the micromechanical approach to consider the change in linear piezoelectric properties by using a self-consistent

scheme for the polycrystal. Later, the authors used a viscoplastic approach [48] instead of a perfectly plastic approach to improve the computational efficiency.

Instead of a random orientation of crystals, [50] considered volume fractions of six variants to calculate the remnant strain and remnant polarisation. Changes in volume fractions of each variant depend on the switching criteria. Elhadrouz et al. [34] developed a micromechanical model for ferroelectric single crystals. In this model, the interaction energy term is obtained from the kinematic adjustments with the adjacent domains. The simulation results show the change in strain and electric displacement of a poled material which is termed as mechanical depolarisation. Based on an effective medium approximation, Roedel and Kreher [96, 97] developed a model to describe a polycrystalline behaviour of ferroelectrics. In this model they considered only the domain wall motion and excluded the domain switching. With this consideration, the model could capture the minor hysteresis of the poled ferroelectric ceramics. To study the domain patterns and their evolution, Zhang et al. [121, 122] introduced a phase field modelling approach. In this work, the finite difference method is used to solve related boundary value problems. The authors studied the domain motion for various conditions such as cubic to tetragonal transformation and different electromechanical loading. Ferroelectric hysteresis curves have also been obtained by averaging the field variables over the domain. In the works [98, 111], the authors implemented the domain evolution in finite element analysis framework. Xu et al. [119] used this micromechanical analysis to predict the mesoscopic response.

Kim and Jiang [64] formulated a model to describe its rate dependent effect. In this formulation, the evolution of mass fractions, which are considered as internal variables, depends on the frequency of the applied loading. This model is implemented in the finite element method and obtained ferroelectric hysteresis and butterfly curves for different rates of loading. The results could predict the qualitative behaviour of the experimental observations. A micromechanically motivated model for rate-dependent response of piezoceramics using finite element formulation is discussed in Arockiarajan et al. [5, 6]. Using a finite element formulation, in [5], the piezoelectric problem is reduced to a purely electrical problem by considering only the electric degrees of freedom. Later on, this work was extended to electromechanical loading, [6]. In [7], the authors used an additional term in the energy based switching criteria to consider the impact of grain boundary effects. To consider the non-uniformity in the grain size, Jayabal et al. [54] used a polygonal finite element approach to predict the intergranular effects.

2.2.2 Phenomenological models

The consideration of switching for each crystal leads to a large number of variables. Thus, this approach is computationally inefficient for the simulation of large scale real world application systems. This requires a model with few variables, respectively degrees of freedom, for macroscopic systems. This motivates the development of phenomenological macroscopic models.

The works [29, 30] are one of the early studies on phenomenological modelling of non-linear ferroelectric behaviour. In this phenomenological treatment, a free energy potential is considered as a function of dielectric constant, crystal structure, internal energy and self polarisation which vary with respect to temperature. This model was able to calculate the dielectric constant and remnant strain for various temperatures and also for different crystal structures. However, this approach is limited to a stress free one-dimensional analysis. Chen et al. [19–21] proposed a constitutive relation and rate law of internal variables for electromechanical behaviour. In their approach, the electric dipoles, which represent the macroscopic electrical properties, can alter their magnitude and direction by external stimuli. They considered the dipole response to be transient and instantaneous to represent rate dependent behaviour. With this approach, they successfully captured the ferroelectric and butterfly curves. However, this model lacks the capturing of further electromechanical phenomena.

Many phenomenological models have been developed based on a thermodynamical framework which is analogous to the theory of plasticity. In this model, two sets of state variables are used to describe the state of the system. These are external variables, which describe the observables on the current state of the system and internal variables, which describe the nature of the system due to the history of loading. Internal variables are essential in such a model to describe the irreversible hysteresis behaviour of the material. Stating evolution functions and the conditions for evolution of these variables are the main theme in developing the constitutive relation. These evolutions are developed in such way that they fulfil the Clausius-Duhem inequality.

One thermodynamically sound phenomenological model is presented in Bassiouny et al. [10–13]. In these works, a free energy function per unit volume is introduced as a function of temperature, strains and the polarisation. The polarisation is additively decomposed into a reversible and an irreversible part, which serves as internal state variable. These internal variables are computed based on the maximum dissipation hypothesis. For rate-independent effects, an electric loading function, or rather switching criterion, is suggested to determine the evolution of the internal state variable. With this model, they could capture the ferroelectric hysteresis for different compressible stresses. In [11], the authors presented an analysis for a ferroelectric circular cylinder subjected to torsion and a longitudinal electric field.

Cock and McMeeking [25] developed a phenomenological model using the idea of Bassiouny's work. They developed a one-dimensional model which reflects the dielectric and the butterfly hysteresis. In this model, kinematic hardening concepts are used to capture the ferroelectric switching. Landis and McMeeking [71] developed a model to simulate the ferroelastic behaviour. They adapted the plasticity theory with a quadratic switching surface along with the associated flow rule. However, the scope of this model is only to capture the behaviour due to mechanical loading and therefore it does not deal with electrical loading.

Kamlah and Tsakmakis [59, 61] developed a one dimensional ferroelectric and ferroelastic domain switching model. This model could capture most of the nonlinear

electromechanical phenomena. Remnant polarisation and irreversible strains are used as the internal variables. They used a separate yield surface for ferroelectric and ferroelastic switching. In addition, two separate surfaces were introduced to condition the saturation limit. With the use of linear kinematic hardening, the model could capture a ferroelectric, ferroelastic and butterfly curve hysteresis in a reasonable manner. In this contribution the irreversible strain part is additively decomposed into two parts, where one evolves from ferroelastic switching and where the other part is due to ferroelectric switching. The ferroelectric switching part is obtained from a direct relationship to the remnant polarisation. The model also considers the saturation polarisation as a function of stress. By using this function, the mechanical depolarisation effect could also be captured. Due to the complexity involved in the evolution of the internal variables, they are computed using the Euler forward method, which requires a small time step of loading. Later, this model was extended to three dimensions with the idea of implementing it for the finite element analysis [60]. It has been observed to have convergence issues during the implementation which was overcome with a staggering approach. Despite its lack of numerical efficiency, the analysis of stacked actuator was successfully implemented.

Landis [72] developed a rigorous thermodynamical framework for a three-dimensional constitutive relation to capture ferroelectric, ferroelastic, butterfly hysteresis and mechanical depolarisation. In this approach, he used a single switching surface for all different switching phenomena. Remnant polarisation and irreversible strains were considered as internal variables. McMeeking and Landis [82] simplified this formulation by considering remnant polarisation as internal variable for the cost of limiting its capability on capturing ferroelastic behaviour. Schröder and Romanowski [100] used the idea of only one switching criterion for their work. They used the coordinate invariant thermodynamically consistent model which is based on the work of Schröder and Gross [99] and which accounts for the dielectric hysteresis as well as the butterfly hysteresis. In the uni-axial model the polarisation direction is assumed to be constant, which limits the model from capturing the polarisation rotation.

A rate-independent ferroelectric and ferroelastic model is suggested by Klinkel [65]. In this model, a key difference from other models is that it uses an irreversible electric field as an internal variable instead of irreversible polarisation. Irreversible strain is also used as the internal variable which is further additively decomposed into two parts, with one contribution being directly related by a one to one relation with the irreversible part of the electric field and the other part is due to the mechanical depolarisation term. This approach could capture ferroelectric, ferroelastic, butterfly hysteresis and mechanical depolarisation. It could also capture the different saturation limit of strain under compression and under tension in ferroelastic behaviour. The model is flexible enough in capturing the experimental results. A wide range of experimental data as well as simulation results are captured by this model. However, under cyclic electric loading with constant prestress, the simulation results produce a ratcheting behaviour in the butterfly curve which is an unphysical phenomenon and is not observed in the experiments. A rate-dependent formulation of ferroelectric behaviour, conceptually

analogous to viscoplasticity, is established in Miehe and Rossato [84]. In this model, the irreversible polarisation is modelled as an internal variable and captured and the model is formulated based on an incremental variational framework. This model reflects the rate dependent behaviour of the material which is observed in the experiments. With this model, a boundary value problem is solved by implementing it in a finite element analysis framework. Later this work is extended to electro-magneto-mechanical coupling problems [85]

Typical piezoelectric finite element models use displacements and the electric potential as nodal degrees of freedom, see Gaudenzi and Bathe [40]. Accordingly, the electric field and the strains are calculated from the gradients of the nodal degrees of freedom. By assuming the free charge density in the volume to be zero, the divergence of the electric displacement can equate to zero. Thus, the electric displacement can be derived from a vector potential. Considering this vector potential as the nodal degree of freedom instead of the usual scalar potential, Landis [70] presented a new formulation. This method improves the numerical stability for nonlinear ferroelectric constitutive equations. In Kamlah and Böhle [60] the finite element analysis is carried out in a two-step scheme to avoid a switching of variables. In the first step a purely dielectric boundary problem is solved to obtain the electric potential. In the second step, the electro-mechanical problem for the mechanical boundary conditions is solved with the prescribed electric potential from the first step. For the finite element solution, Newton's method was employed including the analysis of the domain switching process with incremental loading steps. Since the constitutive relations are highly nonlinear due to hysteresis effects, the Newton iteration scheme is used. This procedure is standard for solving problems with inelastic material behaviour, see e.g. Simo and Hughes [106]. Such procedures are also used in Klinkel [65] and Miehe and Rossato [84].

2.3 Models for piezocomposites

The aim of piezocomposite modelling is to predict the variation in the effective response of the composite with respect to the volume fraction and complex geometry of the constituents, thermal effects and also the electromechanical properties of matrix material. These models are important not only for the design of the actuator system applications but also for the design of the piezocomposite itself to tune the properties for requirement.

Newnham et al. [89] introduced an analytical model based on the connectivity for piezocomposites to predict its structure-property relations with respect to series and parallel connectivity. Using this relation, Banno [9] developed an analytical model to calculate the behaviour of 0-3 type and 1-3 type composites. Later, Aboudi [2] used this procedure to calculate the thermo-piezoelectric properties of the multiphase composites. Smith and Auld [108] developed a material model to predict the material properties which govern the thickness mode oscillation in thin 1-3 piezoelectric composites. Schulgasser [101] developed a method to obtain the effective behaviour of composites by considering only the volume fraction and excluding the geometry of the constituents.

In this approach, both the fiber and matrix are considered as a transversely isotropic material. In [107], the author used a parallel-series connectivity approach for 1-3 composites as in [89] to find out the properties for hydrostatic coefficients. This work aims to facilitate as a design tool for underwater application. Sigmund et al. [103] developed a topological optimisation method to enhance the performance of 1-3 composites for underwater hydrostatic applications.

In an analytical method developed by Benveniste [15], effective constants of the composite aggregate are calculated from the local field by considering uniform strain and electric field intensity throughout the material. Dunn and Taya [31] developed a piezoelectric analogy to Eshelby's tensor [35] in the elastic case. Later, the authors used this method to formulate a model for fiber composites with a cylindrical inclusion [32]. For non-dilute concentration, the authors extended a mechanical field formulation by Mori and Tanaka [86] and Benveniste [14] to the electromechanical field formulation. Haung and Kuo [47] developed an analytical technique to determine the effective properties of piezoelectric composites containing spatially oriented short fibers. Here, the effective material constants are expressed in terms of phase properties, volume fraction and shape inhomogeneity by treating the fibers as spheroidal inclusions. The results show that the longitudinal and in-plane shear moduli increase with fiber length, while the piezoelectric and dielectric constants decrease. In the work of [69], the authors expressed the effective constants by investigating composites as a three-dimensional anisotropic inclusion of piezoelectric material in a matrix. With the results, they came to the conclusion that the electromechanical coupling is strongly affected by both the volume fraction and the orientation of the inclusion. Poizat and Sester [94] also mentioned the piezoelectric effects as a function of volume fractions along with the aspect ratio of the inclusion.

Kar-Gupta and Venkatesh [62] developed a homogenisation method for capturing the electromechanical response for 1-3 piezoelectric composites. In this work, both the matrix and fiber are considered to be transversely isotropic and piezoelectrically active. Bonnet [16] showed this method to solve for composites with elliptic cross sections and multi-phase fibrous composites. Dell and Shu [27] investigated a 1-3 composite with both an active and passive matrix using the micromechanics based Mori-Tanaka model. With the results, they concluded that the active polymer matrix can improve the hydrostatic performance more significantly than passive matrix material.

In the research work discussed above, the homogenisation methods to calculate the effective responses of the piezoelectric material omit the information on the geometry of the fiber. There are methods which adopt the actual geometry of the composite and calculate the effective properties using finite element analysis. Hossack and Hayward [46] made an attempt to discover the influence of ceramic volume fraction, pillar shape and orientation on the piezoelectric characteristics of 1-3 composites using finite element analysis. In this work, they used circular, triangular and square shape pillars for the analysis. They suggested that this numerical method could be used as a good design tool for composites. Silva et al. [105] used the finite element analysis to observe the effective properties of a composite with complex topology. In this analysis, they used

periodic boundary conditions for the unit cell. Pettermann and Suresh [93] studied composites for a different kind of periodic arrangement such as hexagonal and square arrangements of continuous fibers using finite element method.

Odegard [91] calculated the electromechanical properties of various piezoelectric composites such as Graphite/PVDF fiber composites, SiC/PVDF particle composites, PZT-7A/polyimide fiber composites, and PZT-7A/polyimide particle composites. The author used the finite element analysis for the calculation and compared the results with the Mori-Tanaka self-consistent method. The comparison was carried out for various volume fractions of piezoelectric material. This proposed method turned out to achieve results as accurate as the ones achieved by the Mori-Tanaka method. It also has the advantage of not requiring the iterative scheme as the Mori-Tanaka method. Muliana [88] estimated time dependent properties of fiber reinforced composites using a finite element based micromechanical model. In the work of Zhang and Wu [120], they studied the influence of connectivity and shape of the fiber in the two phase composites. In this work, 3-0, 3-1, 3-2, and 3-3 are the connectivities and circular cylinder, elliptical cylinder, and triangular prism are the shapes they have considered.

2.4 Motivation and scope based on the literature review

Due to the importance of piezoelectric materials in engineering applications, a significant amount of work has been carried out on its material characterisation and modelling. From the contribution of experimental work, extensive studies have been made on ferroelectric behaviour under the influence of various physical factors such as external stress, temperature, loading rate, grain size, etc. From the aspect of modelling, both micromechanical and phenomenological modelling are the two approaches which have been followed. In micromechanical modelling, with fewer assumptions, physically sound models have been proposed. The development of such models is useful for multiscale modeling methods. For the advantage of numerical efficiency in the calculation of large scale systems, phenomenological models have been developed. Within this classification, one dimensional models are limited to the analysis of the material which undergoes uniaxial loading. Three dimensional piezoelectric models have been introduced to analyse multiaxial loading conditions.

From the literature on phenomenological modelling on bulk ferroelectric materials, there is only a limited number of proposed models which considered the influence of stress and temperature on ferroelectric hysteresis behaviour. Therefore, as a part of this work, a model has been proposed which could capture the influence of dielectric and butterfly hysteresis under compressive stress. This model has also been developed so that it could capture the behaviour of mechanical depolarisation and ferroelasticity. In addition, an elliptical switching surface has been introduced in order to capture the anisotropic switching behaviour observed in experimental analyse.

The hysteresis behaviour of the material is highly influenced by the amplitude of the applied electric field. Depending on the magnitude, the material exhibits minor or

major ferroelectric hysteresis. Along with this behaviour, in a prepoled material, the material exhibits asymmetric butterfly hysteresis. To capture these behaviour patterns, a multiple switching surface model has been proposed in this work. To avoid complexity, the model focuses only on the ferroelectric hysteresis behaviour.

Experimental studies on temperature dependency on the piezoelectric material are carried out to a large extent. The effect of temperature on the properties of linear piezoelectric material parameters is implemented in various models. However, the models merely focus on the effects of hysteresis behaviour due to temperature, in particular the switch between the ferroelectric hysteresis to antiferroelectric hysteresis and also thermal depolarisation. Having the importance of temperature dependent ferroelectric hysteresis model and the fact that it has been merely discussed in the existing literature as a motivation factor, a temperature dependent model has been proposed. A different method has been introduced in the calculation of internal variables in order to improve the numerical efficiency.

From the literature on piezoelectric composites, material properties of the matrix material, the volume fraction of the constituents and the distribution of the constituents are known to have greater influence on the properties of ferroelectric composites. Various homogenisation approaches have been proposed to predict the effective properties of ferroelectric materials. However, they mainly focus on the linear piezoelectric behaviour. For applications like large deformation actuators, studies on ferroelectric hysteresis behaviour of ferroelectric composites are deemed to be important. Therefore, in this work, a homogenisation procedure to obtain the rate dependent behaviour on ferroelectric composites from a rate dependent ferroelectric model is proposed. A finite element homogenisation procedure is also introduced in this work.

2.5 Organisation of the work

The subsequent chapters of this thesis are organised as follows. In chapter 3, an overview of the aspects of electromechanical modelling is discussed. Here, based on the considered assumptions, the field equations are introduced. Subsequently, a discussion on constitutive modelling within a thermodynamical framework is given. Using the discussed framework, a rate dependent ferroelectric model is then presented. For numerical examples, the material parameters are calibrated based on experimental data for various frequencies of loading and with that parameters the simulations are performed. The simulation results obtained are then compared with the experimental data.

In chapter 4, the model introduced in chapter 3 is extended to a multi-surface model. Here, instead of having remnant polarisation as a single internal variable, it is additively decomposed into several contributions. Therefore, an independent switching surface for each internal variable is introduced. Using this formulation, the behaviour of minor hysteresis as well as asymmetric hysteresis could be captured. Graphical illustration is given in order to better understanding the ability of the model to capture the mentioned behaviours. The simulation results are referred to material parameters for parameter

calibration. In addition, the model is used to simulate the decaying behaviour of offset polarisation observed in the electrically fatigued specimen is also presented.

In chapter 5, along with ferroelectric hysteresis behaviour, a model is presented which could capture the behaviour of ferroelastic and mechanical depolarisation. The main difference from other models available in the literature is the incorporation of anisotropic behaviour of the switching surface in the poled specimen. This anisotropic behaviour becomes evident from the polarisation experiments. To reach a qualitative comparison and to show the capability of capturing various behaviour patterns, the simulation results are presented along with the experimental results from the literature.

In chapter 6, an alternative approach for solving the evolution equation of internal variables for ferroelectric models is provided. Using this method, a local iteration procedure in the finite element analysis can be totally omitted for nonlinear hardening models. Therefore, this method can be seen as a great improvement in the computational efficiency. Then the model is implemented in the finite element framework to solve boundary value problem. Thereafter, a temperature dependent model is introduced. This model is able to capture the thermal depolarisation behaviour as well as the antiferroelectric behaviour. Numerical examples are then presented for the ferroelectric behaviour under various temperatures.

Chapter 7 discusses the homogenisation procedures in the analysis of the effective properties calculation for ferrocomposites. A 1-3 fiber composite with various volume fractions is used for the analysis. In the first part of this chapter, various semi-analytical homogenisation procedures are discussed. Following that, a homogenisation procedure using a finite element analysis is presented. In these procedures, for ferroelectric material, the constitutive model introduced in chapter 3 is considered. For the matrix material, linear piezoelectric constitutive models with negligible coupling terms are considered. The results from both procedures are then compared with experimental data. At the end of this chapter, a comparison with both of these procedures along with experimental data is given. Finally, in chapter 8, the presented work is concluded with a perspective on future work.

3 A single surface model for ferroelectric ceramics

The present chapter deals with the constitutive modelling aspects of ferroelectric materials. The chapter begins with the introduction on the fundamental governing equations in electromechanical continua. Following that, the thermodynamical framework on constitutive modelling is discussed. In this section, a stress driven model and a strain driven model are discussed. Thereafter, a three dimensional rate dependent ferroelectric constitutive model is introduced. In the results section, the introduced model is used for numerical simulations for various loading frequencies as well as for a so called polarisation rotation test. For this numerical simulation, the material parameters are calculated by using a parameter identification procedure based on experimental data.

3.1 Fundamental governing equations

In the present work, relativistic effects and quantum effects are neglected. Hence, the governing laws involved for electromechanical analysis are the balance of linear momentum equation and Maxwell's, respectively Gauß's electrostatic law. The considered length scale also leads to assume the material as a continuum. Therefore, the governing relations are derived within a continuum field theory.

3.1.1 Balance of linear momentum

The rate of change of linear momentum of a material volume is equal to the net external force applied on it. For the quasi-static case, balance of linear momentum of a continuum body can be represented in local form as, [114],

$$\nabla \cdot \boldsymbol{\sigma} + \boldsymbol{b} = \mathbf{0} \quad (3.1)$$

where $\boldsymbol{\sigma}$ represents the stress tensor and \boldsymbol{b} represents the body force. Similarly, the rate of change of angular momentum is balance with the torque applied. In the absence of body couple¹, the balance of angular momentum results in

$$\boldsymbol{\sigma} = \boldsymbol{\sigma}^t \quad (3.2)$$

¹In piezoelectric material, a body couple exerts due to the presence of dipoles. However, this torque is neglected due to the very small distance between the two charges in the dipole.

The strain tensor $\boldsymbol{\varepsilon}$ is derived from the displacement field \mathbf{u} , i.e.

$$\boldsymbol{\varepsilon} = \frac{1}{2}[\nabla\mathbf{u} + \nabla\mathbf{u}^t]. \quad (3.3)$$

3.1.2 Balance of electric charges

Gauß's law states that "The net electric flux through any closed surface is proportional to the net electric charge enclosed within that closed surface", [43]. From this, the local balance of the electric charges is written mathematically as

$$\nabla \cdot \mathbf{D} = \rho, \quad (3.4)$$

where \mathbf{D} represents the electric displacement vector and ρ represents the density of the electric charge. Under the absence of a time varying magnetic field, the electric field is irrotational. Therefore, from Maxwell's third equation this can be represented as

$$\nabla \times \mathbf{E} = \mathbf{0}. \quad (3.5)$$

An irrotational vector field can be derived from the gradient of a scalar potential. Hence, the electric field can be represented as

$$\mathbf{E} = -\nabla\phi, \quad (3.6)$$

where ϕ is the electric potential given in volts.

3.2 Thermodynamic framework of constitutive modelling

In this section, a framework for deriving constitutive models for electromechanical behaviour using a thermodynamical framework is discussed. The notation $\dot{\bullet}$ represents the time derivative. From the first law of thermodynamics, i.e. the law of conservation of energy, one obtain the relations

$$\rho\dot{U} = \boldsymbol{\sigma} : \dot{\boldsymbol{\varepsilon}} - \mathbf{D} \cdot \dot{\mathbf{E}} + r - \nabla \cdot \mathbf{q}, \quad (3.7)$$

where ρ represents the mass density of the material, U represents the internal energy, r represents the heat supplied to the system per unit time and unit volume and where \mathbf{q} represents the heat flux in the material. In eq.(3.7) the left hand side represents the rate of stored internal energy per volume, the first term on the right hand side represents the input mechanical power, the second term represents the electrical power, the third term is the heat supply per unit time and unit volume and the last term represents the

divergence of heat flux. The second law of thermodynamics expressed in form of the Clausius-Duhem inequality is given by

$$\rho \dot{\eta} - \frac{r}{\theta} + \frac{\nabla \cdot \mathbf{q}}{\theta} - \frac{\mathbf{q} \cdot \nabla \theta}{\theta^2} \geq 0 \quad (3.8)$$

where η represents the entropy and θ represents the temperature. Using eq.(3.7) the Clausius-Duhem inequality can be reformulated as

$$\rho[\theta \dot{\eta} - \dot{U}] + \boldsymbol{\sigma} : \dot{\boldsymbol{\varepsilon}} - \mathbf{D} \cdot \dot{\mathbf{E}} \geq 0. \quad (3.9)$$

3.2.1 Strain driven model

The strain is considered as a control variable along with the other control variables as, e.g. the electric field. A thermodynamic free energy potential ψ is introduced as a function of control variables and internal variables as

$$\psi(\theta, \boldsymbol{\varepsilon}, \boldsymbol{\varepsilon}^i, \mathbf{E}, \mathbf{P}^i) = \rho[U - \theta\eta] \quad (3.10)$$

so that

$$\dot{\psi} = \rho[\dot{U} - \theta \dot{\eta} - \eta \dot{\theta}] \quad (3.11)$$

where $\boldsymbol{\varepsilon}^i$ and \mathbf{P}^i are irreversible strain and remnant polarisation, respectively. For isothermal conditions, the rate of temperature is zero, i.e. $\dot{\theta} = 0$, and for the uniform temperature distribution, the gradient of the temperature is zero, i.e. $\nabla \theta = \mathbf{0}$. Along with these conditions and from eq.(3.11), eq.(3.9) reduces to

$$\boldsymbol{\sigma} : \dot{\boldsymbol{\varepsilon}} - \mathbf{D} \cdot \dot{\mathbf{E}} - \dot{\psi} \geq 0 \quad (3.12)$$

where the left hand side of the equation is the rate of dissipation and is denoted by \mathcal{D} . From the fact that ψ is a function of $\boldsymbol{\varepsilon}, \boldsymbol{\varepsilon}^i, \mathbf{E}$ and \mathbf{P}^i , $\dot{\psi}$ can be written as,

$$\dot{\psi} = \frac{\partial \psi}{\partial \boldsymbol{\varepsilon}} : \dot{\boldsymbol{\varepsilon}} + \frac{\partial \psi}{\partial \mathbf{E}} \cdot \dot{\mathbf{E}} + \frac{\partial \psi}{\partial \boldsymbol{\varepsilon}^i} : \dot{\boldsymbol{\varepsilon}}^i + \frac{\partial \psi}{\partial \mathbf{P}^i} \cdot \dot{\mathbf{P}}^i. \quad (3.13)$$

Substituting eq.(3.13) by eq.(3.12) gives

$$\left[\boldsymbol{\sigma} - \frac{\partial \psi}{\partial \boldsymbol{\varepsilon}} \right] : \dot{\boldsymbol{\varepsilon}} - \left[\mathbf{D} + \frac{\partial \psi}{\partial \mathbf{E}} \right] \cdot \dot{\mathbf{E}} - \frac{\partial \psi}{\partial \boldsymbol{\varepsilon}^i} : \dot{\boldsymbol{\varepsilon}}^i - \frac{\partial \psi}{\partial \mathbf{P}^i} \cdot \dot{\mathbf{P}}^i \geq 0. \quad (3.14)$$

Here, the strain and electric field are control variables and so $\dot{\boldsymbol{\varepsilon}}$ and $\dot{\mathbf{E}}$ can be taken an arbitrarily value. Therefore, the coefficients of these variables must vanish in order to satisfy the inequality constraint. Implying this on eq.(3.14) gives

$$\boldsymbol{\sigma} = \frac{\partial \psi}{\partial \boldsymbol{\varepsilon}}, \quad (3.15)$$

$$-\mathbf{D} = \frac{\partial \psi}{\partial \mathbf{E}}, \quad (3.16)$$

$$\mathcal{D} = -\frac{\partial \psi}{\partial \boldsymbol{\varepsilon}^i} : \dot{\boldsymbol{\varepsilon}}^i - \frac{\partial \psi}{\partial \mathbf{P}^i} \cdot \dot{\mathbf{P}}^i \geq 0. \quad (3.17)$$

By specifying the free energy potential ψ , constitutive equations can be constructed by using eq.(3.15),(3.16) and (3.17).

3.2.2 Stress driven model

Most of the experimental studies on ferroelectric material performed on the material are under controlled stress environment. To mimic this situation, the models are also developed as stress driven model. In a similar fashion to strain driven models, an energy potential ψ^* is introduced as

$$\psi^*(\boldsymbol{\sigma}, \boldsymbol{\varepsilon}^i, \mathbf{E}, \mathbf{P}^i) \quad (3.18)$$

Both ψ, ψ^* can be transformed to one another by using the Legendre transformation. This transformation is given as follows

$$\psi^*(\boldsymbol{\sigma}, \boldsymbol{\varepsilon}^i, \mathbf{E}, \mathbf{P}^i) = \boldsymbol{\sigma} : \boldsymbol{\varepsilon} - \psi(\boldsymbol{\varepsilon}, \boldsymbol{\varepsilon}^i, \mathbf{E}, \mathbf{P}^i). \quad (3.19)$$

From this relation, the time derivative of these two energy potentials can be related as

$$\dot{\psi}^* = \boldsymbol{\sigma} : \dot{\boldsymbol{\varepsilon}} + \dot{\boldsymbol{\sigma}} : \boldsymbol{\varepsilon} - \dot{\psi} \quad (3.20)$$

Using this relation together with the dissipation inequality given in eq.(3.12) results in

$$-\boldsymbol{\varepsilon} : \dot{\boldsymbol{\sigma}} - \mathbf{D} \cdot \dot{\mathbf{E}} + \dot{\psi}^* \geq 0. \quad (3.21)$$

Formulating the energy potential ψ^* in terms of control variables and internal variables results in

$$\dot{\psi}^* = \frac{\partial \psi^*}{\partial \boldsymbol{\sigma}} : \dot{\boldsymbol{\sigma}} + \frac{\partial \psi^*}{\partial \mathbf{E}} \cdot \dot{\mathbf{E}} + \frac{\partial \psi^*}{\partial \boldsymbol{\varepsilon}^i} : \dot{\boldsymbol{\varepsilon}}^i + \frac{\partial \psi^*}{\partial \mathbf{P}^i} \cdot \dot{\mathbf{P}}^i. \quad (3.22)$$

Substituting eq.(3.22) by eq.(3.21) gives

$$-\left[\boldsymbol{\varepsilon} - \frac{\partial\psi^*}{\partial\boldsymbol{\sigma}}\right] : \dot{\boldsymbol{\sigma}} - \left[\mathbf{D} - \frac{\partial\psi^*}{\partial\mathbf{E}}\right] \cdot \dot{\mathbf{E}} + \frac{\partial\psi^*}{\partial\boldsymbol{\varepsilon}^i} : \dot{\boldsymbol{\varepsilon}}^i + \frac{\partial\psi^*}{\partial\mathbf{P}^i} \cdot \dot{\mathbf{P}}^i \geq 0. \quad (3.23)$$

With the argument that the rate of external variables can be arbitrarily chosen, equating the coefficients of these variables to zero in order to satisfy the inequality constraint in eq.(3.23) gives

$$\boldsymbol{\varepsilon} = \frac{\partial\psi^*}{\partial\boldsymbol{\sigma}}, \quad (3.24)$$

$$\mathbf{D} = \frac{\partial\psi^*}{\partial\mathbf{E}}, \quad (3.25)$$

$$\mathcal{D} = \frac{\partial\psi^*}{\partial\boldsymbol{\varepsilon}^i} : \dot{\boldsymbol{\varepsilon}}^i + \frac{\partial\psi^*}{\partial\mathbf{P}^i} \cdot \dot{\mathbf{P}}^i \geq 0. \quad (3.26)$$

From these results, a constitutive relations for a stress driven model can be obtained. In the same way, a stress driven model could be modified into a strain driven model by using a Legendre transformation. Even though the stress driven model resembles the experimental situation, strain driven models are preferred for the purpose of model implementation in the context of the finite element method.

3.3 Constitutive model for bulk PZT

In this section, the constitutive model for the non-linear response of ferroelectric ceramics under isothermal conditions is briefly reviewed. Rate-dependent response and polarisation processes are addressed. Ponderomotive forces are neglected and the stress tensor is assumed to be symmetric. A thermodynamic potential, defined as electric enthalpy per unit volume, is introduced as

$$\begin{aligned} \psi = & \frac{1}{2} [\boldsymbol{\varepsilon} - \boldsymbol{\varepsilon}^i] : \mathbf{E} : [\boldsymbol{\varepsilon} - \boldsymbol{\varepsilon}^i] - \frac{\|\mathbf{P}^i\|}{P_s^i} \mathbf{E} \cdot \mathbf{e} : [\boldsymbol{\varepsilon} - \boldsymbol{\varepsilon}^i] \\ & - \frac{1}{2} \mathbf{E} \cdot \boldsymbol{\varepsilon} \cdot \mathbf{E} - \mathbf{P}^i \cdot \mathbf{E} + \bar{\psi}(\mathbf{P}^i), \end{aligned} \quad (3.27)$$

wherein $\boldsymbol{\varepsilon}^i$ denotes the irreversible strain contribution due to switching and where \mathbf{P}^i is the corresponding polarisation contribution which, in the following, is introduced as an internal variable. Moreover, the underlying constitutive tensors are assumed as

$$\mathbf{E} = \lambda \mathbf{I} \otimes \mathbf{I} + 2\mu \mathbf{I}^{\text{sym}}, \quad (3.28)$$

$$\boldsymbol{\epsilon} = -2\gamma \mathbf{I}, \quad (3.29)$$

$$\mathbf{e} = -\beta_1 \mathbf{a} \otimes \mathbf{I} - \beta_2 \mathbf{a} \otimes \mathbf{a} \otimes \mathbf{a} - \frac{1}{2} \beta_3 [\mathbf{I} \otimes \mathbf{a} + \mathbf{I} \otimes \bar{\mathbf{a}}]. \quad (3.30)$$

The vector \mathbf{a} represents the polarisation direction $\mathbf{P}^i / \|\mathbf{P}^i\|$. The scalars P_s^i , λ , μ , γ , β_1 , β_2 and β_3 are material parameters. The initial reference state is assumed to be stress-free with vanishing dielectric displacements. The energetic part $\bar{\psi}$ represents the contribution stored by the internal variables and may be interpreted as a hardening-type function. It is assumed to depend only on the internal state variables of the material and is specified as

$$\bar{\psi} = -a \|\mathbf{P}^i\| \operatorname{arctanh} \left(\frac{\|\mathbf{P}^i\|}{P_s} \right) + \frac{a P_s}{2} \ln \left(1 - \frac{\|\mathbf{P}^i\|^2}{P_s^2} \right). \quad (3.31)$$

Based on this, the local dissipation contribution takes the representation

$$\begin{aligned} \mathcal{D} &= \boldsymbol{\sigma} : \dot{\boldsymbol{\varepsilon}} - \mathbf{D} \cdot \dot{\mathbf{E}} - \dot{\psi} \\ &= \left[\boldsymbol{\sigma} - \frac{\partial \psi}{\partial \boldsymbol{\varepsilon}} \right] : \dot{\boldsymbol{\varepsilon}} - \left[\mathbf{D} + \frac{\partial \psi}{\partial \mathbf{E}} \right] : \dot{\mathbf{E}} - \frac{\partial \psi}{\partial \boldsymbol{\varepsilon}^i} : \dot{\boldsymbol{\varepsilon}}^i - \frac{\partial \psi}{\partial \mathbf{P}^i} : \dot{\mathbf{P}}^i \\ &\geq 0. \end{aligned} \quad (3.32)$$

Applying standard arguments of continuum thermodynamics, cf. Coleman and Noll [26], the stresses and dielectric displacements are introduced as

$$\boldsymbol{\sigma} = \frac{\partial \psi}{\partial \boldsymbol{\varepsilon}} = \mathbf{E} : [\boldsymbol{\varepsilon} - \boldsymbol{\varepsilon}^i] - \frac{\|\mathbf{P}^i\|}{P_s^i} \mathbf{E} \cdot \mathbf{e}, \quad (3.33)$$

$$-\mathbf{D} = \frac{\partial \psi}{\partial \mathbf{E}} = -\frac{\|\mathbf{P}^i\|}{P_s^i} \mathbf{e} : [\boldsymbol{\varepsilon} - \boldsymbol{\varepsilon}^i] - \boldsymbol{\varepsilon} \cdot \mathbf{E} - \mathbf{P}^i. \quad (3.34)$$

In the following, irreversible strains are assumed to possess a one to one relation to the remnant polarisation, i.e.

$$\boldsymbol{\varepsilon}^i = \frac{3}{2} \frac{\varepsilon_s^i}{P_s^{i2}} [\mathbf{P}^i \otimes \mathbf{P}^i] : \mathbf{P}, \quad (3.35)$$

where ε_s^i is a material parameter and the fourth-order symmetric deviatoric projection tensor is defined as $\mathbf{P} = \mathbf{I}^{\text{sym}} - \frac{1}{3} \mathbf{I} \otimes \mathbf{I}$. Note, that $\boldsymbol{\varepsilon}^i$ is assumed to be quadratic

in the remnant polarisation \mathbf{P}^i . With this assumption at hand, the local dissipation contribution remaining reduces to

$$\mathcal{D}_{\text{red}} = - \left[\frac{\partial \psi}{\partial \boldsymbol{\varepsilon}^i} : \frac{\partial \boldsymbol{\varepsilon}^i}{\partial \mathbf{P}^i} + \frac{\partial \psi}{\partial \mathbf{P}^i} \right] \cdot \dot{\mathbf{P}}^i = \left[3 \frac{\varepsilon_s^i}{P_s^i{}^2} [\boldsymbol{\sigma} : \mathbf{P}] \cdot \mathbf{P}^i - \frac{\partial \psi}{\partial \mathbf{P}^i} \right] \cdot \dot{\mathbf{P}}^i \geq 0. \quad (3.36)$$

Following the work by Miehe and Rosato [84], the quantity energetically conjugate to the remnant polarisation is approximated such that its stress-based contribution is neglected and, moreover, the simplification

$$\widehat{\mathbf{E}} = - \frac{\partial \psi}{\partial \mathbf{P}^i} \approx \mathbf{E} - \frac{\partial \bar{\psi}}{\partial \mathbf{P}^i} = \mathbf{E} - \left[a \operatorname{arctanh} \left(\frac{\|\mathbf{P}^i\|}{P_s^i} \right) \right] \frac{\mathbf{P}^i}{\|\mathbf{P}^i\|} \quad (3.37)$$

is used, which results in $\mathcal{D}_{\text{red}} \approx \widehat{\mathbf{E}} \cdot \dot{\mathbf{P}}^i \geq 0$. Next, a switching threshold function $\Phi(\widehat{\mathbf{E}})$ is introduced that controls the activation of domain switching. In the case of reversible processes $\Phi < 0$ holds, whereas $\Phi \geq 0$ is permitted for rate-dependent irreversible processes. The particular switching function adopted is

$$\Phi = \frac{\widehat{\mathbf{E}} \cdot \widehat{\mathbf{E}}}{E_c^2} - 1 = 0, \quad (3.38)$$

wherein the coercive electric field value E_c is a material parameter. With these relations in hand, (associated) Perzyna-type evolution equations are adopted which results in

$$\dot{\mathbf{P}}^i = \frac{\langle \Phi \rangle^m}{\eta} \frac{\partial \Phi}{\partial \widehat{\mathbf{E}}} = \frac{\langle \Phi \rangle^m}{\eta} \frac{2}{E_c^2} \widehat{\mathbf{E}}, \quad (3.39)$$

with $\langle \bullet \rangle = \frac{1}{2} [\bullet + |\bullet|]$ denoting the Macauley brackets, so that the simplified dissipation inequality reduces to a quadratic form in $\widehat{\mathbf{E}}$. The material parameters $\eta > 0$ as well as $m > 0$ influence the rate-dependent response of the electromechanical model.

In view of the numerical integration scheme to update the internal variable \mathbf{P}^i , an implicate Euler backward algorithm is applied. Considering a finite time interval with $\Delta t = t_{n+1} - t_n > 0$, the actual remnant polarisation \mathbf{P}_{n+1}^i can be determined iteratively from the residual form

$$\mathbf{P}_{n+1}^i - \mathbf{P}_n^i - \Delta t \lambda_{n+1} \frac{2}{E_c^2} \widehat{\mathbf{E}}(\mathbf{E}_{n+1}, \mathbf{P}_{n+1}^i) = \mathbf{0}, \quad (3.40)$$

where $\lambda_{n+1} = \langle \Phi_{n+1} \rangle^m / \eta$. As this work proceeds, quantities without any index related to time are referred to t_{n+1} .

An algorithmic sketch of a constitutive driver for the discussed constitutive model is given in Tab. 5.1. This algorithm solves for $\boldsymbol{\varepsilon}$ and \mathbf{D} for given $\boldsymbol{\sigma}^{\text{ext}}$ and \mathbf{E} , where $\boldsymbol{\sigma}^{\text{ext}}$ refers to the given external stresses.

Table 3.1: Algorithmic sketch of the constitutive driver for the rate dependent response of ferroelectric bulk material.

Given: $\sigma_{n+1}^{\text{ext}}, \mathbf{E}_{n+1}, \varepsilon_n, \mathbf{P}_n^i$ Set: $\varepsilon_{n+1} = \varepsilon_n, \mathbf{P}_{n+1}^i = \mathbf{P}_n^i$ Compute: $\mathbf{R}_l, \mathbf{R}_g$ DOWHILE: $\ \mathbf{R}_g\ \geq \text{tol}_g$ DOWHILE: $\ \mathbf{R}_l\ \geq \text{tol}_l$ Compute: $\sigma_{n+1}, \mathbf{D}_{n+1}$ using Eq. (6.2) and (6.3) $\mathbf{R}_l = \mathbf{P}_{n+1}^i - \mathbf{P}_n^i - \Delta t \lambda_{n+1} \frac{2}{E_c^2} \left[\mathbf{E}_{n+1} + \frac{\partial \bar{\psi}}{\partial \mathbf{P}_{n+1}^i} \right]$ $\mathbf{P}_{n+1}^i \leftarrow \mathbf{P}_{n+1}^i - \left[\frac{d\mathbf{R}_l}{d\mathbf{P}_{n+1}^i} \right]^{-1} \cdot \mathbf{R}_l$ END $\mathbf{R}_g = \sigma_{n+1}^{\text{ext}} - \sigma_{n+1}$ $\varepsilon_{n+1} \leftarrow \varepsilon_{n+1} - \left[\frac{d\mathbf{R}_g}{d\varepsilon_{n+1}} \right]^{-1} : \mathbf{R}_g$ END

3.4 Results

This section presents experimental and simulation results for bulk PZT for different electrical loading frequencies. This includes calibration of the underlying material parameters. Material parameters related to the linear piezoelectric behaviour are taken from the manufacturer datasheet, whereas the parameters for inelastic rate-dependent behaviour are obtained from a calibration procedure based on experimental data. To be specific, a least squares functional in terms of differences between measured and simulated response is used and minimised over the set of material parameters. This calibration scheme simultaneously includes experimental data for all frequencies considered within one single least squares functional so that only one set of material parameters is identified for all loading frequencies. The specific functional used is

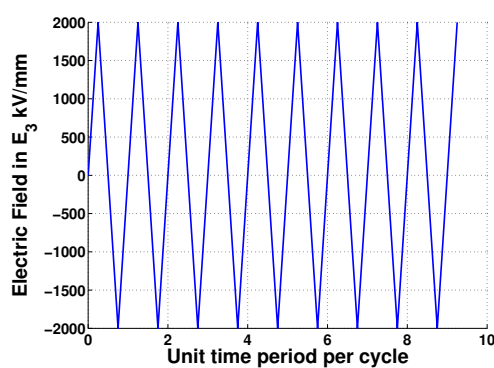
$$f = \min_{\boldsymbol{\kappa}} \left\{ \sum_{j=1}^p w_j [S_j^{\text{sim}}(\boldsymbol{\kappa}) - S_j^{\text{exp}}]^2 \right\} \quad (3.41)$$

where $\boldsymbol{\kappa} = \{E_c, P_s^i, \varepsilon_s^i, a, \eta\}$ is the set of material parameters to be identified. The values S_j^{sim} refer to the result of the simulation and S_j^{exp} are experimentally determined values at the same time step. The parameter m is set to be 1 while the calibration procedure is performed. Moreover, p represents the number of data points accounted for and w_j are additional weighing factors. For the experimentally determined values, S_j^{exp} ,

Table 3.2: Material parameters for bulk PZT.

param.	name	unit	value
λ	Lamé parameter	kN/m ²	91.6 $\times 10^6$
μ	Lamé parameter	kN/m ²	18.86 $\times 10^6$
β_1	Piezoelectric coupling parameter	C/m ²	3.84
β_2	Piezoelectric coupling parameter	C/m ²	-17.44
β_3	Piezoelectric coupling parameter	C/m ²	-17.76
γ	Electric permittivity	C ² /(kN m ²)	-8.11 $\times 10^6$
E_c	Coercive electric field	kV/m	1.34
P_s^i	Saturation polarisation	C/m ²	0.311 $\times 10^3$
ε_s^i	Saturation strain	-	1.854 $\times 10^{-3}$
a	Hardening parameter	C/m ²	3.02 ⁻¹
m	Viscosity shape exponent	-	1
η	Viscosity shape exponent	m ² /(C s)	6.25 $\times 10^{-2}$

the experimental data of ferroelectric response and butterfly curve at electrical loading frequencies of 1 Hz, 5 Hz, 10 Hz, and 25 Hz are used. The least square functional used for the parameter calibration simultaneously includes the data of the hysteresis loops and butterfly curves of all loading frequencies considered. Due to the rate dependent effect, the unsteady state part of the simulation result is omitted by applying continuous cycles of electrical loading until the steady state results are achieved. The loading cycle for the simulation is given in Fig. 3.1. The last cycle of the simulation results, which reflects the steady state simulation results, are used as S^{sim} for the material parameter identification. The material parameters calibrated for the bulk PZT material are summarised in Tab. 5.2.

**Figure 3.1:** Loading cycle for bulk PZT.

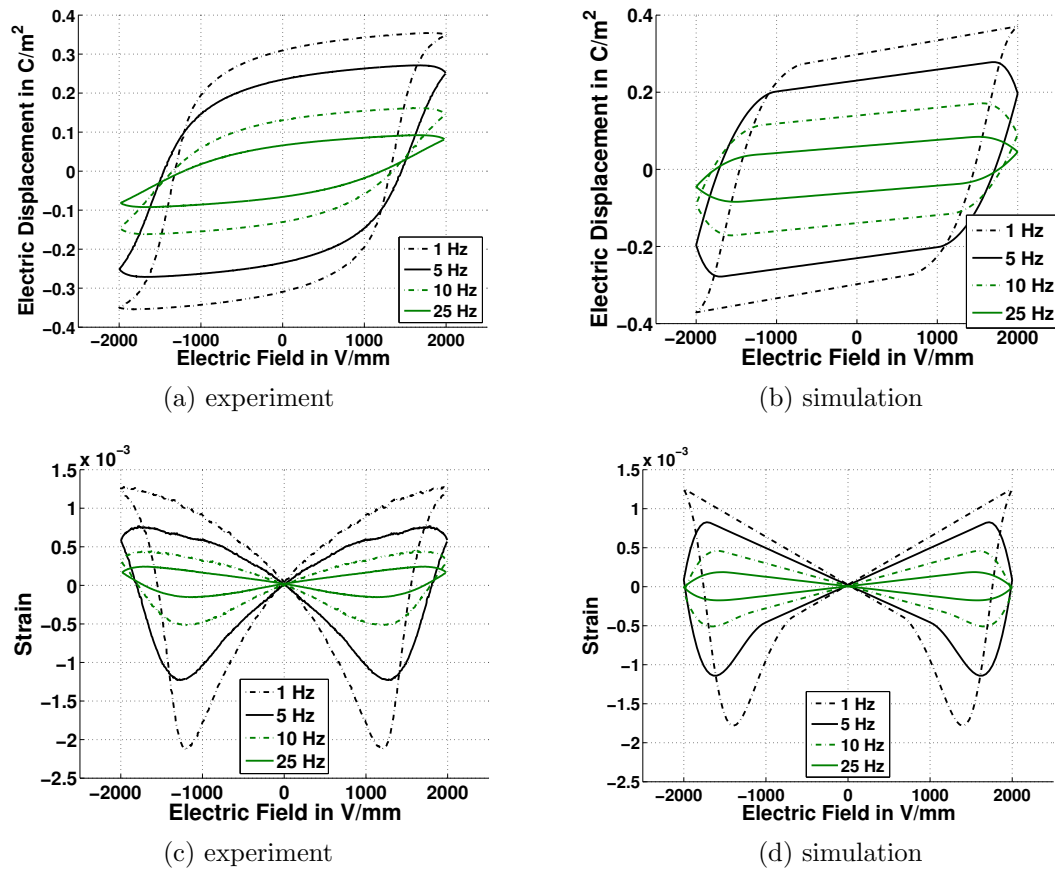


Figure 3.2: Rate dependent ferroelectric hysteresis at electrical loading of 1 Hz, 5 Hz, 10 Hz and 25 Hz: (a,c) experimental data and (b,d) simulation of hysteresis loops and butterfly curves for bulk PZT.

The simulation results for the ferroelectric behaviour, as represented by typical hysteresis and butterfly curves, are discussed for different electrical loading frequencies, namely 1 Hz, 5 Hz, 10 Hz, and 25 Hz; see Fig. 3.2. The simulation results show a good agreement with the experimental data. From the comparison between experimental data and simulation results of ferroelectric hysteresis curves, it can be seen that the simulation results capture the remnant polarisation very well for all frequencies considered. The experimental results show the increase in the coercive electric field as the frequency of the loading increases. This effect is also observed in the simulation results. Since poled ferroelectric specimens are used for the experiments, the polarised state is considered as the reference state for the strain. Therefore, for the comparison between the experimental data and the simulation results of butterfly curves, the remnant strain of the simulation results is shifted to zero strain. From this comparison, the simulation results reasonably match with the experimental data. The change in strain at low frequencies of loading due to polarisation switching is observed to be smaller within the simulation results than for the experiments. Within the experiments at 1 Hz, the com-

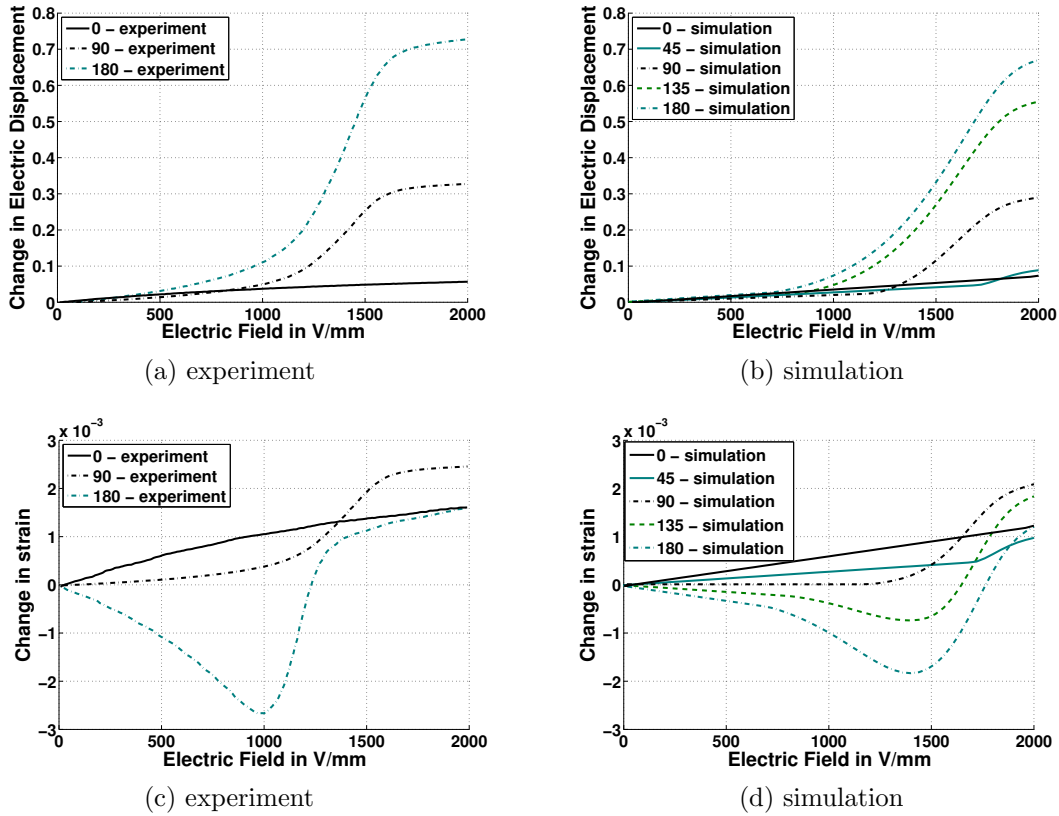


Figure 3.3: Polarization rotation curves of experiments(a,c) and simulation results(b,d) for various loading angles between the direction of polarisation and the direction of electrical loading for bulk PZT.

pressive strain goes up to 2.1×10^{-3} during the polarisation switching. The simulated strains, however, approach a value of up to -1.8×10^{-3} .

Moreover, polarisation rotation tests are simulated for different angles. The initial conditions are assumed such that the material is poled in a certain direction and the electric field is applied at an angle to this initial poling direction. Simulations are performed for the applied electric field for the angles 0° , 45° , 90° , 135° and 180° . The change in electric displacement and the change in strain are calculated and compared with the related experimental data. From the comparison given in Fig. 3.3, the change in electric displacement due to the polarisation rotation test is very well captured. Even though the comparison of change in strain is in good agreement, the polarisation rotation at 180° does not perfectly match the experimental data.

3.5 Summary and conclusions

From the experimental results, the frequency dependence of the ferroelectric behaviour is very well observed. As the frequency increases, the remnant polarisation and remnant strain decrease. This behaviour is due to the fact that, at higher rate of loading, the time taken for the domain switching process becomes comparable with the time taken for one complete cycle of loading. As a result, at a higher frequencies, even before the completion of domain switching process, the external loading reverses the applied direction and consequently attenuates the completion of domain switching. Due to this fact, as the frequency of loading increases, the process of domain switching reduces. Therefore, a notable reduction of polarisation and strain is observed as the frequency of loading increases. Moreover, the study of frequency dependence is important for the design of large displacement actuators by providing the limitation of displacement output for the required frequency of actuation. Therefore, a rate dependent ferroelectric model is required in order to analyse such cases. To capture the loading frequency dependent behaviour, a rate dependent ferroelectric model has been developed. The material parameters are then predicted using a parameter identification procedure. With these identified parameters, the simulation results are then compared with the experimental data. From the simulation results, the experimental data of ferroelectric hysteresis curves are very well captured by the model. This model could also be extended to implement within a finite element framework. In chapter 7, this model will be used for predicting the effective ferroelectric behaviour of 1-3 piezocomposites. Even though, this model could capture the rate dependent ferroelectric behaviour, it lacks in predicting the asymmetric butterfly hysteresis behaviour and also minor hysteresis loop due to the change in maximum applied electric field. In the following chapter, a model able to predict these behaviour is introduced.

4 A multi-surface model for ferroelectric ceramics

The model introduced in the previous chapter is able to capture the rate dependent response of ferroelectric behaviour. Concerning the behaviour of minor ferroelectric hysteresis and asymmetric butterfly hysteresis, however, that model is limited. Therefore, a new model is presented in this chapter, which is able to capture minor ferroelectric hysteresis and asymmetric butterfly hysteresis behaviour. In this context, a multisurface ferroelectric model is introduced. This chapter starts with the motivation for the multi-surface model along with a discussion of experimental results. Following that, a modelling framework for the constitutive response is introduced. Finally, the simulation results are presented together with the comparison to experimental data. This chapter is concluded with a discussion on further extension of this model.

4.1 Motivation for multi-surface model and experimental data

In a polycrystalline ferroelectric material, ferroelectric hysteresis behaviour is caused due to the ferroelectric domain switching. Upon applying an electrical load, a defined potential for the switching criteria reaches the critical value. Once the potential reaches this critical value, domain switching takes place. In a phenomenological model, the domain switching phenomenon is a result of the change in remnant polarisation. This domain switching does not take place in all the domains simultaneously and therefore requires different switching criteria for different grains. The reasons for varying switching criteria for different grains are the orientation of the domains, size of the grain and interface effects from adjacent grains. Due to these reasons, at the macroscopic scale, hardening behaviour of the ferroelectric switching is observed. In a fully poled material, undergoing ferroelectric switching with medium amplitude of the external cyclic electrical field, domains with low threshold limit switch with respect to the applied field which results in the hysteresis. At the same time, the remaining domains remain to be oriented in poled direction. Due to these non-switching domains, a polarisation offset can be observed, which results in a shift of the hysteresis curve with respect to the electric field axis. This offset polarisation can be seen in the results of the experimental investigation carried out at the laboratory at the Department of Applied Mechanics at the Indian Institute of Technology Madras, shown in Fig. 4.1.

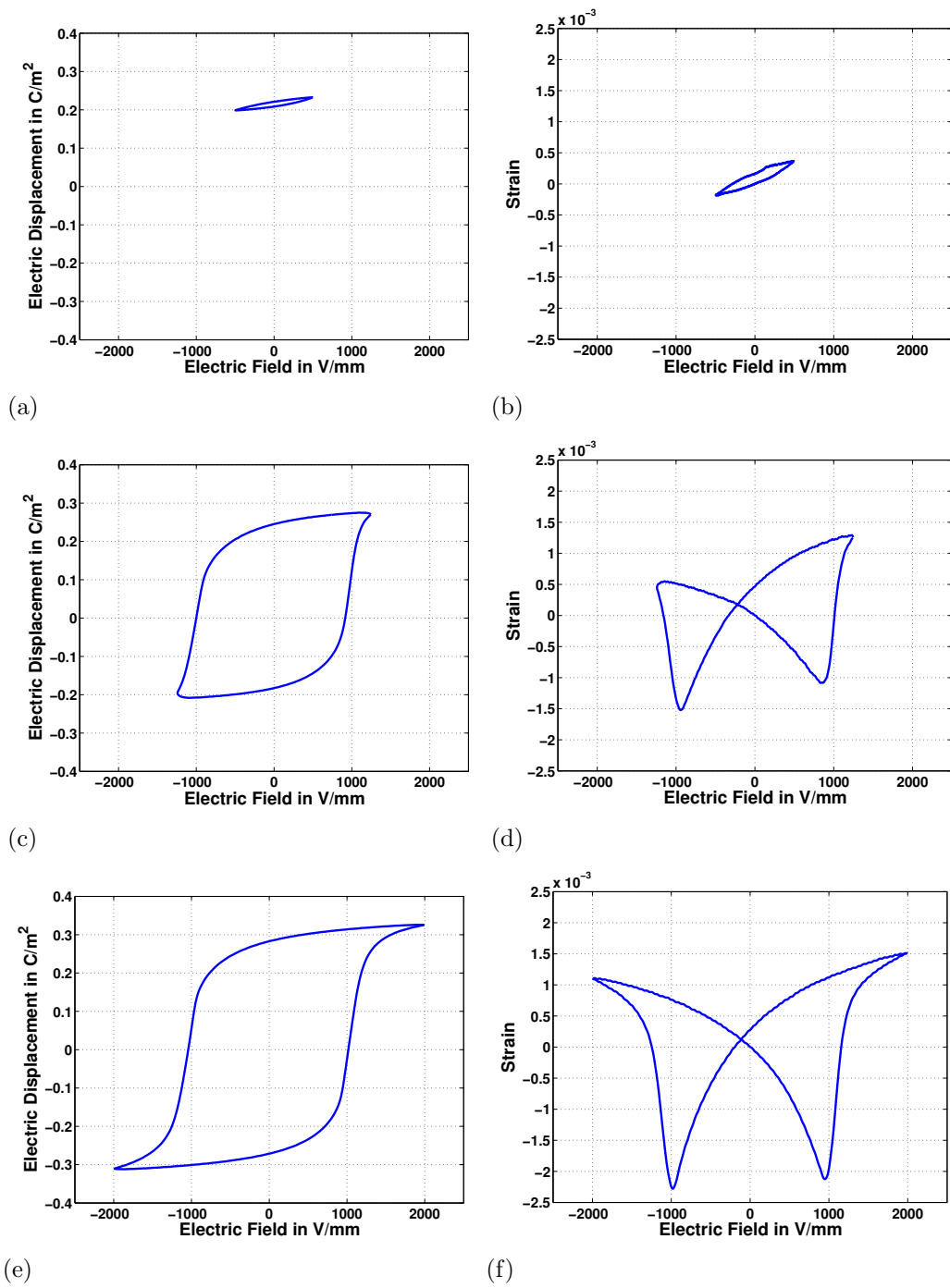


Figure 4.1: Experimental data for dielectric hysteresis (a, c, e) and butterfly hysteresis (b, d, f) of PZT5A1 for a linearly increasing and decreasing electric field (triangular shaped cyclic loading) with amplitudes of 500 V/mm, 1250 V/mm and 2000 V/mm [79].

In this work, ferroelectric behaviour of a piezoelectric material is experimentally investigated for various loading amplitudes. The amplitudes 500 V/mm, 1250 V/mm and 2000 V/mm are chosen such that the behaviour shows minor hysteresis loops, major hysteresis loops and asymmetric butterfly hysteresis. The test samples used for the experiments are disc specimens of PZT5A1 SP502 with a 10 mm diameter and 1 mm thickness, provided by CeramTec GmbH. A bipolar cyclic electric field is applied at 1 Hz. For an illustration of the experimental setup, we refer to Jayendiran et al. [55]. To measure the dielectric hysteresis, a Sawyer tower circuit is used. This circuit measures only the relative electric displacement with respect to the initial polarisation. Therefore, a constant initial polarisation is chosen to shift the reference state of the polarisation so that the offset polarisation is zero for large electrical loading amplitudes.

Offset polarisation in dielectric hysteresis as well as asymmetric behaviour in the butterfly hysteresis are also observed in the ferroelectric material which has undergone electrical fatigue, see [77], as shown in Fig. 4.2. From this figure, it is observed that upon increasing the maximum amplitude of the bipolar cyclic electrical loading, the offset polarisation reduces. At a later stage when the maximum amplitude decreases, the offset polarisation remains zero.

In order to model the asymmetric behaviour of fatigued specimen, the offset polarisation is introduced as a material parameter by Nuffer et al. [90]. The total polarisation is additively decomposed into switching polarisation and offset polarisation. For the simulation of asymmetric behaviour in fatigue, spontaneous polarisation is considered as one internal variable which evolves with respect to the applied electric field and the offset polarisation which evolves with respect to the number of loading cycles. In this regard, two internal variables are introduced which both evolve independently. In a similar fashion, more than one independent remnant polarisation contribution can be introduced for asymmetric ferroelectric behaviour due to the amplitude variation. In this context, a Mroz-type multi-surface model, see Mroz [87], is used with irreversible polarisation instead of irreversible plastic strains.

As this work proceeds, a constitutive model for ferroelectric material with multi-switching surface is developed. Later, the model is implemented for the numerical analysis. The material parameters are identified based on experimental results. In [77], where material which has undergone electrical fatigue is investigated, a difference in ferroelectric behaviour has been observed for increasing and decreasing electric loading. Such loading is also used for the simulation analysis for the motivation of extending the model to fatigue analysis. To show the capability in capturing the behaviour for multiaxial loading, simulation results of polarisation rotation curves are presented.

4.2 Constitutive model

In order to develop a constitutive model within a thermodynamic framework, an energy function in terms of state variables is introduced. In this work, along with the external state variables, i.e. strain $\boldsymbol{\varepsilon}$ and electric field \boldsymbol{E} , remnant polarisation are considered as

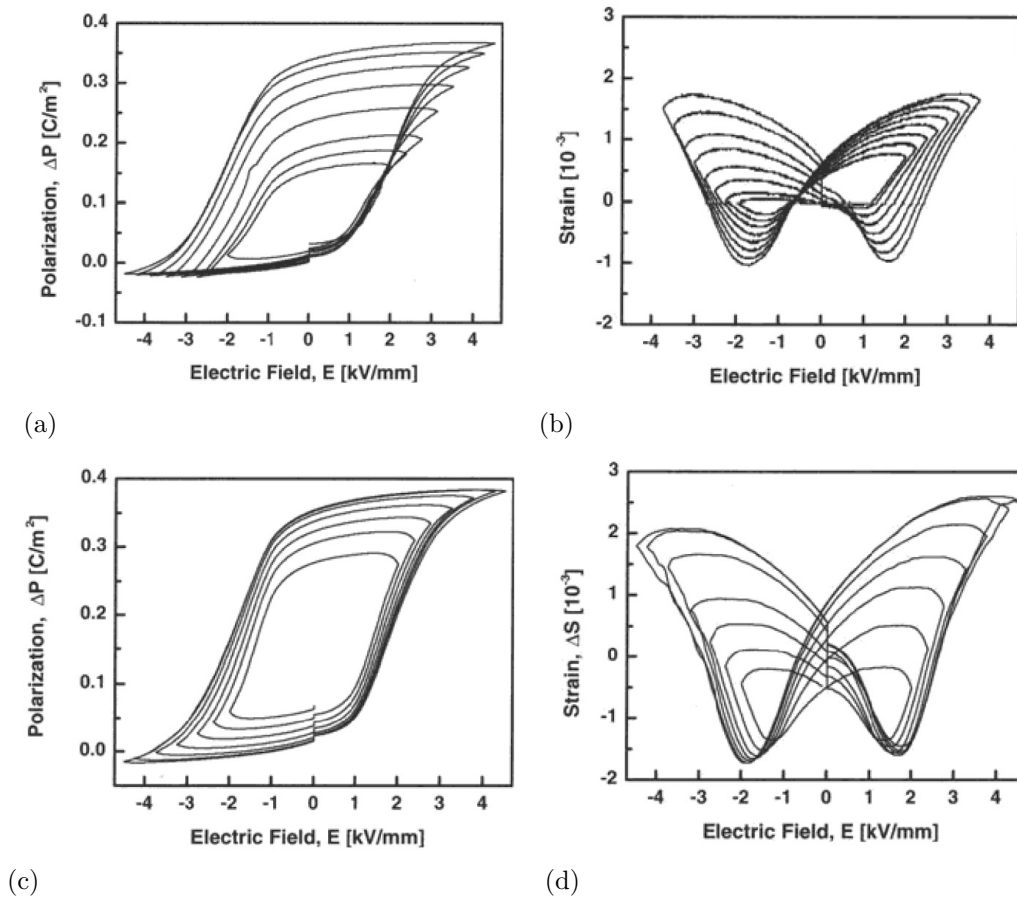


Figure 4.2: Ferroelectric hysteresis behaviour under bipolar electrical loading of a fatigued specimen of PIC 151 with increasing (a,b) and decreasing (c,d) amplitude of the maximum applied electric field, taken from Lupascu [77].

internal state variables. For the multi-surface modelling approach proposed, the total remnant polarisation \mathbf{P}_T^i is additively decomposed into a set of N independent remnant polarisation contributions $\mathbf{P}_{1,\dots,N}^i$. The relation between the total polarisation and the set of remnant polarisation is given as

$$\mathbf{P}_T^i = \mathbf{P}_0^i + \sum_{j=1}^N \mathbf{P}_j^i. \quad (4.1)$$

In a prepoled material, certain domains require very large applied electric fields along with a temperature rise in order to switch from the poled direction. In order to account for these frozen domains, a constant offset polarisation is introduced as \mathbf{P}_0^i . Based on the loading history and the external load, this offset polarisation will be chosen. This offset polarisation can be ignored for unpoled material. Remnant strains arising due to the domain switching are considered to be dependent on the total remnant polarisation. Therefore this strain is derived from a one to one relation which is given as

$$\boldsymbol{\varepsilon}^{\text{pi}} = \frac{3\varepsilon_s^i}{2} \left[\frac{\|\mathbf{P}_T^i\|}{P_s^i} \right]^{3/2} [\mathbf{a} \otimes \mathbf{a}] : \mathbf{P}, \quad (4.2)$$

where \mathbf{a} is defined as the direction of remnant polarisation given as $\mathbf{a} = \mathbf{P}_T^i / \|\mathbf{P}_T^i\|$. The parameters P_s^i and ε_s^i are the saturation remnant polarisation value and the saturation strain value, respectively. Instead of linear, [59], or quadratic, [65], power relations in eq.(4.2), the value 3/2 has been chosen which in view of predicting experimental data by the model proposed as this work proceeds turned out to be reasonable. To account for ferroelastic behaviour, an additional irreversible strain $\boldsymbol{\varepsilon}^{\text{si}}$ can be considered so that the total irreversible strain $\boldsymbol{\varepsilon}^i$ is additively decomposed as

$$\boldsymbol{\varepsilon}^i = \boldsymbol{\varepsilon}^{\text{pi}} + \boldsymbol{\varepsilon}^{\text{si}}. \quad (4.3)$$

4.2.1 Energy functions and flux terms

As a function of independent state variables (at constant temperature), the free energy per unit volume is introduced as

$$\begin{aligned} \psi(\boldsymbol{\varepsilon}, \mathbf{E}, \mathbf{P}_1^i, \dots, \mathbf{P}_N^i) = & \frac{1}{2} [\boldsymbol{\varepsilon} - \boldsymbol{\varepsilon}^i] : \mathbf{E} : [\boldsymbol{\varepsilon} - \boldsymbol{\varepsilon}^i] - \frac{\|\mathbf{P}_T^i\|}{P_s^i} \mathbf{E} \cdot \mathbf{e} : [\boldsymbol{\varepsilon} - \boldsymbol{\varepsilon}^i] \\ & - \frac{1}{2} \mathbf{E} \cdot \boldsymbol{\varepsilon} \cdot \mathbf{E} - \mathbf{P}_T^i \cdot \mathbf{E} + \bar{\psi}_1(\mathbf{P}_1^i, \dots, \mathbf{P}_N^i) + \bar{\psi}_2(\boldsymbol{\varepsilon}^{\text{si}}). \end{aligned} \quad (4.4)$$

The last two terms in the energy potential in eq.(4.4), $\bar{\psi}_1$ and $\bar{\psi}_2$, represent the free energy stored by the remnant polarisation contribution and can be considered as hardening contributions of the internal variables. The term $\bar{\psi}_1$ is specified as

$$\bar{\psi}_1 = \sum_{j=1}^N -a_j \|\mathbf{P}_j^i\| \operatorname{arctanh} \left(\frac{\|\mathbf{P}_j^i\|}{\alpha_j P_s^i} \right) + \frac{\alpha_j a_j P_s^i}{2} \ln \left(1 - \frac{\|\mathbf{P}_j^i\|^2}{[\alpha_j P_s^i]^2} \right), \quad (4.5)$$

see Schroeder et al. [100], wherein the scalar values α_j are the factors which represent the fraction of polarisation associated to the respective internal variable and the values a_j are hardening parameters. The scalars $\alpha_j > 0$ have to be chosen such that $[1 - \sum_{j=1}^N \alpha_j] P_s^i = \|\mathbf{P}_0^i\|$. Based on the work by Landis [72], see also Klinkel [65], the derivative of the contribution $\bar{\psi}_2$ can be introduced as

$$\frac{\partial \bar{\psi}_2}{\partial \boldsymbol{\varepsilon}^{\text{si}}} = \sum_{a=1}^3 \frac{h \varepsilon_a^{\text{si}}}{[1 + 2 \varepsilon_a^{\text{si}} / \varepsilon_s^i][1 - \varepsilon_a^{\text{si}} / \varepsilon_s^i]} \mathbf{n}_a \otimes \mathbf{n}_a, \quad (4.6)$$

wherein h is a material parameter and $\varepsilon_a^{\text{si}}$ and \mathbf{n}_a represent the eigenvalues and eigenvectors of $\boldsymbol{\varepsilon}^{\text{si}}$, respectively.

Following standard arguments of continuum thermodynamics, cf. Coleman and Noll [26], the stresses and dielectric displacements take the representation as

$$\boldsymbol{\sigma} = \frac{\partial \psi}{\partial \boldsymbol{\varepsilon}} = \mathbf{E} : [\boldsymbol{\varepsilon} - \boldsymbol{\varepsilon}^i] - \frac{\|\mathbf{P}_T^i\|}{P_s^i} \mathbf{e}^t \cdot \mathbf{E}, \quad (4.7)$$

$$-\mathbf{D} = \frac{\partial \psi}{\partial \mathbf{E}} = -\frac{\|\mathbf{P}_T^i\|}{P_s^i} \cdot \mathbf{e} : [\boldsymbol{\varepsilon} - \boldsymbol{\varepsilon}^i] - \boldsymbol{\varepsilon} \cdot \mathbf{E} - \mathbf{P}_T^i. \quad (4.8)$$

4.2.2 Evolution equations of internal variables

Evolution equations of internal variables are obtained from maximizing the dissipation contribution. The procedure for developing the evolution equation is based on the work by Miehe and Rosato [84]. The local dissipation contribution is given as the sum of the product of all internal variables with their energy conjugates. A rate dependent model shall be established which, from an algorithmic point of view, has the advantage that the current loading state does not need to satisfy the switching function itself (i.e. the constraints $\dot{\Phi}_j \leq 0$ and $\dot{\Phi}_s \leq 0$) as in the case of rate independent response. Hence, to deal with the rate dependent behaviour, a penalty function is added and the dissipation function is introduced as

$$\mathcal{D} = \sum_{j=1}^N \widehat{\mathbf{E}}_j \cdot \dot{\mathbf{P}}_j^i + \widehat{\boldsymbol{\sigma}} : \boldsymbol{\varepsilon}^{\text{si}} - \frac{1}{\eta_j [m_j + 1]} \langle \dot{\Phi}_j \rangle^{m_j+1} - \frac{1}{\eta_s [m_s + 1]} \langle \dot{\Phi}_s \rangle^{m_s+1} \geq 0 \quad (4.9)$$

with $\langle \bullet \rangle = \frac{1}{2} [\bullet + |\bullet|]$ denoting the Macauley brackets. The material parameters $\eta_j > 0$ and $\eta_s > 0$ as well as $m_j > 0$ and $m_s > 0$ influence the rate-dependent response of the electromechanical model. The functions Φ_j represent the switching criteria given for each remnant polarisation and introduced as

$$\Phi_j = \frac{\widehat{\mathbf{E}}_j \cdot \widehat{\mathbf{E}}_j}{jE_c^2} - 1. \quad (4.10)$$

The coercive values jE_c are material parameters for the corresponding yield surface. The function Φ_s represents the switching criterion for the irreversible strain and is introduced as

$$\Phi_s = \frac{\widehat{\boldsymbol{\sigma}} : \widehat{\boldsymbol{\sigma}}}{\sigma_c^2} - 1, \quad (4.11)$$

wherein σ_c represents the coercive stress value. The energy conjugate of remnant polarisations, $\widehat{\mathbf{E}}_j$, and the energy conjugate of irreversible strain, $\widehat{\boldsymbol{\sigma}}$, are defined as

$$\widehat{\mathbf{E}}_j = -\frac{\partial \psi}{\partial \mathbf{P}_j^i} \approx \mathbf{E} - \frac{\partial \bar{\psi}}{\partial \mathbf{P}_j^i}, \quad (4.12)$$

$$\widehat{\boldsymbol{\sigma}} = -\frac{\partial \psi}{\partial \boldsymbol{\varepsilon}^{si}}. \quad (4.13)$$

In the present work, the main focus is placed on the ferroelectric behaviour of the material. Hence, the ferroelastic contributions are neglected in the following. Based on the maximum dissipation hypothesis, evolution equations for the internal variables \mathbf{P}_j^i are obtained from the derivatives of eq.(4.10) with respect to $\widehat{\mathbf{E}}_j$, i.e.

$$\dot{\mathbf{P}}_j^i = \lambda_j \frac{\partial \Phi_j}{\partial \widehat{\mathbf{E}}_j} = \lambda_j \frac{2}{jE_c^2} \widehat{\mathbf{E}}_j = \lambda_j \frac{2}{jE_c^2} \left[\mathbf{E} - \frac{\partial \bar{\psi}}{\partial \mathbf{P}_j^i} \right], \quad (4.14)$$

wherein $\lambda_j = \eta_j^{-1} \langle \Phi_j \rangle^{m_j}$. Based on eq.(4.5), the last contribution in eq.(4.14) takes the representation

$$\frac{\partial \bar{\psi}}{\partial \mathbf{P}_j^i} = a_j \operatorname{arctanh} \left(\frac{\|\mathbf{P}_j^i\|}{\alpha_j P_s^i} \right) \frac{\mathbf{P}_j^i}{\|\mathbf{P}_j^i\|}. \quad (4.15)$$

4.2.3 Graphical illustration of the multi-surface model

In this section, an illustration of the constitutive model is highlighted in order to discuss the ability of the model capturing different phenomena exhibited from the experimental

investigation of the material studied. Fig. 4.3 shows a modified single switching surface in the space of the electrical field.

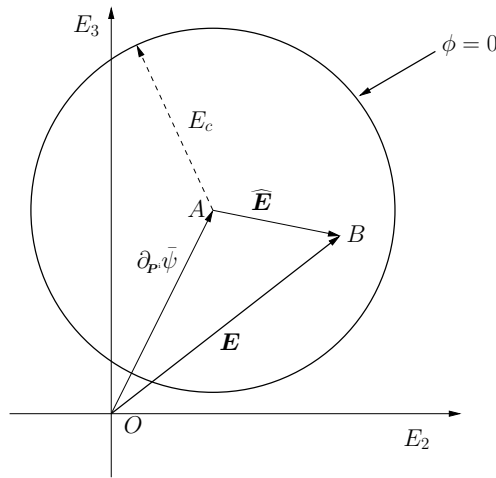


Figure 4.3: Illustration of the switching surface in the space of the electrical field.

This modified switching surface is given in the following equation as

$$\phi_j = {}^j E_c^2 \Phi_j. \quad (4.16)$$

The circle in Fig. 4.3 represents the projection of the modified switching surface in $E_2 - E_3$ plane. Point 'B' represents the state of the current applied electrical field with $E_2 = \mathbf{E} \cdot \mathbf{e}_2$ and $E_3 = \mathbf{E} \cdot \mathbf{e}_3$. Point 'A' represents the center of the yield surface. The distance of point 'A' from the origin can be interpreted as the magnitude of remnant polarisation, cf. eq.(4.15). However, the polarisation value is limited to a saturation polarisation by choosing an appropriate hardening function. Fig. 4.4 illustrates the relation between the magnitude of \overline{OA} and the normalised polarisation $\|\mathbf{P}^i\|/P_s^i$. The radius of the yield surface in Fig. 4.3 does not change and remains equal to E_c in order to represent kinematic hardening. As point 'B' remains within the switching surface, switching phenomena do not occur and therefore the relation between the electric field and strain to electric displacement and stress will be linear as given in eq.(4.7) and (4.8). When the external electric field is applied at a level such that point 'B' goes beyond the switching surface, the switching surface moves towards the loading point 'B' such that the switching surface reaches the fixed loading point, i.e. the fixed value of electric field, asymptotically. As a result, the center of the yield surface 'A' moves to a new position which leads to the evolution of remnant polarisation.

Fig. 4.5(a) shows a similar graphical illustration of the multi-surface modelling approach. Switching surfaces with different radius represent different threshold limits for each switching surface. For illustration purposes, the number of switching surfaces is chosen to be 4.

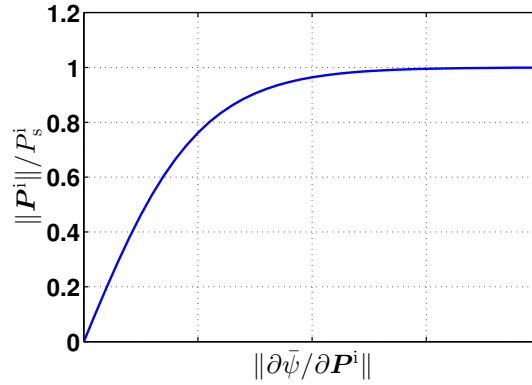


Figure 4.4: Relation between the magnitude of \overline{OA} and the normalised magnitude of polarisation.

Fig. 4.5-4.12 show the multi-switching surface on an electric field and the evolution of the surfaces during the various stages of loading processes. In each of these figures, subfigures (a) represent the switching surfaces and the load point in the domain of the electrical field; subfigures (b) represent the distribution of magnitude in each remnant polarisation along the \mathbf{e}_3 direction, which corresponds to the direction of the external electric field. Subfigures (c) and (d) represent the dielectric hysteresis and butterfly hysteresis for associated loading processes, respectively.

4.2.3.1 Evolution from unpoled to poled states

Fig. 4.5-4.8 represent the process of the ferroelectric material taken from the unpoled to poled state. For an unpoled material, the yield surfaces are held concentric to the origin in the electric field coordinate as shown in Fig. 4.5(a). At this state, each remnant polarisation of the material is zero as shown in Fig. 4.5(b). However, the total polarisation \mathbf{P}_T^i is non-zero due to the contribution of \mathbf{P}_0^i . As the load increases, see Fig. 4.6, the switching surface moves along the loading point and therefore the associated remnant polarisations evolve. Upon unloading, see Fig. 4.7, the switching surfaces ϕ_1 and ϕ_2 move along the loading path and at the same time the switching surfaces ϕ_3 and ϕ_4 remain unmoved. Hence, the magnitude of \mathbf{P}_1^i and \mathbf{P}_2^i has been reduced. From Fig. 4.8, upon loading again, \mathbf{P}_1^i and \mathbf{P}_2^i evolve and result in a hysteresis behaviour due to unipolar loading, which is an observable phenomenon in experiments.

4.2.3.2 Minor hysteresis loop

In a poled material, upon applying a cyclic electric field at a small magnitude, a small dielectric hysteresis loop is observed which is known as minor hysteresis loop. Fig. 4.9 and Fig. 4.10 show the illustration for a minor hysteresis loop under an extreme loading condition along direction \mathbf{e}_3 . During this cyclic loading, only the switching surfaces ϕ_1 and ϕ_2 reach the switching limit and therefore the corresponding remnant polarisations \mathbf{P}_1^i and \mathbf{P}_2^i change between positive and negative values along the direction \mathbf{e}_3 . However,

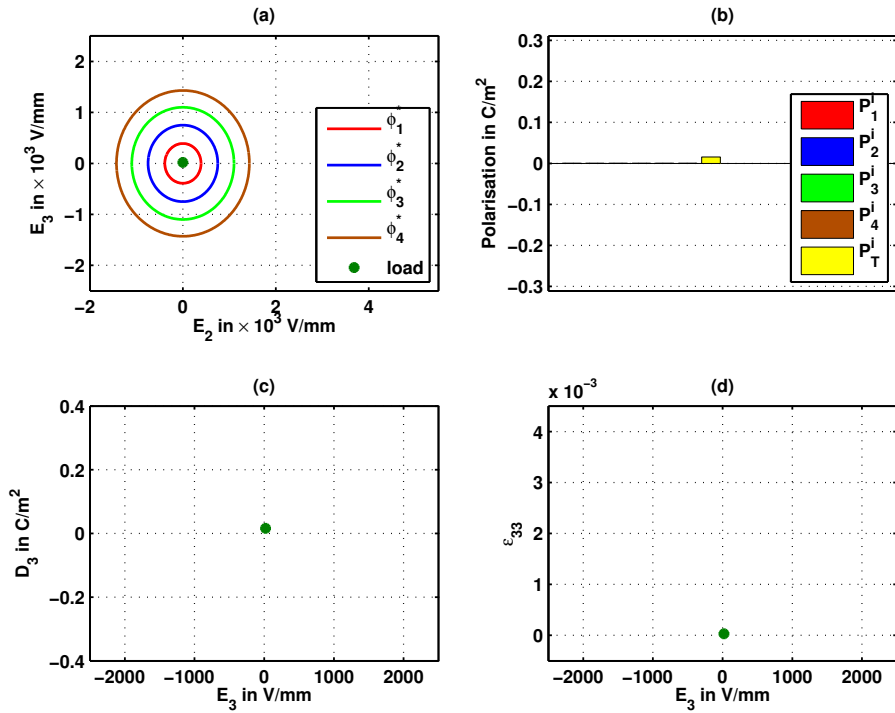


Figure 4.5: Unpoled state of material at load free condition. (a) switching surface, (b) polarisation distribution, (c) dielectric hysteresis and (d) butterfly hysteresis.

the switching limit is not reached by other switching surfaces and therefore there is no change in the remnant polarisation of P_2^i and P_3^i . As a result, the net remnant polarisation remains positive for the whole loading cycle. A relatively small change in remnant polarisation due to this loading gives rise to a small hysteresis loop and therefore the minor hysteresis is observed.

4.2.3.3 Asymmetrical butterfly hysteresis

Fig. 4.11 and 4.12 illustrate an asymmetrical butterfly hysteresis loop for prepoled material and electrical loading along the direction e_3 . During the bipolar cyclic electric field loading with a medium magnitude, the switching surfaces ϕ_1 and ϕ_2 reach their switching limit and therefore the remnant polarisations P_1^i and P_2^i evolve along with cyclic loading. However, the switching limits of surfaces for P_3^i and P_4^i are not reached. Therefore the magnitude of P_3^i and P_4^i do not change. This results in a total remnant polarisation of larger magnitude in the poling direction than in the opposite direction. Due to this unequal magnitude of remnant polarisation between the poling direction and its opposite direction, the butterfly hysteresis loop shows an asymmetrical behaviour.

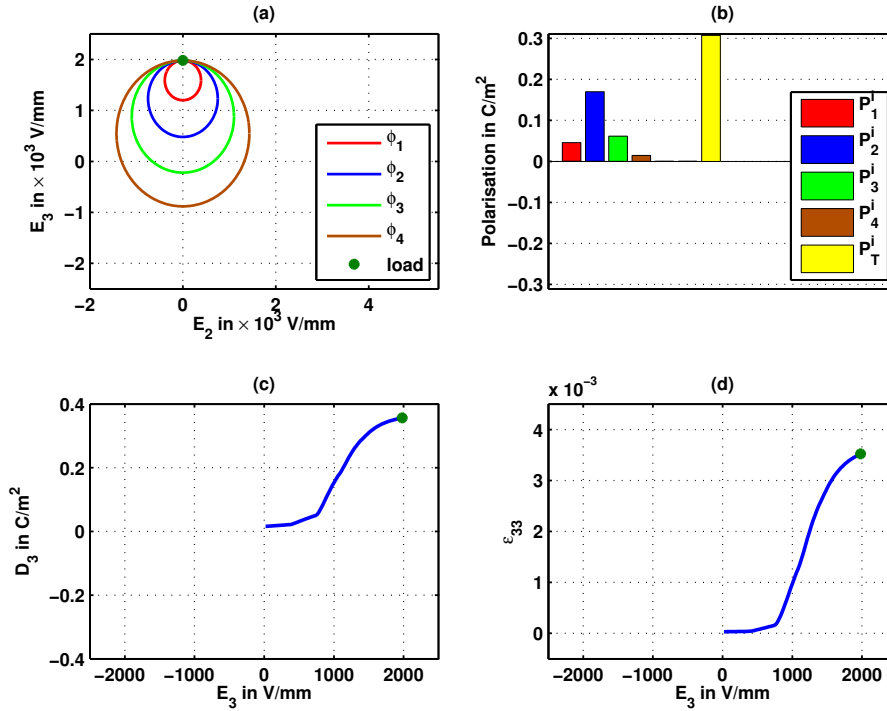


Figure 4.6: Initially unpoled material under an applied electric field. (a) switching surface, (b) polarisation distribution, (c) dielectric hysteresis and (d) butterfly hysteresis.

4.3 Simulation of ferroelectric behaviour

This section discusses the simulation results of ferroelectric behaviour for the proposed model. The algorithmic sketch for the numerical simulation is given in the appendix. In the first part of this section, based on the experimental data, material parameters for the model are identified and the results are compared. In the second part, a qualitative prediction of decaying offset polarisation of electrically fatigued specimen is discussed.

4.3.1 Parameter identification based on experimental data for ferroelectric hysteresis at different loading levels

The simulations studied in this subsection refer to the same loading conditions as the experimental data shown in Fig. 4.1. For an unpoled material, the centers of the yield surfaces are chosen to coincide with the origin in the space of the electric field – in other words, the remnant polarisation vanishes identically. In order to consider the material as a poled specimen, a unipolar electric field of up to 2000 V/mm is applied at 1 Hz within the simulations and the resulting remnant polarisation is considered as the initial remnant polarisation for the subsequent examples. Thereafter, the appropriate amplitude of bipolar electric field is applied. For this analysis, the number of remnant polarisations N is taken to be 4. Material parameters related to the linear piezoelectric

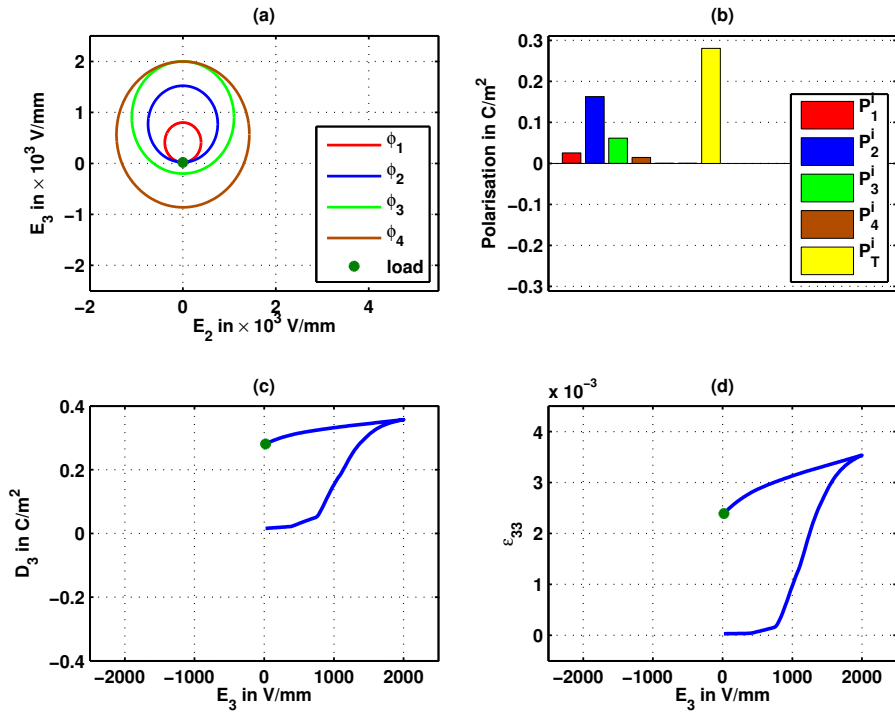


Figure 4.7: Initially unpoled material at a state of reverse loading. (a) switching surface, (b) polarisation distribution, (c) dielectric hysteresis and (d) butterfly hysteresis.

behaviour are taken from the manufacturer datasheet, whereas the parameters for ferroelectric behaviour are obtained from a calibration procedure based on the experimental data shown in Fig. 4.1. Viscosity related parameters are chosen so that quasi rate independent behaviour is obtained. The material parameters for the PZT5A1 material are calibrated based on a least square minimisation approach and are summarised in Tab. 4.1.

Fig. 4.13 shows the comparison of results from experiments and simulations. From these result, both the minor hysteresis and major hysteresis in the experiments are captured very well within the simulation. It is also observed that both offset polarisation as well as asymmetric behaviour is very well captured.

4.3.2 Simulation of decaying offset polarisation of an electrically fatigued specimen

In Lupascu [77], a fatigued specimen is studied under varying amplitudes of electrical loading. By increasing the electrical loading, the specimen is observed to be regaining its symmetric behaviour within the butterfly hysteresis. At the same time, an offset in the dielectric hysteresis for a lower amplitude of electrical loading is observed. Upon continuing the experiment by decreasing the electrical loading, the material response

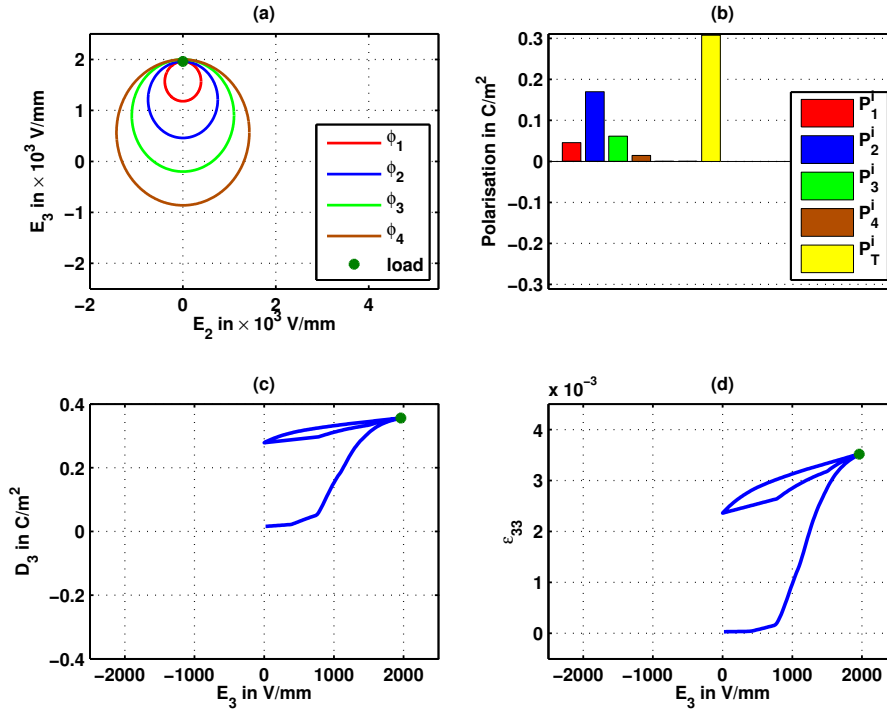


Figure 4.8: Initially unpoled material at the state of reloading. (a) switching surface, (b) polarisation distribution, (c) dielectric hysteresis and (d) butterfly hysteresis.

shows less asymmetry and the offset in the dielectric hysteresis is also reduced. Fig. 4.14 shows the loading path for the numerical simulation.

The experimental results considered are shown in Fig. 4.2. The offset polarisation in the electrically fatigued material is induced due to the fact that the domains are oriented in a particular direction. This phenomenon of fixed domains is similar to phenomena that occur during the poling process. Therefore, this offset polarisation is equivalently replaced by an initial remnant polarisation within the simulations. With this initial condition, the electrical loading with increasing and decreasing maximum amplitude of electrical loading is applied. The simulation results for this loading are shown in Fig. 4.15(a,b). Following this, the amplitude of electrical loading is reduced. The ferroelectric behaviour of this loading path is given in Fig. 4.15(c,d). The results are qualitatively well comparable with the experimental results, in particular the presence of offset in dielectric hysteresis and asymmetry in butterfly hysteresis when increasing the electrical loading and the reduced offset in dielectric hysteresis and asymmetry in butterfly hysteresis during the decreased electrical loading are captured. The reduction in offset upon slowly decreasing the electrical loading level is due to the movement of the yield surface to arrange its center near to the origin. From the simulation results, the multi-surface model on ferroelectrics can be taken as a good start in further developing the constitutive model for ferroelectric materials which undergo electrical fatigue.

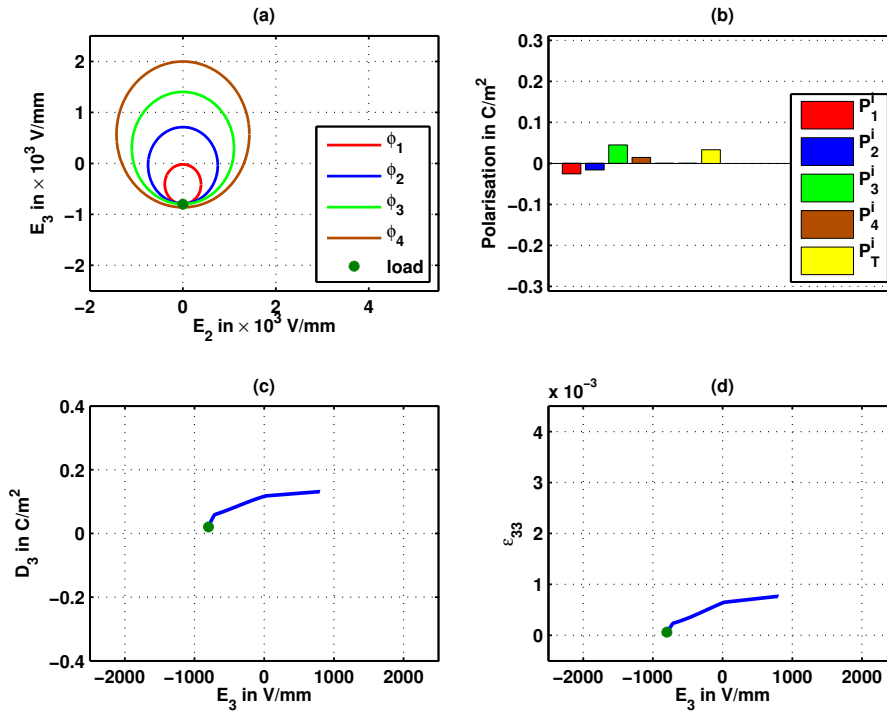


Figure 4.9: Minor loop: loading in opposite direction to the poling direction. (a) switching surface, (b) polarisation distribution, (c) dielectric hysteresis and (d) butterfly hysteresis.

4.3.3 Polarisation rotation test

In this section, the numerical results of polarisation rotation simulations are discussed. To perform this simulation, the initial conditions are assumed such that the specimen is poled and the electric field is applied at an angle to this initial poling direction. The particular angles considered are 0° , 45° , 90° , 135° and 180° . The change in electric displacement and the change in strain, both projected onto the direction of the applied electric field, are calculated and the results are shown in Fig. 4.16. From these simulation results, it is observed that the model is able to capture the material behaviour under multiaxial loading, even though this experimental data is not considered within the parameter identification procedure.

4.4 Summary and conclusion

In this chapter, a multisurface ferroelectric modelling approach is introduced, which is able to capture minor loop as well as asymmetric hysteresis behaviour. In view of the numerical implementations, the model's ability to predict experimental data is shown. It has also been shown that the model could mimic the behaviour of fatigued specimen. Therefore, this modelling approach can be extended to the simulation of fatigue behaviour. From the experimental results, Fig. 4.1, the lowest strain value on

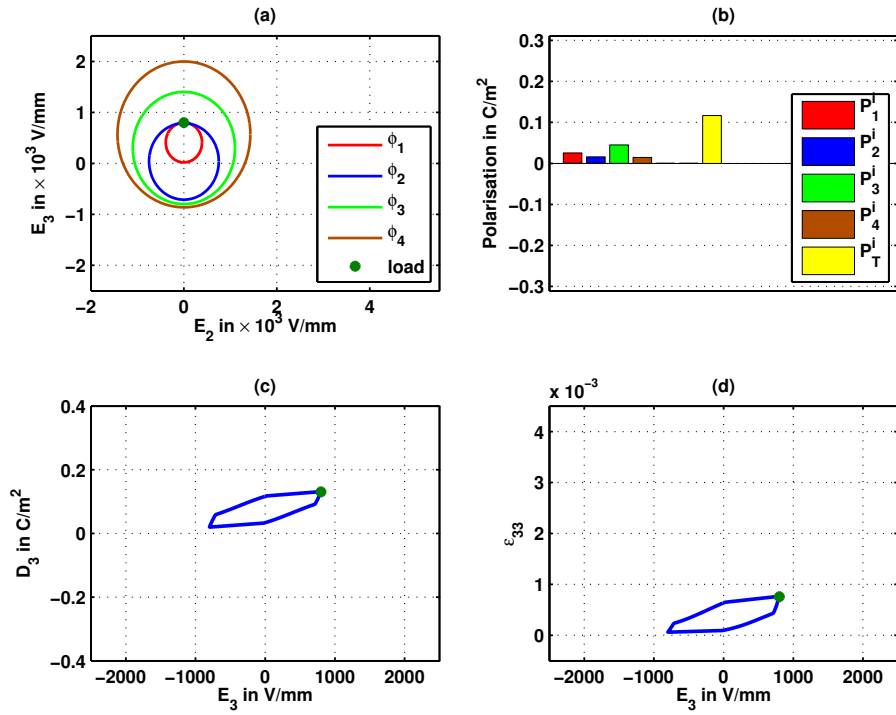


Figure 4.10: Minor loop: reverse loading in the direction of initial poling. (a) switching surface, (b) polarisation distribution, (c) dielectric hysteresis and (d) butterfly hysteresis.

each wing from the butterfly hysteresis curve differ from each other. This difference decreases as the maximum amplitude of electrical loading increases. However, such an effect is not observed in the simulation results. This character can be seen as a result of additional coupling effects along the poling direction. A modification of the coupling part in the energy function can therefore be an improvement to this multi-surface model.

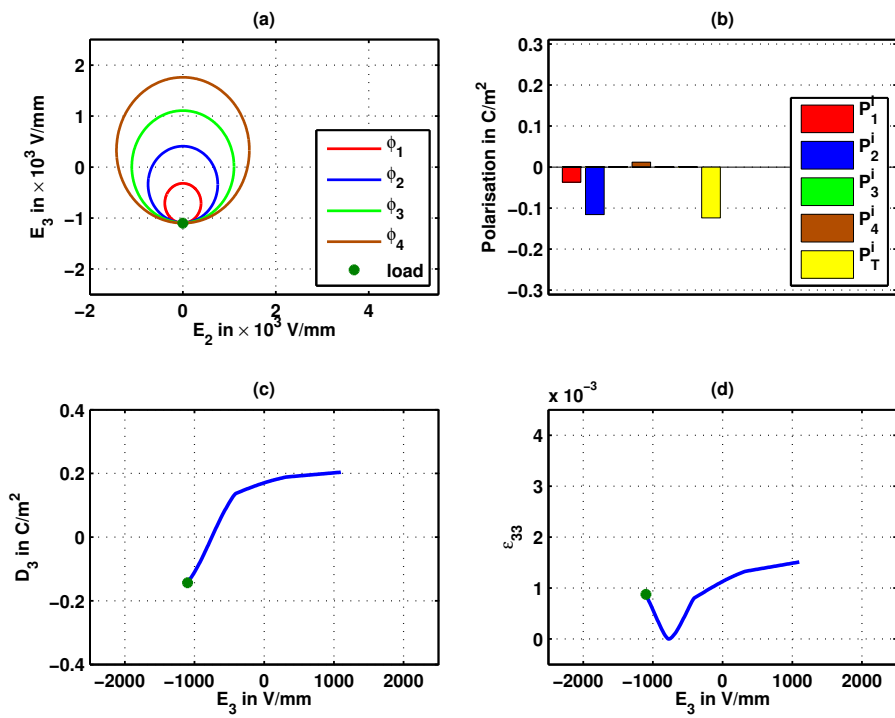


Figure 4.11: Asymmetrical loop: loading in opposite direction to the poling direction. (a) switching surface, (b) polarisation distribution, (c) dielectric hysteresis and (d) butterfly hysteresis.

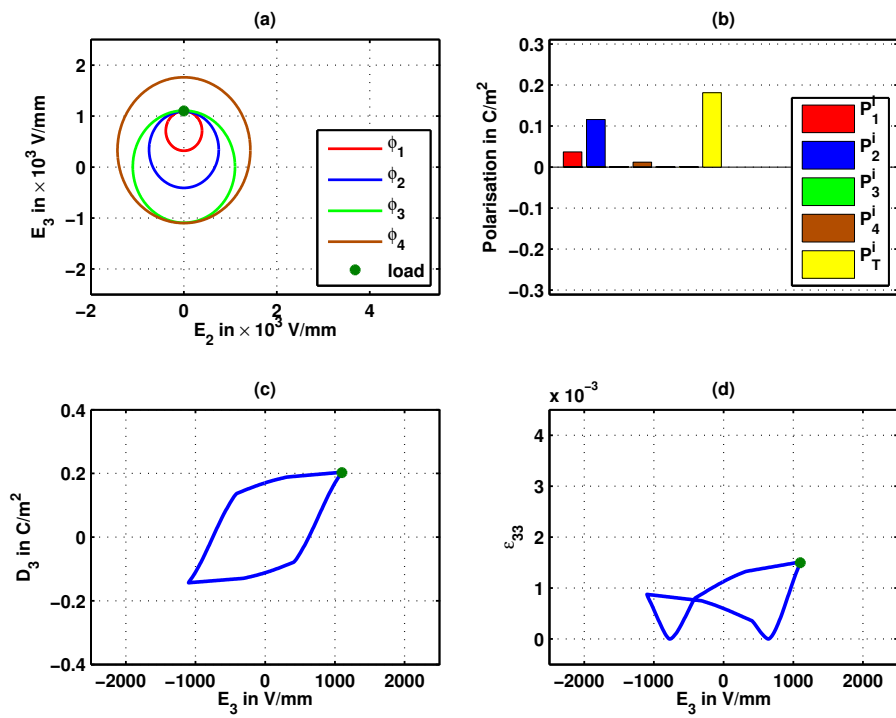


Figure 4.12: Asymmetrical loop: reverse loading in the direction of initial poling. (a) switching surface, (b) polarisation distribution, (c) dielectric hysteresis and (d) butterfly hysteresis.

Table 4.1: Material parameters for the multi-surface model for ferroelectric ceramics.

param.	denomination	unit	value
λ	Lamé parameter	kN/m ²	91.6 $\times 10^6$
μ	Lamé parameter	kN/m ²	18.86 $\times 10^6$
β_1	Piezoelectric coupling parameter	C/m ²	2.7
β_2	Piezoelectric coupling parameter	C/m ²	-10.9
β_3	Piezoelectric coupling parameter	C/m ²	-11
γ	Electric permittivity	C ² /(kN m ²)	-8.11 $\times 10^6$
1E_c	Coercive electric field	kV/m	0.39
2E_c	Coercive electric field	kV/m	0.75
3E_c	Coercive electric field	kV/m	1.1
4E_c	Coercive electric field	kV/m	1.43
P_s^i	Saturation polarisation	C/m ²	0.311 $\times 10^3$
ε_s^i	Saturation strain	-	2.781 $\times 10^{-3}$
a_1	Hardening parameter	C/m ²	0.662
a_2	Hardening parameter	C/m ²	0.415
a_3	Hardening parameter	C/m ²	0.331
a_4	Hardening parameter	C/m ²	0.336
α_1	polarisation factor	-	0.15
α_2	polarisation factor	-	0.56
α_3	polarisation factor	-	0.19
α_4	polarisation factor	-	0.05
P_0^i	constant offset polarisation	C/m ²	$0.05 \times P_s^i e_3$
m_i	Viscosity shape exponent	-	1
η_i	Viscosity shape exponent	m ² /(C s)	6.25 $\times 10^{-2}$

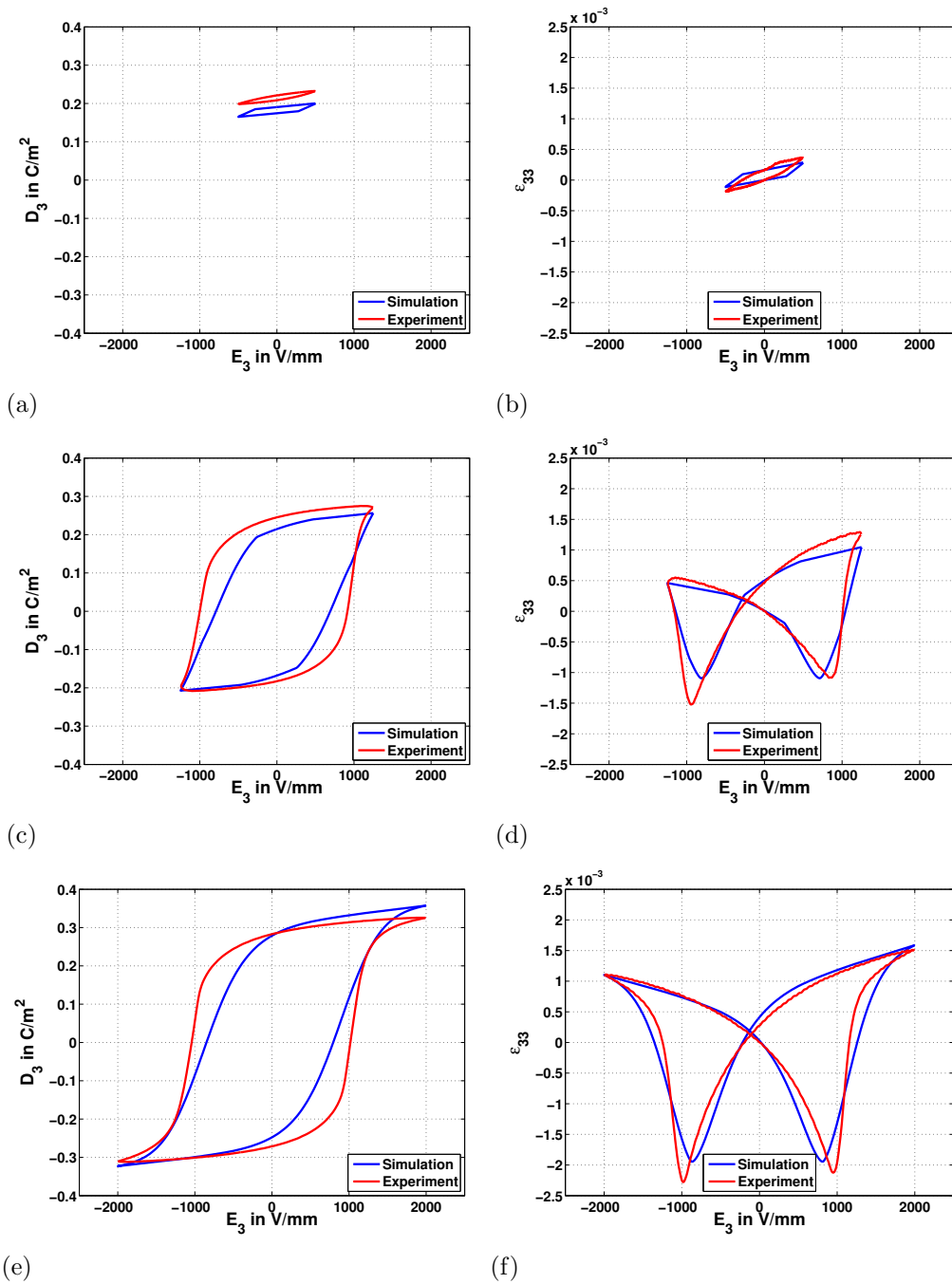


Figure 4.13: Experimental data and simulation results for dielectric hysteresis (a, c, e) and butterfly hysteresis (b, d, f) of PZT5A1 for a linearly increasing and decreasing electric field (triangular shaped cyclic loading) with the amplitude of 500 V/mm, 1250 V/mm and 2000 V/mm.

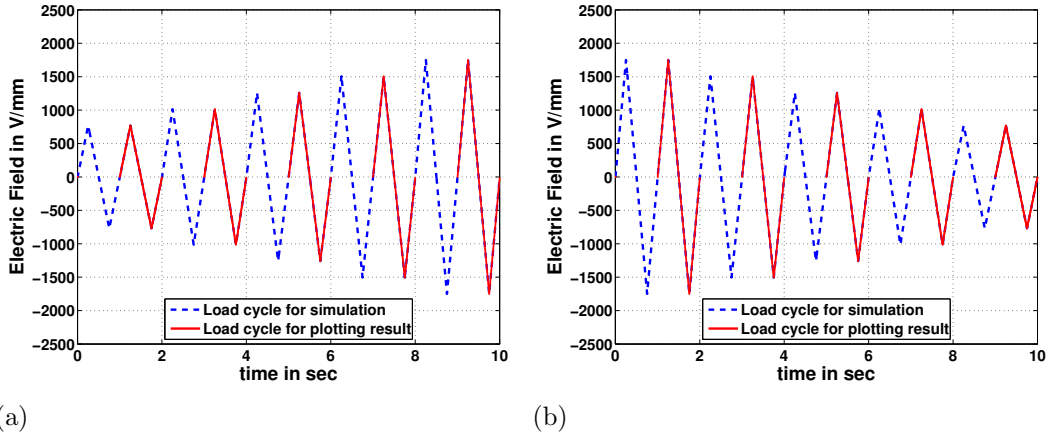


Figure 4.14: Loading curve on the fatigued specimen with (a) increasing and (b) decreasing maximum amplitude of the electric field.

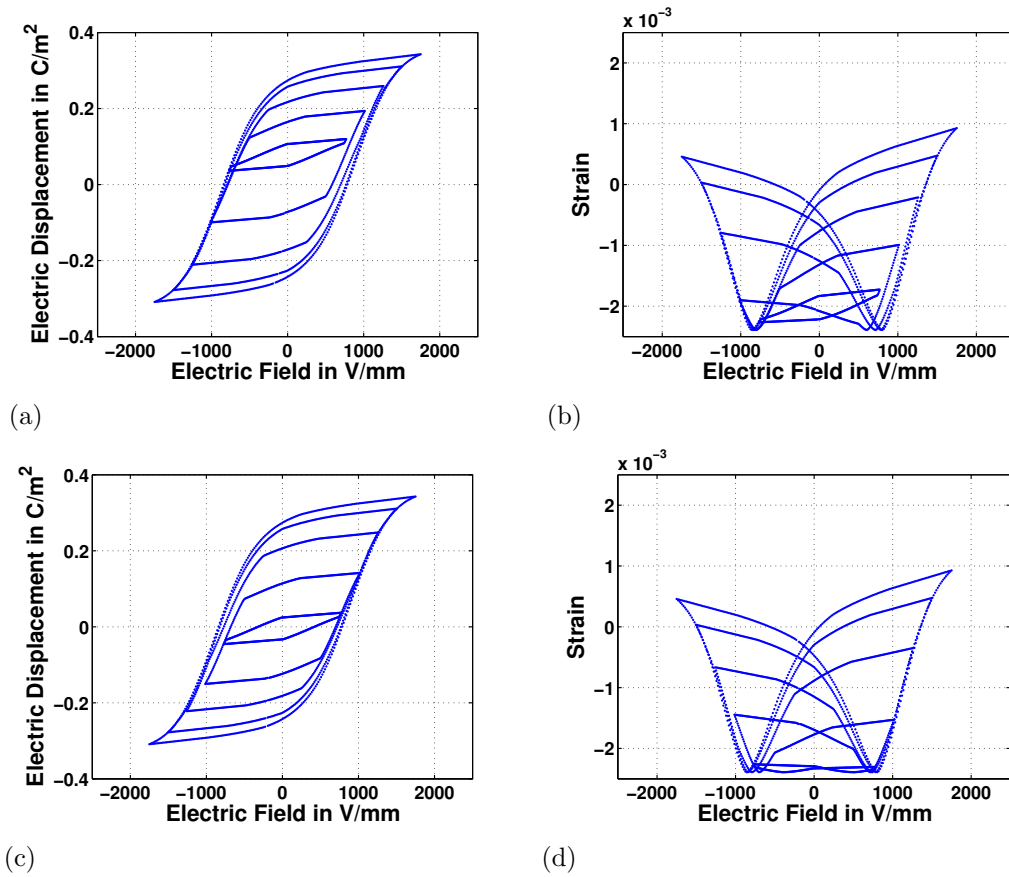


Figure 4.15: Simulation results of ferroelectric hysteresis behaviour on bipolar electrical loading on fatigued specimen with increasing (a, b) and decreasing (c, d) amplitude of maximum applied electric field.

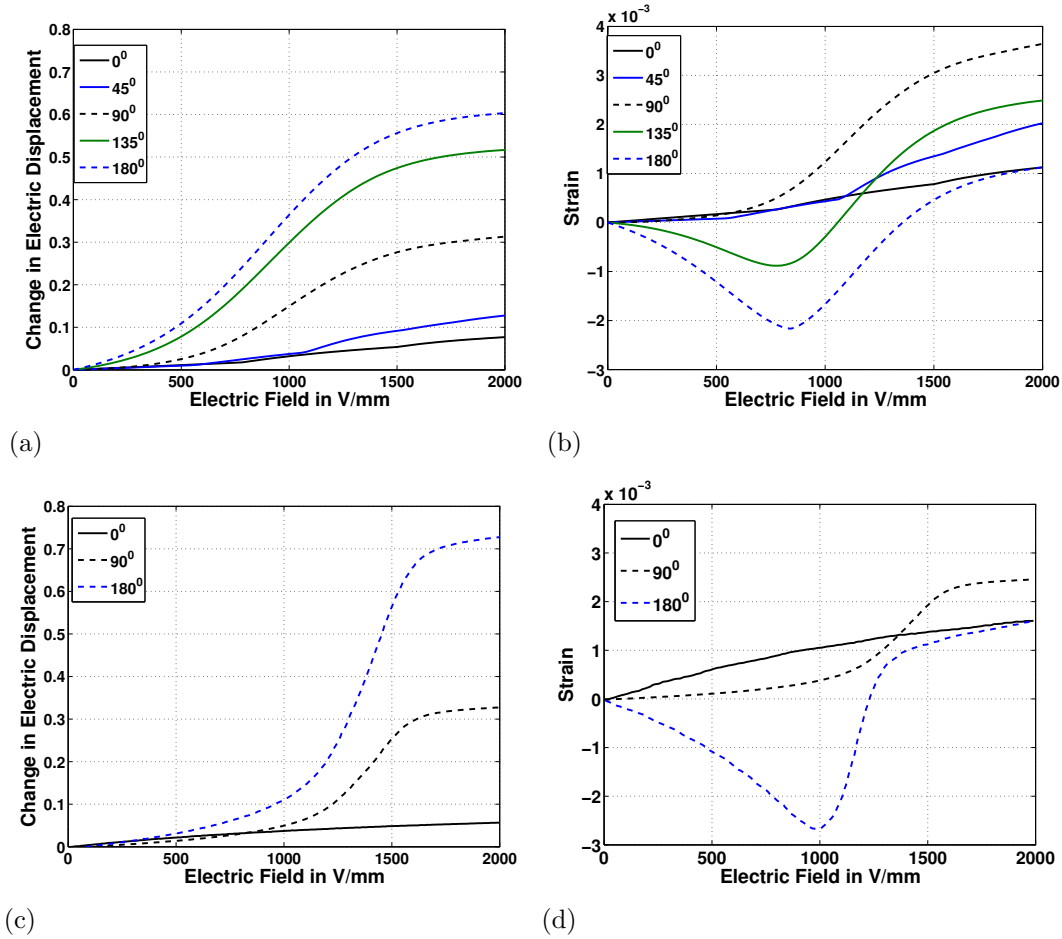


Figure 4.16: Polarization rotation curves: simulation (a, b) and experimental results (c, d), [80], for various loading angles between the direction of polarisation and the direction of electrical loading.

5 An anisotropic switching model including external stress effects

During the application of displacement actuators, the material undergoes a stress load along with the electrical loading. For soft piezoelectric materials, the additional stress load influences the ferroelectric nature of the material. Therefore, with respect to designing an actuator, a constitutive model is important which could capture the effects of stress in ferroelectric behaviour. Keeping this in mind, in this chapter, a ferroelectric constitutive model is developed, which is also able of capturing the ferroelastic behaviour as well as mechanical depolarisation. From the experimental results on multiaxial loading, the pre-poled material shows the anisotropic behaviour in switching condition. To capture this anisotropic behaviour, an elliptical yield function is introduced. This chapter begins with the thermodynamic formulation of the model. In the results section, various properties of the model are presented by means of representative simulation results. To obtain a qualitative comparison with the experimental data, various experimental results will also be given in this section.

5.1 Thermodynamical modelling framework

In order to consider the behaviour of ferroelastic hysteresis along with the ferroelectric hysteresis, an additional internal variable $\boldsymbol{\varepsilon}^i$ along with the remnant polarisation \mathbf{P}^i is introduced as in [65]. With that additional internal variable, a thermodynamical potential as free energy per unit volume, is introduced as

$$\psi = \psi^*(\boldsymbol{\varepsilon}, \boldsymbol{\varepsilon}^i, \mathbf{E}, \mathbf{P}^i) + \bar{\psi}(\boldsymbol{\varepsilon}^i, \mathbf{P}^i)$$

This potential is additively decomposed into the reversible part ψ^* and the irreversible part $\bar{\psi}$. In the ferroelastic hysteresis, the material exert a change in remnant strain without any change in remnant polarisation. Hence, in the consideration of the additively decomposed remnant strain $\boldsymbol{\varepsilon}^i = \boldsymbol{\varepsilon}^{pi} + \boldsymbol{\varepsilon}^{si}$, the first part is treated as the contribution for the irreversible strain due to polarisation, and the second term is treated as the ferroelastic part of the irreversible strain. The first term is derived from the assumed one to one relation between irreversible strain and the irreversible electric field, namely

$$\boldsymbol{\varepsilon}^{pi} = \frac{3}{2} \frac{\varepsilon_s^i}{P_s^i} [\mathbf{P}^i \otimes \mathbf{P}^i] : \mathbf{P}. \quad (5.1)$$

The scalars P_s^i and ϵ_s^i are the saturation remnant polarisation and saturation strain values respectively. To be able to consider the linear piezoelectric behaviour in the reversible regime, the free energy potential is given as

$$\begin{aligned} \psi = & \frac{1}{2} [\boldsymbol{\epsilon} - \boldsymbol{\epsilon}^i] : \mathbf{E} : [\boldsymbol{\epsilon} - \boldsymbol{\epsilon}^i] - \frac{|\mathbf{P}^i|}{P_s^i} \mathbf{E} \cdot \mathbf{e} : [\boldsymbol{\epsilon} - \boldsymbol{\epsilon}^i] \\ & - \frac{1}{2} \mathbf{E} \cdot \boldsymbol{\epsilon} \cdot \mathbf{E} - \mathbf{P}^i \cdot \mathbf{E} + \bar{\psi}(\boldsymbol{\epsilon}^{si}, \mathbf{P}^i). \end{aligned} \quad (5.2)$$

We consider the case of rate-dependent problems so that a class of dissipation functions with reversible admissible range Λ can be governed by the level-set function Φ . This results in the dissipation contribution

$$\mathcal{D} = - \frac{\partial \psi}{\partial \boldsymbol{\epsilon}^{si}} : \dot{\boldsymbol{\epsilon}}^{si} - \frac{\partial \psi}{\partial \mathbf{P}^i} \cdot \dot{\mathbf{P}}^i - \sum_{i=1}^n \frac{1}{\eta_i [m_i + 1]} \langle \Phi_i \rangle^{m_i+1} \geq 0 \quad (5.3)$$

with the constants $\eta_i > 0$ and $m_i > 0$ interpreted as material parameters associated with the viscosity or rather rate-dependency of the electromechanical process [84]. Eq.(5.3) motivates the definition of the work conjugate variables of the internal state variables as

$$\hat{\boldsymbol{\sigma}} = - \frac{\partial \psi}{\partial \boldsymbol{\epsilon}^{si}} = \boldsymbol{\sigma} - \frac{\partial \bar{\psi}}{\partial \boldsymbol{\epsilon}^{si}}, \quad (5.4)$$

$$\hat{\mathbf{E}} = - \frac{\partial \psi}{\partial \mathbf{P}^i} = \mathbf{E} - \frac{\partial \bar{\psi}}{\partial \mathbf{P}^i}. \quad (5.5)$$

With these definitions at hand, rewriting the dissipation function (5.3) yields

$$\mathcal{D} = \hat{\boldsymbol{\sigma}} : \dot{\boldsymbol{\epsilon}}^{si} + \hat{\mathbf{E}} \cdot \dot{\mathbf{P}}^i - \sum_{i=1}^n \frac{1}{\eta_i [m_i + 1]} \langle \Phi_i \rangle^{m_i+1} \geq 0. \quad (5.6)$$

The switching threshold functions Φ_i control the activation of domain switching. In this case the number of the switching threshold function n is assumed to be 2, where the first function Φ_1 shall be referred to ferroelastic switching phenomena and the second one shall be used for the ferroelectric switching and mechanical depolarisation. In the case of reversible processes $\Phi_i < 0$ holds, whereas $\Phi_i \geq 0$ is allowed for irreversible processes.

5.1.1 Ferroelastic switching

The threshold function representing ferroelastic switching is introduced as

$$\Phi_1 = \frac{3 \hat{\boldsymbol{\sigma}} : \mathbf{P} : \hat{\boldsymbol{\sigma}}}{2 h \sigma_c^2} - 1, \quad (5.7)$$

wherein σ_c^2 is the material parameter which represents the coercive value of mechanical stress. In this proposed model, the hardening contribution on ferroelastic deformation is assumed to be isotropic. This hardening is included by introducing parameter h which is given as

$$h = 1 + 2 \operatorname{arctanh} \left(\frac{2 \boldsymbol{\varepsilon}^{\text{si}} : \boldsymbol{\varepsilon}^{\text{si}}}{3 \varepsilon_s^2} \right). \quad (5.8)$$

5.1.2 Ferroelectric switching and mechanical depolarisation

The threshold function representing the evolution of remnant polarisation is introduced as

$$\Phi_2 = \frac{[\mathbf{Q} \cdot \hat{\mathbf{E}}] \cdot [\mathbf{Q} \cdot \hat{\mathbf{E}}]}{E_c^2} + \xi f \frac{\hat{\mathbf{E}}^i \cdot \mathbf{P}^i}{\sigma_c^2 P_s} - 1. \quad (5.9)$$

The first term in this equation represents the ferroelectric switching and the second term represents the mechanical depolarisation. From the experimental investigation on multiaxial loading by Zhou et al. [127], it has been argued that the switching surface changes from circular at unpoled state to elliptical at poled state. To include this shape change of the switching surface, a scaling operator \mathbf{Q} is introduced and given as

$$\mathbf{Q} = \frac{\mathbf{I} - \mathbf{T}}{1 - \mathbf{a} \cdot \mathbf{T} \cdot \mathbf{a}} \quad (5.10)$$

where

$$\mathbf{T} = \frac{k}{P_s^2} [\mathbf{P}^i \otimes \mathbf{P}^i] : \mathbf{P} \quad (5.11)$$

with k being a material parameter associated with a positive scalar value. The scaling operator \mathbf{Q} is introduced such that the scaling factor along the direction \mathbf{a} is 1, i.e. $\mathbf{Q} \cdot \mathbf{a} = \mathbf{a}$. Therefore, during the study of parameter identification, the material parameters for uni-axial loading can be independently identified without multiaxial loading data. The material parameter ξ , as a negative scalar value, is introduced to fit the mechanical depolarisation behaviour. Considering the fact that mechanical depolarisation occurs only in polarised ceramics under a compression stress along the poling direction, the function f , as given in [65], is defined as

$$\begin{aligned} f &= \left[\frac{3}{2} \boldsymbol{\sigma} : \mathbf{P} : \mathbf{M} \right]^2 & \text{if } \boldsymbol{\sigma} : \mathbf{P} : \mathbf{M} < 0 \\ f &= 0 & \text{if } \boldsymbol{\sigma} : \mathbf{P} : \mathbf{M} \geq 0 \end{aligned} \quad (5.12)$$

with $\mathbf{M} = \mathbf{a} \otimes \mathbf{a}$. Eq.(5.12) states that the function f is larger than zero if a state of compressible stresses along the direction \mathbf{a} exists. It is noted that the deviatoric

projection is used in this function to consider the mechanical depolarisation as volume preserving process. The postulate of the maximum dissipation is represented by

$$\mathcal{D} = \sup_{\hat{\boldsymbol{\sigma}}, \hat{\mathbf{E}}} \left\{ \hat{\boldsymbol{\sigma}} : \dot{\boldsymbol{\epsilon}}^{\text{si}} + \hat{\mathbf{E}} \cdot \dot{\mathbf{P}}^{\text{i}} - \frac{1}{\eta_1 [m_1 + 1]} \langle \Phi_1 \rangle^{m_1+1} - \frac{1}{\eta_2 [m_2 + 1]} \langle \Phi_2 \rangle^{m_2+1} \right\}. \quad (5.13)$$

Based on this, the evolution equations for the internal variables are given by

$$\dot{\boldsymbol{\epsilon}}^{\text{si}} = \lambda_1 \frac{\partial \Phi_1}{\partial \hat{\boldsymbol{\sigma}}} = \lambda_1 \frac{3}{h\sigma_c^2} \mathbf{P} : \hat{\boldsymbol{\sigma}} \quad (5.14)$$

$$\dot{\mathbf{P}}^{\text{i}} = \lambda_2 \frac{\partial \Phi_2}{\partial \hat{\mathbf{E}}} = \lambda_2 \frac{2}{E_c^2} [\mathbf{Q}^{\text{t}} \cdot \mathbf{Q} \cdot \hat{\mathbf{E}}] + \lambda_2 \xi f \frac{\mathbf{P}^{\text{i}}}{\sigma_c^2 P_s} \quad (5.15)$$

wherein $\lambda_i = \eta_i^{-1} \langle \Phi_i \rangle^{m_i}$.

5.1.3 Irreversible part of the free energy

Since isotropic hardening is assumed for the ferroelastic contribution, the irreversible part of the free energy $\bar{\psi}$ is introduced as a function of the remnant polarisation. Therefore, the same energy function from the model discussed in chapter 3 is adopted as

$$\bar{\psi} = -a \operatorname{arctanh} \left(\frac{\|\mathbf{P}^{\text{i}}\|}{P_s^{\text{i}}} \right) + \frac{a P_s^{\text{i}}}{2} \ln \left(1 - \frac{\|\mathbf{P}^{\text{i}}\|}{P_s^{\text{i}}} \right). \quad (5.16)$$

5.1.4 Integration algorithm

A numerical simulation of a path dependent material requires a state updating scheme. Accordingly, with a given initial value of \mathbf{P}^{i} and $\boldsymbol{\epsilon}^{\text{si}}$ and for a given electrical $\mathbf{E}(t)$ and mechanical loading $\boldsymbol{\sigma}^{\text{ext}}(t)$, the response of the material is simulated. For numerical integration, the discrete time step is used. In this procedure, starting from an updated state at time step t_n , the current state at time step t_{n+1} is calculated. The algorithm for this procedure is given in Tab. 5.1.

5.2 Numerical results

In the numerical examples, ferroelectric material is simulated under different electromechanical loading to show the ability of the constitutive model to capture various behaviour. Tab. 5.2 provides the material parameters used for this analysis.

Table 5.1: Sketch of the algorithm of the constitutive driver for the rate dependent response of ferroelectric material.

<p>Given: $\boldsymbol{\sigma}_{n+1}^{\text{ext}}, \mathbf{E}_{n+1}, \boldsymbol{\varepsilon}_n, \mathbf{P}_n^i, \boldsymbol{\varepsilon}_n^{\text{si}}$ Set: $\boldsymbol{\varepsilon}_{n+1} = \boldsymbol{\varepsilon}_n, \mathbf{P}_{n+1}^i = \mathbf{P}_n^i, \boldsymbol{\varepsilon}_{n+1}^{\text{si}} = \boldsymbol{\varepsilon}_n^{\text{si}}$ Compute: $\mathbf{R}_l, \mathbf{R}_g$ DOWHILE: $\ \mathbf{R}_g\ \geq \text{tol}_g$ DOWHILE: $\ \mathbf{R}_{l1}\ \geq \text{tol}_{l1}$ or $\ \mathbf{R}_{l2}\ \geq \text{tol}_{l2}$ Compute: $\boldsymbol{\sigma}_{n+1}, \mathbf{D}_{n+1}$ using equations (6.2) and (6.3) $\mathbf{R}_{l1} = \mathbf{P}_{n+1}^i - \mathbf{P}_n^i - \Delta t \lambda_{1\ n+1} \frac{2}{E_c^2} [\mathbf{Q}^t \cdot \mathbf{Q} \cdot \widehat{\mathbf{E}}_{n+1}] + \lambda_{1\ n+1} \xi f \frac{\mathbf{P}_{n+1}^i}{\sigma_c^2 P_s}$ $\mathbf{R}_{l2} = \boldsymbol{\varepsilon}_{n+1}^{\text{si}} - \boldsymbol{\varepsilon}_n^{\text{si}} - \Delta t \lambda_{2\ n+1} \frac{3}{h\sigma_c^2} \mathbf{P} : \boldsymbol{\sigma}_{n+1}$ $\mathbf{P}_{n+1}^i \leftarrow \mathbf{P}_{n+1}^i - \left[\frac{d\mathbf{R}_{l1}}{d\mathbf{P}_{n+1}^i} \right]^{-1} \cdot \mathbf{R}_{l1}$ $\boldsymbol{\varepsilon}_{n+1}^{\text{si}} \leftarrow \boldsymbol{\varepsilon}_{n+1}^{\text{si}} - \left[\frac{d\mathbf{R}_{l2}}{d\boldsymbol{\varepsilon}_{n+1}^{\text{si}}} \right]^{-1} : \mathbf{R}_{l2}$ END $\mathbf{R}_g = \boldsymbol{\sigma}_{n+1}^{\text{ext}} - \boldsymbol{\sigma}_{n+1}$ $\boldsymbol{\varepsilon}_{n+1} \leftarrow \boldsymbol{\varepsilon}_{n+1} - \left[\frac{d\mathbf{R}_g}{d\boldsymbol{\varepsilon}_{n+1}} \right]^{-1} : \mathbf{R}_g$ END END</p>
--

Table 5.2: Material parameters for the rate dependent ferroelectric model.

param.	value	param.	value
λ	70.5×10^6 kN/m ²	γ	-8.11×10^{-6} C ² /kN m ²
μ	14.51×10^6 kN/m ²	P_s^i	0.311×10^3 C/m ²
β_1	2.7 C/m ²	ε_s^i	2.554×10^{-3}
β_2	-10.9 C/m ²	η	6.25×10^{-2}
β_3	-11 C/m ²	m	1
E_c	1 kV/mm	σ_c	50 MPa
ξ	-2.7	a	3.04^{-1} C/m ²
k	0.5		

5.2.1 Purely electrical loading

In this example, and maintaining a stress free condition, only the triangular cyclic electric field is applied. This cyclic electric field begins from 0 kV/mm and cycles between ± 2 kV/mm in the loading frequency of 1 Hz. As initial conditions, an unpoled state of the material has been assumed. Fig. 5.1 shows both dielectric hysteresis and butterfly hysteresis. From the comparison between experimental data and simulation results, it can be seen that the hysteresis behaviour is very well captured. The data also shows the saturation behaviour on remnant strain and remnant polarisation, as observed in the experiments.

5.2.2 Purely mechanical loading

In this section, the simulation of material being subjected to compressive stresses is performed. In this example, the capability of the model to capture the ferroelastic behaviour as well as the mechanical depolarisation behaviour is analysed. To analyse these behaviours, a compressive loading is applied. From the stress free state, the loading is taken to -300 MPa in a rate of -300 MPa/sec. Consequently, it is unloaded to a stress free state again in the same rate of loading. For observing ferroelastic behaviour, the unpoled material state is considered as the initial condition. For the observation of the mechanical depolarisation behaviour, the state of poled material is used. In order to obtain an initially poled material, first an electrical field with the maximum amount of 2 kV/mm is applied at the rate of 8 kV/mm/sec. The remnant polarisation remnant strain values are chosen as initial condition for the subsequent simulation under mechanical loading. Fig. 5.2 shows the change in electrical displacement and strain for the applied compressive stresses. From the qualitative comparison between simulation and experiments, it can be seen that the model reasonably matches the experiments results.

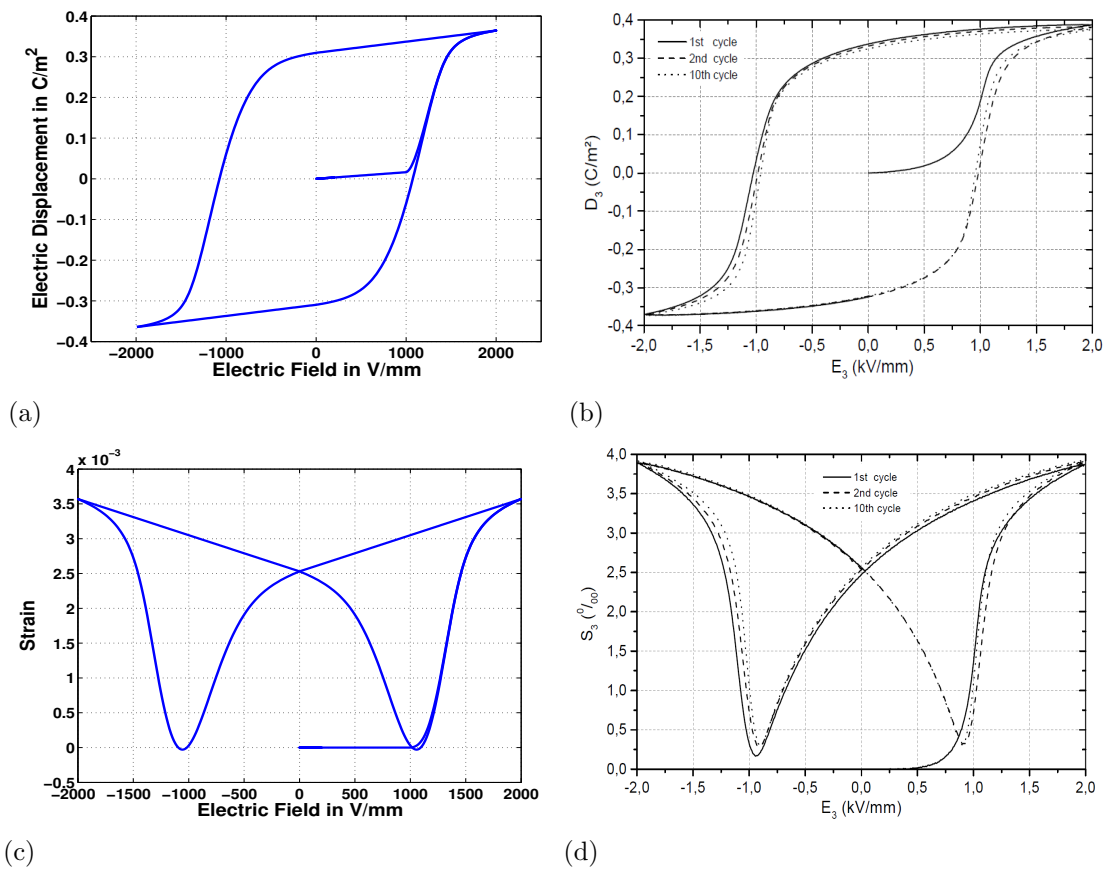


Figure 5.1: Comparison between experiment and simulation of dielectric hysteresis (a,b) and butterfly hysteresis (c,d) [124].

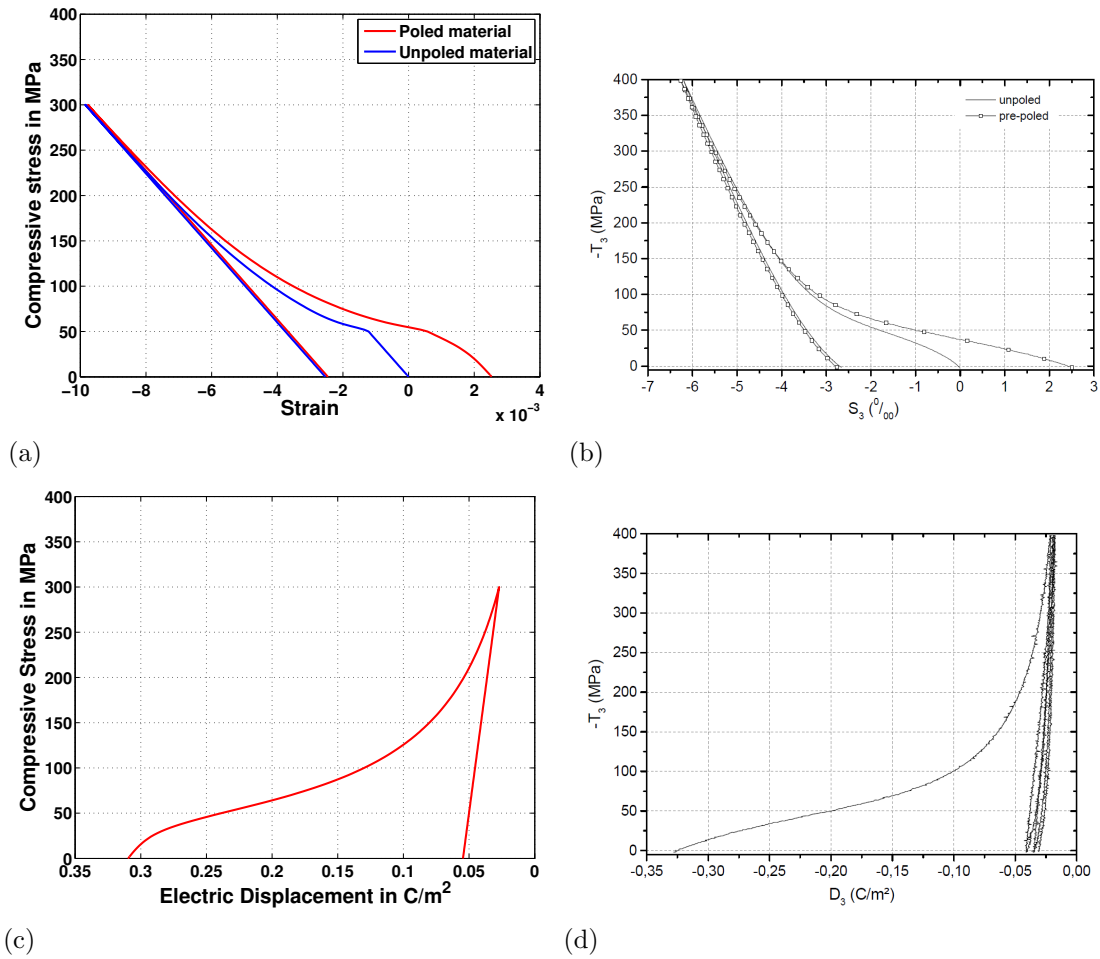


Figure 5.2: Comparison between experiment and simulation of ferroelastic hysteresis (a,b) and mechanical depolarisation (c,d) [124].

5.2.3 Electromechanical loading

In this numerical example, for a simultaneous loading of both electrical field and mechanical stress, the simulation is performed. For a comparison study with experiments, a cyclic electric field under mechanically preloaded loading condition is used. The cyclic electric field between ± 2 kV/mm is applied at 1 Hz. For this example the applied compression stresses are 25 MPa and 50 MPa. Fig. 5.3 shows the comparison between simulation and experiments of the hysteresis loop of ferroelectric ceramics. From the results, it can be observed that the model is able to capture the decrease in remnant polarisation as the compressible stress increases. The experiment also shows that the decrease in the area of hysteresis loop of the butterfly hysteresis for larger compressible stress. This behaviour could also be captured very well within the simulations.

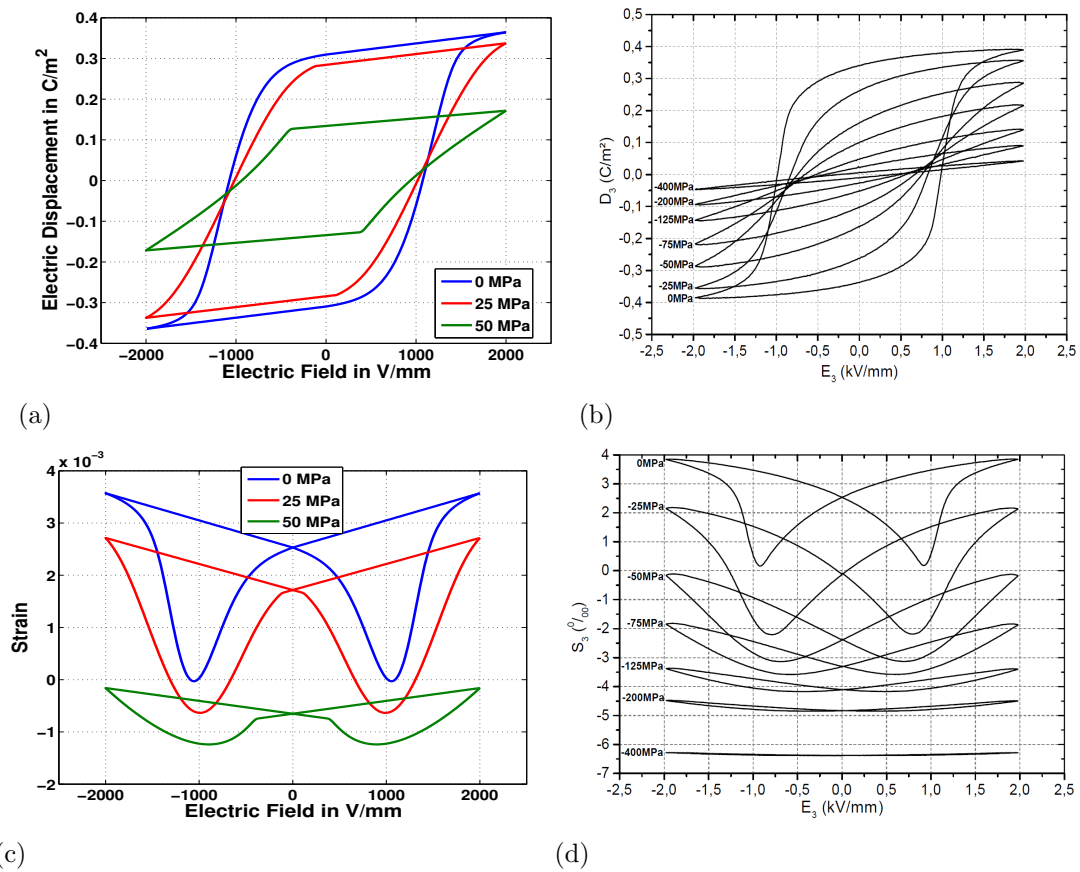


Figure 5.3: Comparison between experiment and simulation of dielectric hysteresis (a,b) and butterfly hysteresis (c,d) under different stress level [124].

5.2.4 Polarisation rotation

An important behaviour in polarisation rotation in the experiment is observed in so far as the material with a poling angle of 135° is observed to have a switching behaviour prior to the material with a poling angle of 180° . In order to simulate this behaviour, an anisotropic switching surface is introduced in this model. From the experimental data, for a pre-poled material, the ferroelectric switching surface is approximated by an elliptically shaped function as shown in Fig. 5.4. For a qualitative comparison, the simulations are performed with the poling angles set to 0° , 45° , 90° , 135° , and 180° . Fig. 5.5 shows the experiment [127] and simulation of the polarisation rotation curve for various angles. In this result, the curve with angle 135° rises prior to the curve with angle 180° as observed in the experiment. The model also captures the increase in the saturation limit of the change in electrical displacement as the poling angle increases.

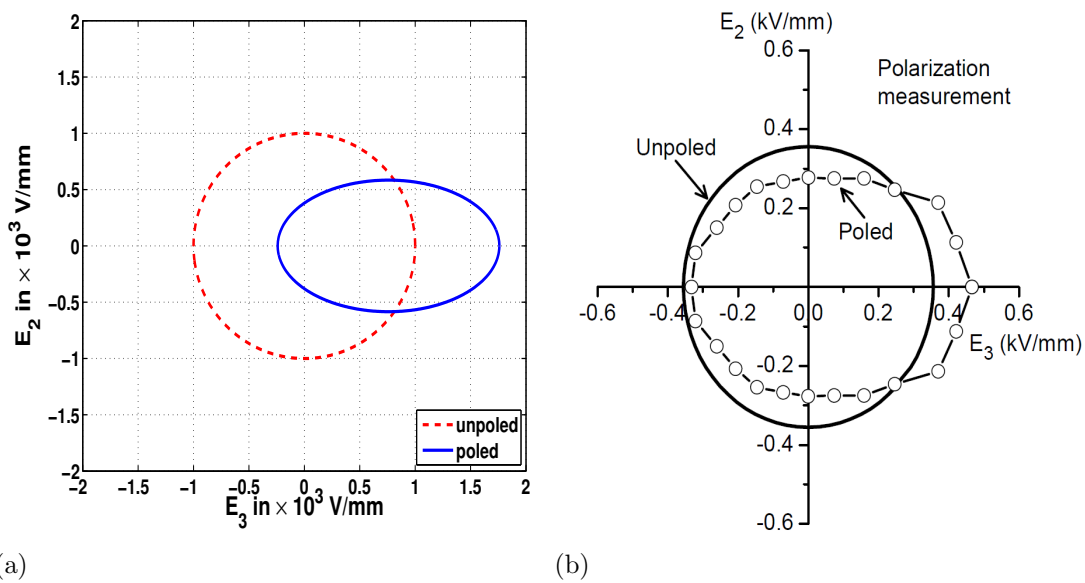
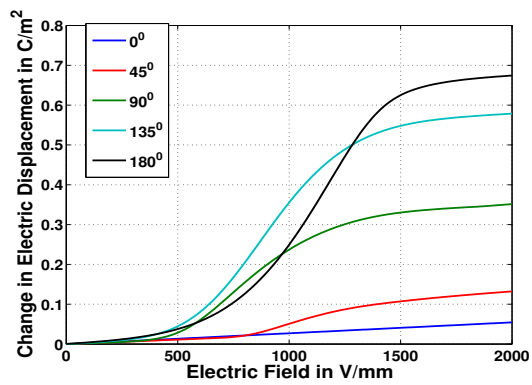


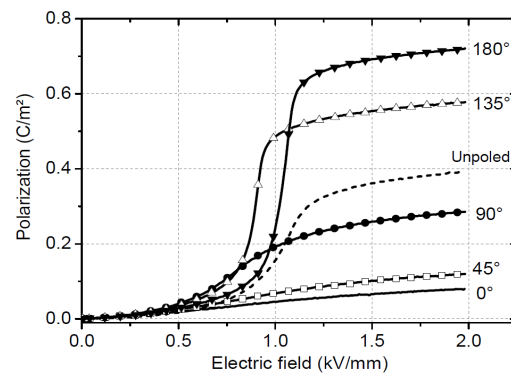
Figure 5.4: Modelling (a) and experimental prediction (b) of ferroelectric switching surface [127].

5.3 Summary and conclusion

In order to predict the influence of switching behaviour due to external stresses, a ferroelectric model is developed in this chapter. In addition, the model is formulated such that it can predict the anisotropic nature of switching functions. From the simulation results, the model is able to predict various behaviours of ferroelectric materials such as ferroelectric hysteresis with and without the external stress, ferroelastic hysteresis, polarisation rotation and mechanical depolarisation. The model is designed so that it can be incorporated into a finite element framework.



(a)



(b)

Figure 5.5: Polarisation rotation by simulation (a) and experimental results (b) [127].

6 A temperature dependent model for ferroelectric ceramics

6.1 Introduction

From the ferroelectric model introduced in chapter 3, it can be understood that the numerical simulation requires two iteration loops, where one is a global iteration and the other one is a local iteration to solve the evolution equation of remnant polarisation. This chapter presents an alternative approach for a rate independent model to the numerical simulation such that the remnant polarisation can be calculated without a local iteration even for a non-linear hardening function. Based on the application, the piezoelectric material may have to work in a different ambient temperature. Due to the heat dissipation behaviour of the material, its temperature could increase. Therefore, in order to account for this variation of material temperature during the applications, temperature dependent piezoelectric and ferroelectric behaviour has to be studied. In this chapter, a temperature dependent ferroelectric model is introduced. As the temperature increases near the Curie temperature, the ferroelectric hysteresis behaviour changes to antiferroelectric hysteresis behaviour. In a poled material, the remnant polarisation of the material decreases to null as the temperature increases above the Curie temperature. This behaviour is called thermal depolarisation. To account for these temperature dependent behaviour, a temperature dependent model is introduced. As a simplification, the heat flux contributions are neglected in this model. In the first part of this chapter, an alternative ferroelectric modelling approach is discussed and finite element simulation results using this approach for an electrical loading on a plate with hole are presented. Following this, the model is modified to capture temperature dependent ferroelectric behaviours such as thermal depolarisation as well as the transition from ferroelectric hysteresis to antiferroelectric hysteresis.

6.2 Constitutive model

This section discusses the electromechanical rate independent constitutive relation of ferroelectric materials. As this model is a modification of the model introduced in chapter 3, the energy terms and the flux terms are adopted from the same model. For the evolution of internal variables, the alternative approach has been discussed. The proof for this approach to satisfy the dissipation inequality is also provided in this section.

6.2.1 Energy and flux terms

The free energy potential as introduced in chapter 3 is restated as,

$$\begin{aligned} \psi = & \frac{1}{2} [\boldsymbol{\varepsilon} - \boldsymbol{\varepsilon}^i] : \mathbf{E} : [\boldsymbol{\varepsilon} - \boldsymbol{\varepsilon}^i] - \frac{\|\mathbf{P}^i\|}{P_s^i} \mathbf{E} \cdot \mathbf{e} : [\boldsymbol{\varepsilon} - \boldsymbol{\varepsilon}^i] \\ & - \frac{1}{2} \mathbf{E} \cdot \boldsymbol{\varepsilon} \cdot \mathbf{E} - \mathbf{P}^i \cdot \mathbf{E} + \bar{\psi}(\mathbf{P}^i). \end{aligned} \quad (6.1)$$

From this energy potential, the stresses and the electric displacement are derived as

$$\boldsymbol{\sigma} = \frac{\partial \psi}{\partial \boldsymbol{\varepsilon}} = \mathbf{E} : [\boldsymbol{\varepsilon} - \boldsymbol{\varepsilon}^i] - \frac{\|\mathbf{P}^i\|}{P_s^i} \mathbf{E} \cdot \mathbf{e}, \quad (6.2)$$

$$-\mathbf{D} = \frac{\partial \psi}{\partial \mathbf{E}} = -\frac{\|\mathbf{P}^i\|}{P_s^i} \mathbf{e} : [\boldsymbol{\varepsilon} - \boldsymbol{\varepsilon}^i] - \boldsymbol{\varepsilon} \cdot \mathbf{E} - \mathbf{P}^i. \quad (6.3)$$

6.2.2 Evolution of internal variable

For the evolution of the internal variable \mathbf{P}^i , the rate of change of internal variables has to be evaluated such that it has to satisfy the inequality constraints obtained from the switching function and the dissipation inequality. In this model, the switching function is chosen to be,

$$\Phi = \|\widehat{\mathbf{E}}\| - E_c \quad (6.4)$$

where

$$\widehat{\mathbf{E}} = \mathbf{E} - \frac{\partial \bar{\psi}}{\partial \mathbf{P}^i}. \quad (6.5)$$

At this stage, a new quantity is introduced which is defined as

$$\mathbf{G} := \frac{\partial \bar{\psi}}{\partial \mathbf{P}^i}. \quad (6.6)$$

Similar to rate independent plasticity-type theory, the switching criteria for this model is expressed as $\Phi \leq 0$. In order to identify whether the state of the system satisfies the switching criteria at a discrete time step t_{n+1} , for known state values at t_n , the following procedure is used. By assuming $\mathbf{P}_{n+1}^i = \mathbf{P}_n^i$, a trial switching function Φ_{trial} is calculated. If the trial switching function satisfies the switching criteria, the value of \mathbf{P}^i remains unchanged. Otherwise, the remnant polarisation \mathbf{P}^i has to be evaluated such as to satisfy the switching criteria. The function Φ_{trial} can be written as,

$$\Phi_{trial} = \left\| \mathbf{E}_{n+1} - \frac{\partial \bar{\psi}}{\partial \mathbf{P}_n^i} \right\| - E_c = \|\mathbf{E}_{n+1} - \mathbf{G}_n\| - E_c. \quad (6.7)$$

If the value of Φ_{trial} is greater than 0, then the internal variables must be updated such that Φ is equal to 0, i.e.

$$\Phi = \|\mathbf{E}_{n+1} - \mathbf{G}_{n+1}\| - E_c = \|\mathbf{E}_{n+1} - \mathbf{G}_n - \Delta\mathbf{G}\| - E_c = 0. \quad (6.8)$$

From the triangular inequality, eq.(6.8) can be reduced to the following equation

$$|\|\mathbf{E}_{n+1} - \mathbf{G}_n\| - \|\Delta\mathbf{G}\|| - E_c \leq 0. \quad (6.9)$$

Reducing the outer modulus of eq.(6.9) results in the following relation

$$\pm [|\|\mathbf{E}_{n+1} - \mathbf{G}_n\| - \|\Delta\mathbf{G}\||] - E_c \leq 0. \quad (6.10)$$

From eq.(6.10), the possible range of $\|\Delta\mathbf{G}\|$ can be derived such as to satisfy the condition $\Phi = 0$. This range is given as

$$\Phi_{trial} = \|\mathbf{E}_{n+1} - \mathbf{G}_n\| - E_c \leq \|\Delta\mathbf{G}\| \leq \|\mathbf{E}_{n+1} - \mathbf{G}_n\| + E_c \quad (6.11)$$

In the present method, the value of $\|\Delta\mathbf{G}\|$ is chosen to be minimum, i.e. $\|\Delta\mathbf{G}\| = \Phi_{trial}$. The following section discusses the necessary condition for this method to satisfy the dissipation inequality.

6.2.3 Dissipation inequality

For a rate independent problem, the dissipation rate inequality condition on the evolution of internal variable is given as

$$\mathcal{D} = \widehat{\mathbf{E}} \cdot \dot{\mathbf{P}}^i \geq 0. \quad (6.12)$$

For a discrete time step, this dissipation function can be rewritten as

$$\mathcal{D} = [\mathbf{E}_{n+1} - \mathbf{G}_n - \Delta\mathbf{G}] \cdot [\mathbf{P}_{n+1}^i - \mathbf{P}_n^i]. \quad (6.13)$$

If $\|\Delta\mathbf{G}\|$ is chosen such that $\|\Delta\mathbf{G}\| = \|\mathbf{E}_{n+1} - \mathbf{G}_n\| - E_c$, then the directions of $\Delta\mathbf{G}$ and $\mathbf{E}_{n+1} - \mathbf{G}_n$ should be identical. As a result, the direction of $\widehat{\mathbf{E}}$ will also coincide with the direction of $\Delta\mathbf{G}$. Hence, $\widehat{\mathbf{E}}$ can be written as $\beta\Delta\mathbf{G}$, where β is a positive scalar value. Therefore the dissipation inequality can be written as

$$\mathcal{D} = \beta\Delta\mathbf{G} \cdot [\mathbf{P}_{n+1}^i - \mathbf{P}_n^i] = \beta[\mathbf{G}_{n+1} - \mathbf{G}_n] \cdot [\mathbf{P}_{n+1}^i - \mathbf{P}_n^i]. \quad (6.14)$$

From the definition of \mathbf{G} given in eq.(6.6), the relation between the remnant polarisation \mathbf{P}^i and \mathbf{G} is given as

$$\mathbf{P}^i = K(\|\mathbf{G}\|) \frac{\mathbf{G}}{\|\mathbf{G}\|} = \nu \frac{\mathbf{G}}{\|\mathbf{G}\|} = \mu\mathbf{G}, \quad (6.15)$$

where K is a scalar valued function and $\nu = K$ as well as $\mu = K/\|\mathbf{G}\|$. From this relation, the change in remnant polarisation can be written as,

$$\mathbf{P}_{n+1}^i - \mathbf{P}_n^i = \mu_{n+1}\mathbf{G}_{n+1} - \mu_n\mathbf{G}_n. \quad (6.16)$$

By substituting this relation, the dissipation function given in eq.(6.14) can be rewritten as

$$\begin{aligned} \mathcal{D} &= \beta [\mathbf{G}_{n+1} - \mathbf{G}_n] \cdot [\mu_{n+1}\mathbf{G}_{n+1} - \mu_n\mathbf{G}_n] \\ &= \beta [\mu_{n+1}\|\mathbf{G}_{n+1}\|^2 + \mu_n\|\mathbf{G}_n\|^2 - [\mu_{n+1} + \mu_n]\mathbf{G}_{n+1} \cdot \mathbf{G}_n] \geq 0. \end{aligned} \quad (6.17)$$

From the Cauchy-Schwarz inequality condition, given as $-\mathbf{G}_{n+1} \cdot \mathbf{G}_n \geq -\|\mathbf{G}_{n+1}\|\|\mathbf{G}_n\|$, this dissipation function can be transformed as

$$\mathcal{D} \geq \beta [\mu_{n+1}\|\mathbf{G}_{n+1}\|^2 + \mu_n\|\mathbf{G}_n\|^2 - [\mu_{n+1} + \mu_n]\|\mathbf{G}_{n+1}\|\|\mathbf{G}_n\|] \geq 0. \quad (6.18)$$

By rearranging this equation, one can obtain the dissipation function as

$$\mathcal{D} \geq \beta [\mu_{n+1}\|\mathbf{G}_{n+1}\| - \mu_n\|\mathbf{G}_n\|] [\|\mathbf{G}_{n+1}\| - \|\mathbf{G}_n\|] \quad (6.19)$$

$$= \beta [\nu_{n+1} - \nu_n] [\|\mathbf{G}_{n+1}\| - \|\mathbf{G}_n\|] \geq 0. \quad (6.20)$$

To satisfy the dissipation inequality condition given in Eq.(6.21), the sign of $\nu_{n+1} - \nu_n$ and $\|\mathbf{G}_{n+1}\| - \|\mathbf{G}_n\|$ has to be identical. This can be obtained by choosing the scalar function K so as to satisfy the following condition.

$$\frac{\partial K}{\partial \|\mathbf{G}\|} \geq 0. \quad (6.21)$$

To evaluate the remnant polarisation, the algorithmic procedure using the discussed method is summarised as

$$\mathbf{G}_{n+1} = \mathbf{G}_n + 0.5 [\Phi_{trial} + |\Phi_{trial}|] \frac{\mathbf{E}_{n+1} - \mathbf{G}_n}{\|\mathbf{E}_{n+1} - \mathbf{G}_n\|}, \quad (6.22)$$

$$\mathbf{P}_{n+1}^i = K(\|\mathbf{G}_{n+1}\|) \frac{\mathbf{G}_{n+1}}{\|\mathbf{G}_{n+1}\|}. \quad (6.23)$$

6.3 Numerical simulation of ferroelectric behaviour

To model the ferroelectric behaviour, an appropriate hardening function is introduced in this section. With this function, the model is implemented in a finite element framework to solve an inhomogeneous boundary value problem.

6.3.1 Hardening function

To obtain a saturation ferroelectric behaviour, the hardening function is chosen as an asymptotic function which approaches the saturation polarisation value as the value of $\|\mathbf{G}\|$ increases. The following function is chosen to obtain such a saturation behaviour

$$K = P_s \tanh\left(\frac{\|\mathbf{G}\|}{a}\right) \quad (6.24)$$

where the scalar value a is a hardening parameter as used in the model discussed in chapter 3.

6.3.2 Results

To predict ferroelectric behaviour by the model proposed, loading under a cyclic electric field is simulated with a maximum loading amplitude of ± 2000 V/mm. The material parameters for this model correspond to those used in chapter 3. For the applied electric field, the obtained results of the simulation of ferroelectric behaviour are highlighted in Fig. 6.1. From these results, it could be observed that the non-linear hardening as well as the saturation effect of remnant polarisation are very well captured by the model without a local iteration procedure.

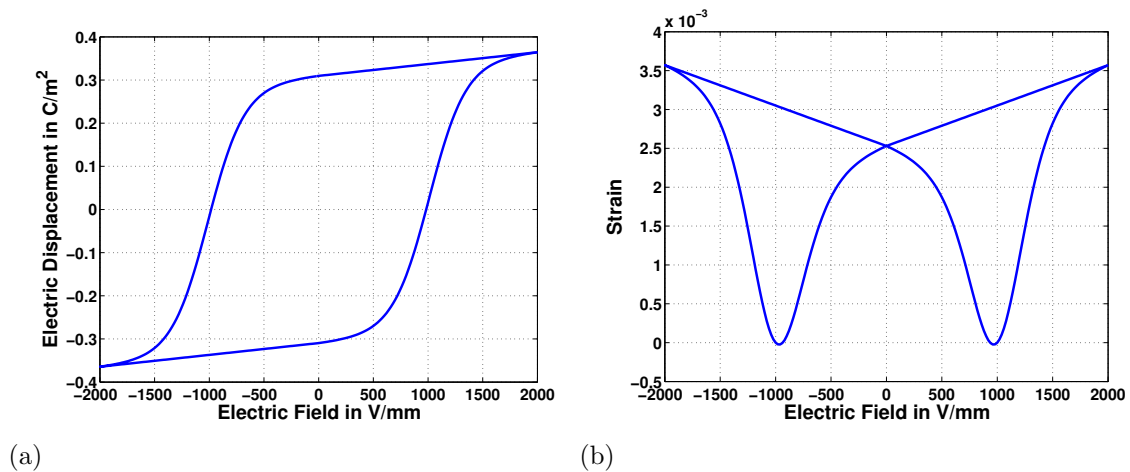


Figure 6.1: Rate independent ferroelectric behaviour.

This framework is extended to a finite element formulation in order to solve an inhomogeneous boundary value problem. As a boundary value problem, an externally applied electric field on a plate with a hole is considered. Using symmetry properties, one quadrant of the plate is considered. The electrical and mechanical boundary conditions for this problem along with the dimensions are given in Fig. 6.2.

The problem is solved by using a three-dimensional finite element formulation. The general finite element framework for electromechanical problems is summarised in ap-

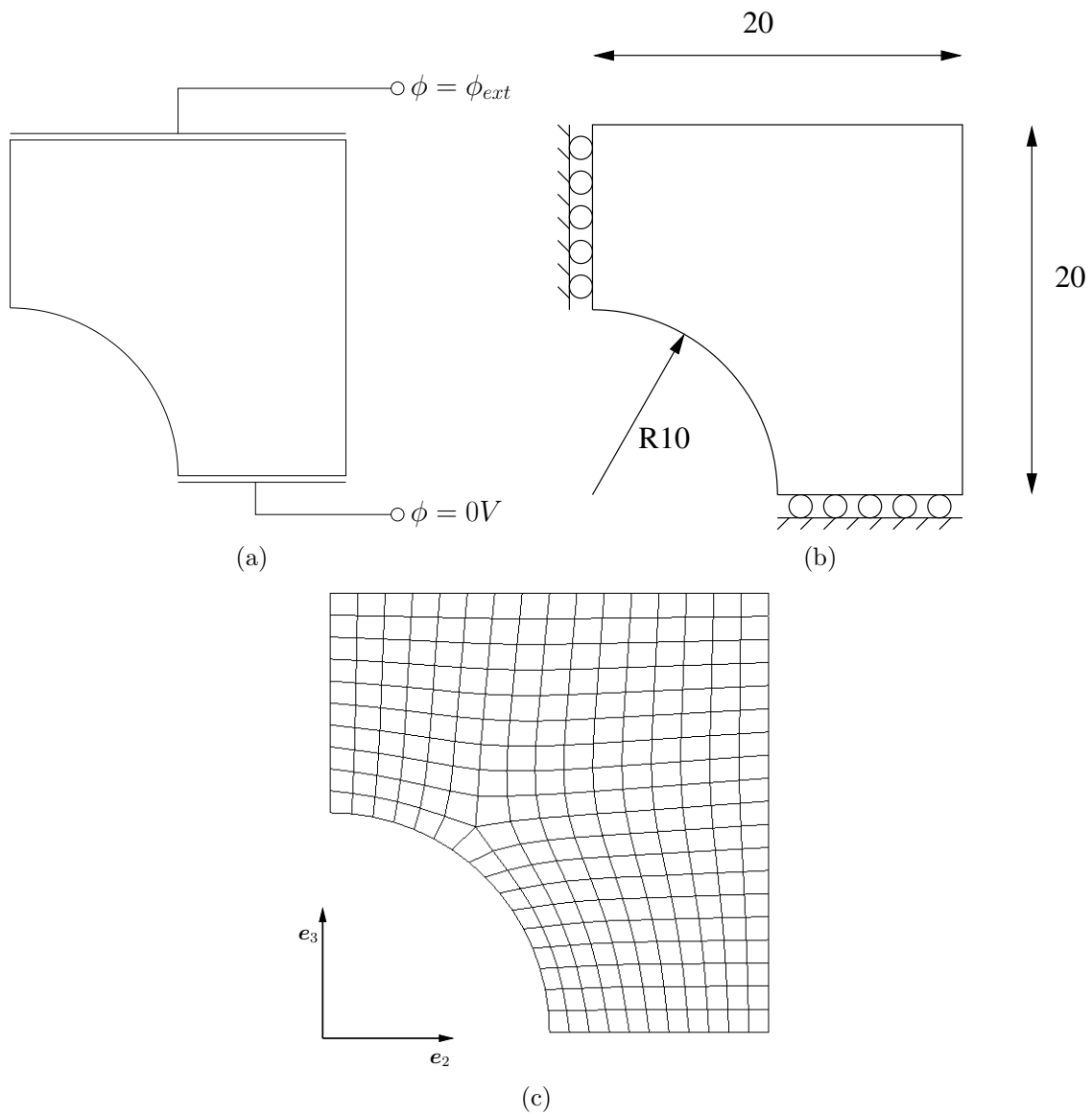
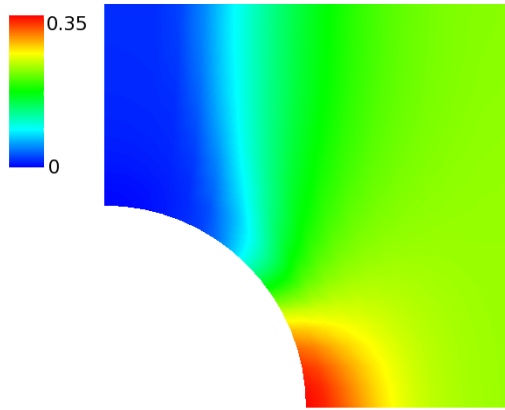
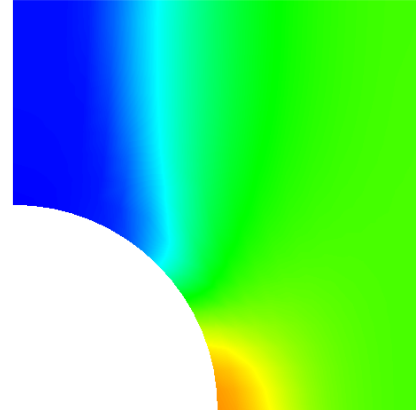
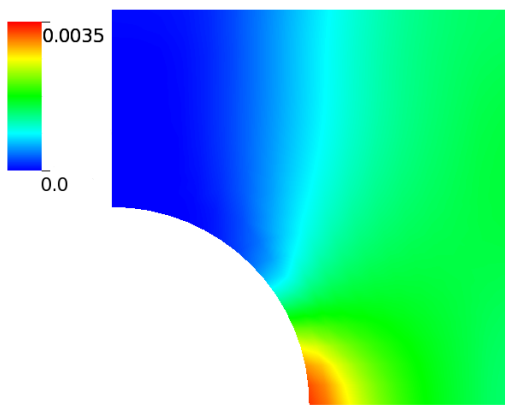
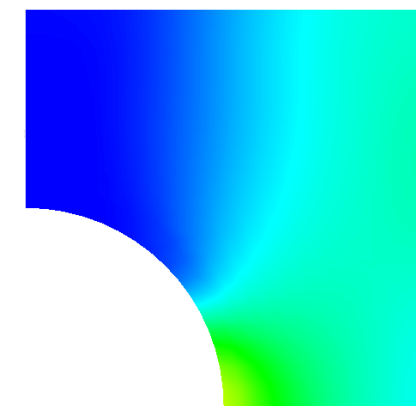
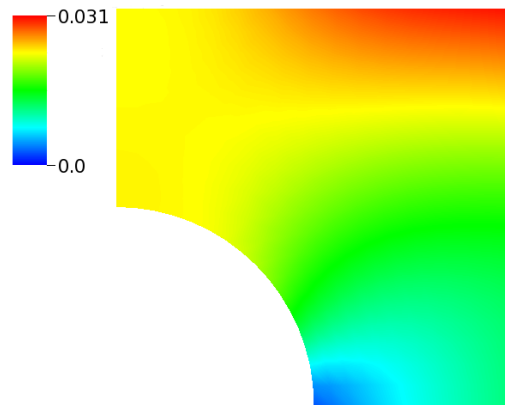
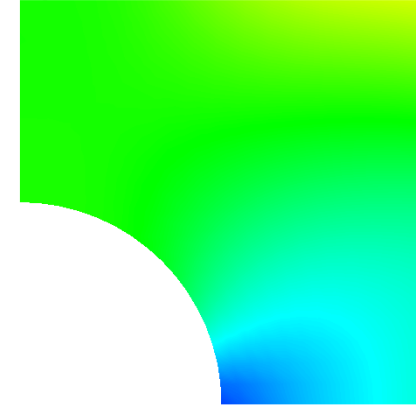


Figure 6.2: Boundary conditions for a plate with hole: (a) electrical boundary condition (b) mechanical boundary condition with dimensions in mm and finite element mesh for a plate with hole (c).

pendix A. Tetragonal elements are used for the analysis. The finite element mesh for this problem is given in Fig. 6.2 (c). The external electrical voltage ϕ_{ext} is applied as follows. From the zero voltage, ϕ_{ext} is increased up to $30kV$. The voltage is then dropped to zero. Simulation results are given in Fig. 6.3.

(a) Electric displacement D_3 in C/m(b) Electric displacement D_3 in C/m(c) Strain ϵ_{33} (d) Strain ϵ_{33} (e) Displacement along e_3 in mm(f) Displacement along e_3 in mm**Figure 6.3:** Simulation of a plate with hole: (a,c,e) results under loading, (b,d,f) results after unloading.

6.4 Temperature dependent ferroelectric model

To obtain the temperature dependent hardening behaviour, two modifications are included in the introduced model. From the study of [78], the coercive electric field decreases as the temperature increases. To represent this effect, the coercive electric field value is given as a function of temperature as

$$E_c = [1 - C] E_c^0 \quad (6.25)$$

with

$$C = \left\langle \frac{\theta - 300}{\theta_c - 300} \right\rangle \quad (6.26)$$

where θ is the temperature of the material and where θ_c is the Curie temperature of the material. The scalar function C is chosen such that the coercive electric field approaches to zero as the temperature reaches the Curie temperature. Such a function is required in order to capture the thermal depolarisation.

6.4.1 Hardening function

As the temperature increases close to the Curie temperature, the behaviour of the material changes from ferroelectric to anti-ferroelectric hysteresis behaviour. To include this effect, the following hardening function is chosen,

$$K = P_s \tanh \left(\frac{\|\mathbf{G}\|}{a} - C \right) - P_s \tanh \left(\frac{-\|\mathbf{G}\|}{a} - C \right). \quad (6.27)$$

At a lower temperature, the value of C will be zero and recaptures the ferroelectric effect. As the temperature rises, the value of C increases along with it. Thus, it influences the hardening function to obtain the anti-ferroelectric behaviour.

6.4.2 Numerical simulation of thermal depolarisation

Thermal depolarisation is a phenomenon which occurs in a poled material. Therefore, for a numerical simulation, the initial condition has to be taken as a poled. This initial condition is obtained by applying an applied electric field upto 2 kV/mm at a temperature of $\theta = 300$ K. The Curie temperature of the material is assumed to be $\theta_c = 400$ K. For simulating the thermal depolarisation, the temperature variable is increased from 300 K to 400 K. The results obtained of temperature depolarisation are presented in Fig. 6.4. The result shows the decrease in electric displacement of the poled material which approaches zero as the temperature increases up to the Curie temperature. Thus, the obtained result matches the experimental data of mechanical depolarisation behaviour as shown in Fig 1.9.

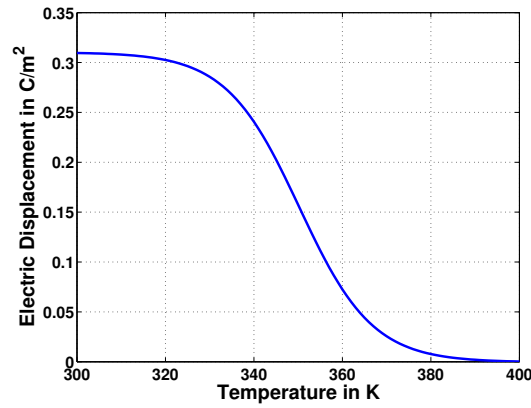


Figure 6.4: Simulation result of thermal depolarisation.

6.4.3 Simulation of ferroelectric hysteresis

To simulate the ferroelectric behaviour for various temperature, the response at cyclic electric field (max. ± 2 kV/mm) for a constant temperature is calculated. Chosen temperatures for the numerical simulation are 300 K, 350 K and 400 K. The simulation results for various temperatures are given in Fig. 6.5. As the temperature increases, the ferroelectric behaviour changes to antiferroelectric behaviour, as observed from experimental investigations.

6.5 Summary and conclusion

In this chapter, an alternative approach to solve the evolution equation in ferroelectric model has been introduced in order to improve the numerical efficiency. The model was then implemented in a finite element framework and presented the results for inhomogeneous boundary value problem were presented. Later, the model was extended to represent the behaviour of temperature dependency. From the simulation results, it has been shown that the discussed model is able predict the temperature dependent behaviour of ferroelectric ceramics such as thermal depolarisation and anti-ferroelectric behaviour.

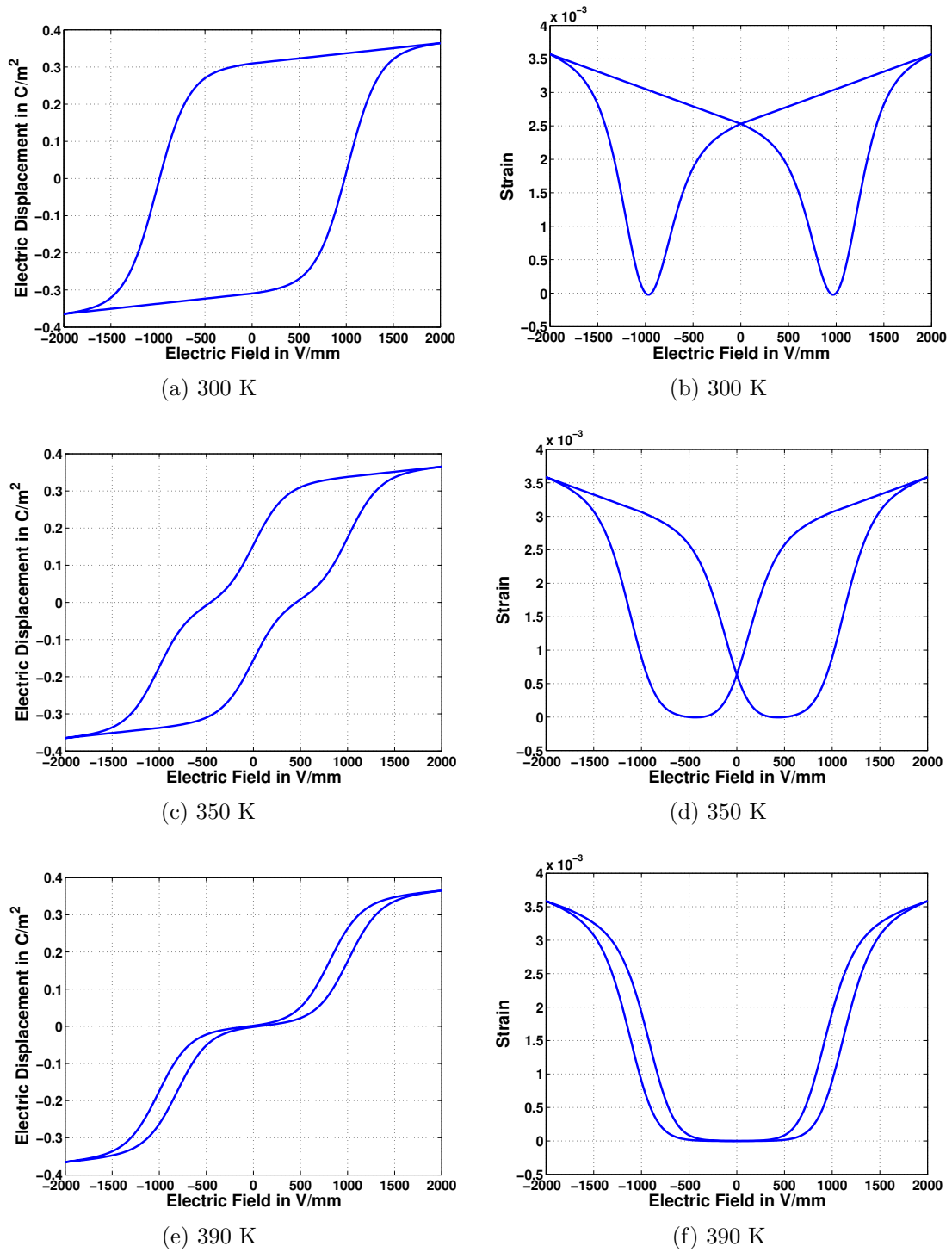


Figure 6.5: Simulation results of dielectric hysteresis (a,c,e) and butterfly hysteresis (b,d,f) at temperatures of 300 K, 350 K and 390 K.

7 Simulation of 1-3 piezocomposites

Predicting the effective behaviour of ferroelectric composite is very important in the improvement of ferroelectric applications. To capture the behaviour within a non-linear regime, finite element approaches are commonly used. In this chapter, a semi-analytical approach is used to calculate the effective behaviour of 1-3 composite. To have a comparative study, the finite element homogenisation framework is presented and related simulation results are discussed. Then, both the homogenisation methods are compared. In the first part of this chapter, elementary homogenisation techniques such as the Voigt and Reuss approach are discussed. Thereafter, a simple homogenisation method, particularly for 1-3 composite, is discussed. Then the simulation results obtained for this simple homogenisation method for various frequencies and volume fractions are presented. These simulation results are also compared with experimental data. In the second part of this chapter, the finite element homogenisation technique is discussed. Following that the results obtained from this technique is compared with experimental data. In the final part, a comparative study between both the semi-analytical method and the finite element homogenisation method is addressed.

7.1 Homogenisation methods

Voigt and Reuss are two well known homogenisation methods commonly used to predict the effective behaviour of composites. However, these procedures consider only the volume fraction of the constituents and ignore other factors such as the distribution of constituents, interfacial effects, etc. Despite of these procedures' simplification, these methods provide the range of the values of the effective properties. To consider the constituent distribution of the material, a simple homogenisation procedure is introduced. In this section, after the Voigt and the Reuss homogenisation procedure, a formulation for the simple homogenisation approach is discussed.

7.1.1 Voigt assumption

Within the Voigt approach, the strains and the electric field are assumed to be uniform in the material body considered. Consequently, the strain and the electric field are identical in both the matrix and the fiber material. This assumption leads to that the

stress and electric displacement of the composite are different in the matrix material and the fiber material. This assumption can be represented as

$$\begin{bmatrix} \boldsymbol{\varepsilon} \\ \mathbf{E} \end{bmatrix} = \begin{bmatrix} {}_f\boldsymbol{\varepsilon} \\ {}_f\mathbf{E} \end{bmatrix} = \begin{bmatrix} {}_m\boldsymbol{\varepsilon} \\ {}_m\mathbf{E} \end{bmatrix}, \quad (7.1)$$

$$\begin{bmatrix} \boldsymbol{\sigma} \\ \mathbf{D} \end{bmatrix} = v_f \begin{bmatrix} {}_f\boldsymbol{\sigma} \\ {}_f\mathbf{D} \end{bmatrix} + v_m \begin{bmatrix} {}_m\boldsymbol{\sigma} \\ {}_m\mathbf{D} \end{bmatrix}, \quad (7.2)$$

where ${}_f\boldsymbol{\sigma}$, ${}_m\boldsymbol{\sigma}$, ${}_f\mathbf{D}$, ${}_m\mathbf{D}$, ${}_f\boldsymbol{\varepsilon}$, ${}_m\boldsymbol{\varepsilon}$, ${}_f\mathbf{E}$, ${}_m\mathbf{E}$, v_f , v_m are the stresses in the fiber, the stresses in matrix, the electric displacement in the fiber, the electric displacement in the matrix, the strains in the fiber, the strains in the matrix, the electric field in the matrix, the electric field in the matrix, the volume fraction of the fiber and the volume fraction of the matrix, respectively. Combined with the constitutive relation for both fiber and matrix and for given strains and the electric field, the stresses, and the electric displacement for the fiber and the matrix material and also the stresses and the electric displacement for the composite can be calculated.

7.1.2 Reuss assumption

Contrary to the voigt assumption, the stresses and the electric displacement are assumed to be uniform throughout the material. So, the stresses and the electric displacement of the composite are identical to the stresses and electric displacement of the matrix and the fiber material. The strains and the electric field of the matrix, the fiber and the composite are related such that the weighted sum of the strain and the electric field of the matrix and fiber are equal to the strains and the electric field in the composite, respectively. These relations can be represented as

$$\begin{bmatrix} \boldsymbol{\sigma} \\ \mathbf{D} \end{bmatrix} = \begin{bmatrix} {}_f\boldsymbol{\sigma} \\ {}_f\mathbf{D} \end{bmatrix} = \begin{bmatrix} {}_m\boldsymbol{\sigma} \\ {}_m\mathbf{D} \end{bmatrix}, \quad (7.3)$$

$$\begin{bmatrix} \boldsymbol{\varepsilon} \\ \mathbf{E} \end{bmatrix} = v_f \begin{bmatrix} {}_f\boldsymbol{\varepsilon} \\ {}_f\mathbf{E} \end{bmatrix} + v_m \begin{bmatrix} {}_m\boldsymbol{\varepsilon} \\ {}_m\mathbf{E} \end{bmatrix}. \quad (7.4)$$

Combined with the constitutive relation for both fiber and matrix and for given strains and the electric field, the stresses, and the electric displacement for the fiber and the matrix material and also the stresses and the electric displacement for the composite can be calculated.

7.1.3 Simple homogenisation approach

All state variables and their conjugate flux terms are decomposed into a matrix part and a fibre part in combination with related homogenisation assumptions. In this context, volume fractions related to the matrix and fibre contributions are introduced. The constitutive relations applied to the fibre contributions are those introduced for bulk PZT, so that rate-dependent switching processes are accounted for at sufficiently high loading levels. The resulting non-linear system of equations representing the constitutive response of the 1-3 composite is iteratively solved for given loading conditions.

We assume Voigt-type conditions for the electric field in loading direction as well as for the related strains, i.e.

$$\mathbf{e}_i \cdot \boldsymbol{\varepsilon} \cdot \mathbf{e}_j = \mathbf{e}_i \cdot {}_f \boldsymbol{\varepsilon} \cdot \mathbf{e}_j = \mathbf{e}_i \cdot {}_m \boldsymbol{\varepsilon} \cdot \mathbf{e}_j \quad \text{for } (i, j) \in \{(1, 2), (2, 1), (3, 3)\}, \quad (7.5)$$

$$\mathbf{E} \cdot \mathbf{e}_k = {}_f \mathbf{E} \cdot \mathbf{e}_k = {}_m \mathbf{E} \cdot \mathbf{e}_k \quad \text{for } k \in \{3\}, \quad (7.6)$$

wherein the index f refers to the fibre contributions and wherein the index m indicates matrix contributions. The related stresses and dielectric displacements follow as

$$\mathbf{e}_i \cdot \boldsymbol{\sigma} \cdot \mathbf{e}_j = v_f \mathbf{e}_i \cdot {}_f \boldsymbol{\sigma} \cdot \mathbf{e}_j + v_m \mathbf{e}_i \cdot {}_m \boldsymbol{\sigma} \cdot \mathbf{e}_j \quad \text{for } (i, j) \in \{(1, 2), (2, 1), (3, 3)\}, \quad (7.7)$$

$$\mathbf{D} \cdot \mathbf{e}_k = v_f {}_f \mathbf{D} \cdot \mathbf{e}_k + v_m {}_m \mathbf{D} \cdot \mathbf{e}_k \quad \text{for } k \in \{3\}, \quad (7.8)$$

wherein $v_f \geq 0$ denotes the volume fraction of PZT fibres and $v_m \geq 0$ characterises the volume fraction of the matrix with $v_f + v_m = 1$. Moreover, Reuss-type conditions are assumed in the remaining directions, resulting in

$$\mathbf{e}_l \cdot \boldsymbol{\sigma} \cdot \mathbf{e}_o = \mathbf{e}_l \cdot {}_f \boldsymbol{\sigma} \cdot \mathbf{e}_o + \mathbf{e}_l \cdot {}_m \boldsymbol{\sigma} \cdot \mathbf{e}_o \quad \text{for } (l, o) \in \{(1, 1), (2, 2), (2, 3), \quad (7.9)$$

$$(3, 2), (1, 3), (3, 1)\},$$

$$\mathbf{D} \cdot \mathbf{e}_p = {}_f \mathbf{D} \cdot \mathbf{e}_p + {}_m \mathbf{D} \cdot \mathbf{e}_p \quad \text{for } p \in \{1, 2\}, \quad (7.10)$$

so that the related strains and electric field contributions follow as

$$\mathbf{e}_l \cdot \boldsymbol{\varepsilon} \cdot \mathbf{e}_o = v_f \mathbf{e}_l \cdot {}_f \boldsymbol{\varepsilon} \cdot \mathbf{e}_o + v_m \mathbf{e}_l \cdot {}_m \boldsymbol{\varepsilon} \cdot \mathbf{e}_o \quad \text{for } (l, o) \in \{(1, 1), (2, 2), (2, 3), \quad (7.11)$$

$$(3, 2), (1, 3), (3, 1)\},$$

$$\mathbf{E} \cdot \mathbf{e}_p = v_f {}_f \mathbf{E} \cdot \mathbf{e}_p + v_m {}_m \mathbf{E} \cdot \mathbf{e}_p \quad \text{for } p \in \{1, 2\}. \quad (7.12)$$

With these assumptions at hand, along with the constitutive relations, the stresses and strains as well as the dielectric displacements and the electric field in the individual constituents and the entire composite can be calculated for given macroscopic loading and boundary conditions.

7.2 Homogenisation algorithm for nonlinear behaviour

The aim of this algorithm is to compute the response of the stresses and the electric displacement of the composite for a given strain and the electric field. At loading step t_{n+1} , the strains and the electric field are known as they are the input quantities for this algorithm. Since the remnant polarisation at t_{n+1} is unknown, the remnant polarisation at t_n is taken as a trail value. The trail value of remnant polarisation is updated iteratively in the algorithm, if the switching condition is violated. For given loading conditions together with one of the homogenisation models discussed above, the stresses and the electrical displacement of the composite, matrix and fiber are computed. From the field variables obtained for fiber, the switching criterion is checked. Internal variables are then updated according to the switching criterion. While updating the internal variables, the homogenisation assumptions are satisfied parallelly. Thus at the end of each iteration, the stresses and the electric displacement of the composite are obtained for the updated remnant polarisation. This procedure is summarized in Tab. 7.1.

Table 7.1: Algorithmic sketch of the constitutive driver for rate dependent response of the ferroelectric composite material.

<p>Given: $\sigma_{n+1}^{\text{ext}}, \mathbf{E}_{n+1}, \varepsilon_n, {}_f\mathbf{P}_n^i$ (remnant polarisation of the fiber)</p> <p>Set: $\varepsilon_{n+1} = \varepsilon_n, {}_f\mathbf{P}_{n+1}^i = {}_f\mathbf{P}_n^i$</p> <p>Compute: $\mathbf{R}_l, \mathbf{R}_g$</p> <p>DOWHILE: $\ \mathbf{R}_g\ \geq \text{tol}_g$</p> <p style="padding-left: 2em;">DOWHILE: $\ \mathbf{R}_l\ \geq \text{tol}_l$</p> <p style="padding-left: 2em;">Compute:</p> <p style="padding-left: 4em;">$\sigma_{n+1, f}, \sigma_{n+1, m}, \mathbf{D}_{n+1, f}, \mathbf{D}_{n+1, m}, \mathbf{E}_{n+1, f}, \mathbf{E}_{n+1, m}$</p> <p style="padding-left: 4em;">using equations (6.2) and (6.3) along with the homogenisation equations (7.1)-(7.2) or (7.3)-(7.4) or (7.5)-(7.12) according to the assumed homogenisation approach.</p> <p style="padding-left: 4em;">$\mathbf{R}_l = {}_f\mathbf{P}_{n+1}^i - {}_f\mathbf{P}_n^i - \Delta t \lambda_{n+1} \frac{2}{E_c^2} \left[\mathbf{E}_{n+1} + \frac{\partial \bar{\psi}}{\partial {}_f\mathbf{P}_{n+1}^i} \right]$</p> <p style="padding-left: 4em;">${}_f\mathbf{P}_{n+1}^i \leftarrow {}_f\mathbf{P}_{n+1}^i - \left[\frac{d\mathbf{R}_l}{d{}_f\mathbf{P}_{n+1}^i} \right]^{-1} \cdot \mathbf{R}_l$</p> <p style="padding-left: 2em;">END</p> <p style="padding-left: 2em;">$\mathbf{R}_g = \sigma_{n+1}^{\text{ext}} - \sigma_{n+1}$</p> <p style="padding-left: 4em;">$\varepsilon_{n+1} \leftarrow \varepsilon_{n+1} - \left[\frac{d\mathbf{R}_g}{d\varepsilon_{n+1}} \right]^{-1} : \mathbf{R}_g$</p> <p>END</p>
--

7.3 Finite element homogenisation procedure

To predict the non-linear behaviour of a composite, the finite element method is the commonly used procedure. In this section, the rate dependent ferroelectric model discussed in the chapter 3 is applied to a homogenisation procedure for 1-3 ferrocomposites. The simulation has been performed for various volume fraction under different frequency of loading.

In order to simulate effective properties of a 1-3 piezocomposite by means of the finite element formulation discussed, a discretisation of a Representative Volume Element (RVE) type specimen shall be considered. In comparing the elastic properties of matrix material and fiber material, the volume fraction is more influential than the shape of the fiber for the boundary value problems considered in this work. Therefore a square fiber is chosen to simplify the RVE and also to accommodate the composites with different volume fractions. This RVE includes areas of bulk PZT and areas of matrix material, which is assumed to be isotropic and linear elastic. Accordingly, the discretisation, respectively the constitutive relations referred to individual finite elements, depends on the underlying volume fraction of PZT fibres. In view of the cartesian axes illustrated in Fig. 7.1, the mechanical boundary conditions chosen include $u_3|_{x_3=\min} = 0$. Moreover, the displacements $u_3|_{x_3=\max}$, $u_1|_{x_1=\min}$, $u_1|_{x_1=\max}$, $u_2|_{x_2=\min}$ and $u_2|_{x_2=\max}$ shall be uniform. For the respective surfaces, the latter conditions are implemented in terms of a linear constraint. Electrical boundary conditions are prescribed by $\phi|_{x_3=\min} = 0$ and $\phi|_{x_3=\max} = \phi_{\text{ext}}$.

Since the response of the RVE-type specimen is homogeneous in the direction of electrical loading, only one element in thickness direction is used for the discretisation. The total discretisation consists of 256, 256 and 324 hexahedral elements for fiber volume fraction of 80 %, 65 %, 35 %, respectively. The effective response of the composite is obtained by volume-averaging quantities of interest such as $\langle \boldsymbol{\sigma} \rangle_{\mathcal{B}}$ and $\langle \mathbf{D} \rangle_{\mathcal{B}}$ with

$$\langle \bullet \rangle_{\mathcal{B}} = \frac{1}{v_{\mathcal{B}}} \int_{\mathcal{B}} \bullet \, dv. \quad (7.13)$$

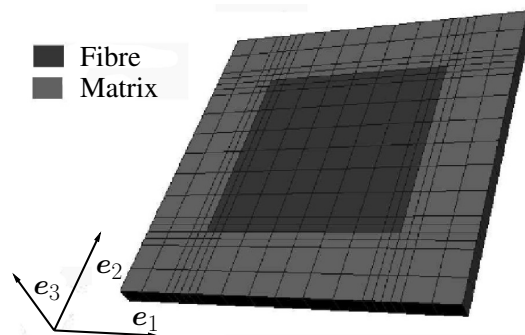


Figure 7.1: Finite element mesh representing a piezocomposite with a PZT volume fraction of 35 %.

7.4 Simulation results

The piezocomposites are simulated in two ways. First the simple homogenisation approach is applied. For the matrix material, a linear uncoupled electroelastic material model has been considered. The related material parameters are shown in Tab. 7.2. With this assumption, the piezocomposites are simulated for various electric loading frequencies such as 1 Hz, 5 Hz, 10 Hz, 25 Hz, and for various fibre volume fractions such as 0.8, 0.65, 0.35. The finite element simulations are referred to the same loading and volume fractions and the simulation results are compared with the experimental data. The electric loading cycle applied is given in Fig. 3.1. The simulation results of the last full cycle are compared with experimental data. This comparison between the simulation results obtained using a simple homogenisation approach and the finite element method along with experimental data for the fibre volume fraction of 0.8, 0.65, 0.35 is given in Fig. 7.2, 7.3 and 7.4, respectively.

It is observed from the comparison that the simulation results obtained from the simple homogenisation approach and finite element approach are quasi-identical. However, a small deviation in the butterfly hysteresis results of these two approaches can be seen in the simulation for the volume fraction of 0.35 at 1 Hz. It has been observed that the change in strain during the polarisation switching is larger in the finite element approach than in the simple homogenisation approach.

Table 7.2: Material parameters for matrix material.

param.	name	unit	value
λ	Lamé parameter	kN/m ²	1.67×10^6
μ	Lamé parameter	kN/m ²	1.115×10^6
γ	Electric permittivity	C ² /(kN m ²)	-0.02×10^6

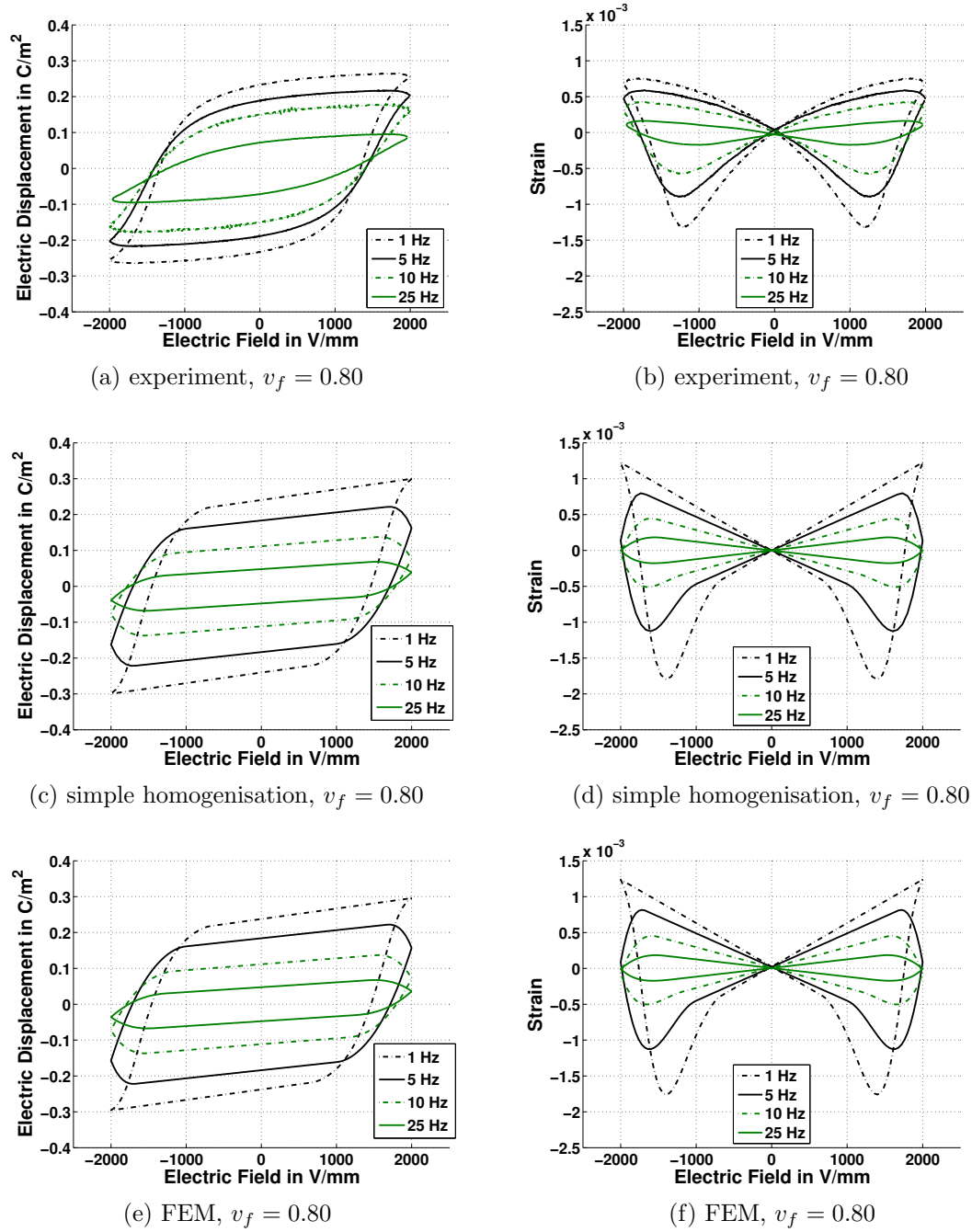


Figure 7.2: Rate-dependent ferroelectric hysteresis at 1 Hz, 5 Hz, 10 Hz and 25 Hz: for a fibre volume fraction of 0.8 (a) experiment, (c) simple homogenisation approach and (e) FEM; related butterfly curves: (b) experiment, (d) simple homogenisation approach and (f) FEM.

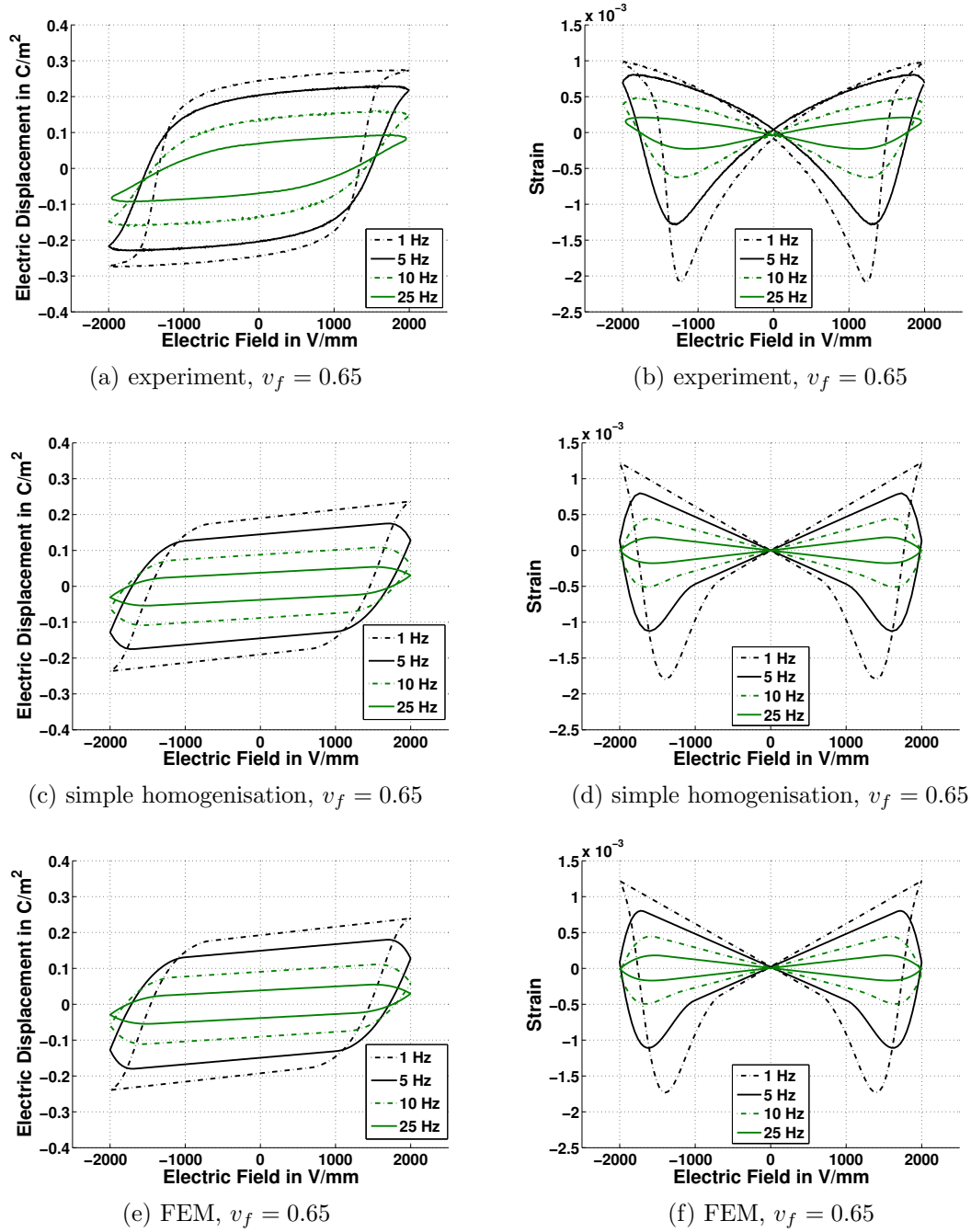


Figure 7.3: Rate-dependent ferroelectric hysteresis at 1 Hz, 5 Hz, 10 Hz and 25 Hz: for a fibre volume fraction of 0.65 (a) experiment, (c) simple homogenisation approach and (e) FEM; related butterfly curves: (b) experiment, (d) simple homogenisation approach and (f) FEM.

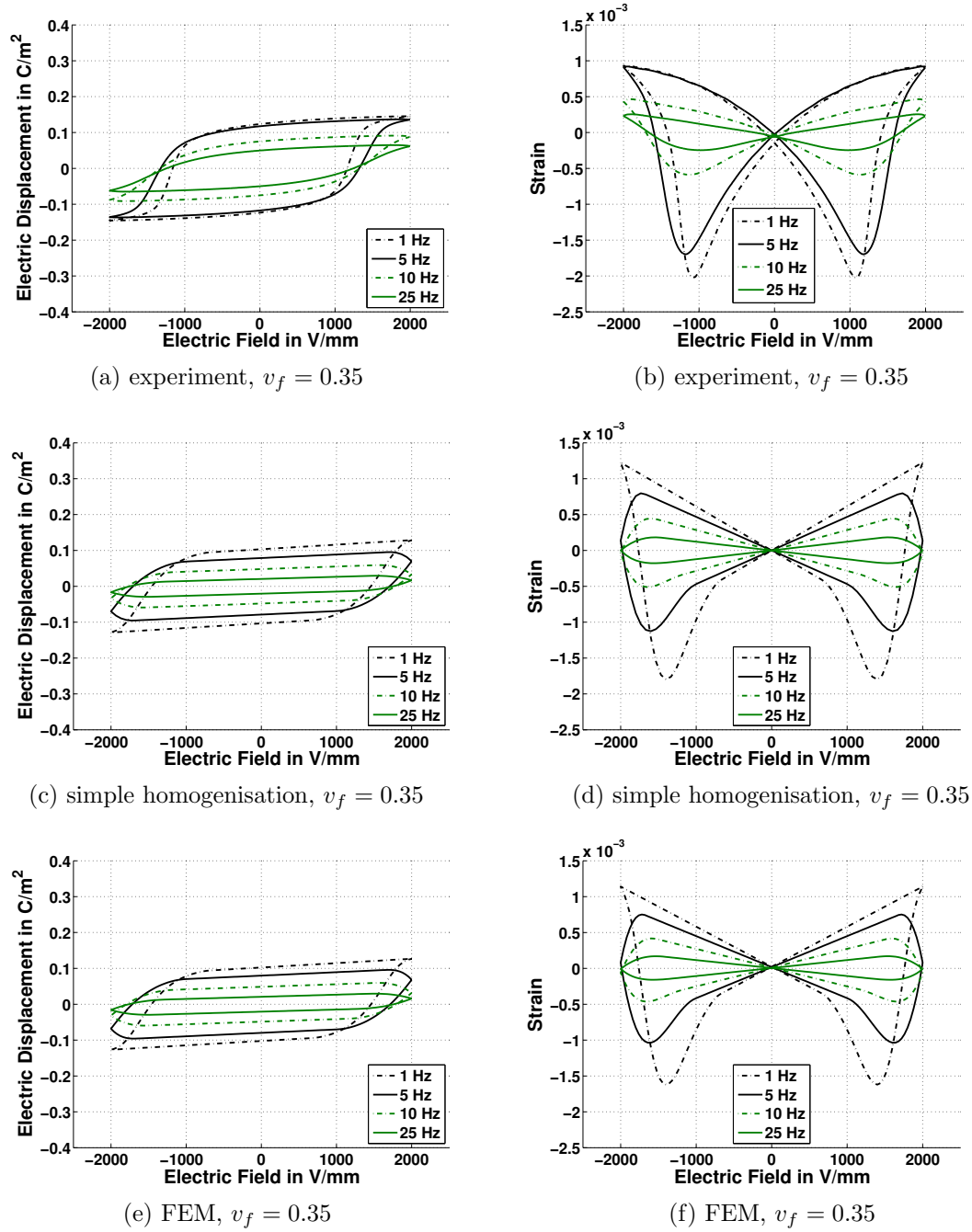


Figure 7.4: Rate-dependent ferroelectric hysteresis at 1 Hz, 5 Hz, 10 Hz and 25 Hz: for a fibre volume fraction of 0.35 (a) experiment, (c) simple homogenisation approach and (e) FEM; related butterfly curves: (b) experiment, (d) simple homogenisation approach and (f) FEM.

7.5 A comparative study between two approaches

To obtain a quantitative comparison between simulation results and the experiments, the difference in the results of both approaches on total change in remnant polarisation, and total change in strain for different frequencies and volume fractions are plotted as shown in Fig. 7.5 and 7.6, respectively. From the comparison plot, it could be observed that the total change in remnant polarisation shows a reduction as the volume fraction of fiber reduces. The simulation results could capture this reducing behaviour. The total change in strain is observed to remain unchanged as the volume fraction decreases as for as the frequency remains the same. This behaviour is successfully captured by the simulations. However, some deviations in this trend could be observed in the experimental results at $v_f = 0.8$. Nevertheless, the change in behaviour of the composite for different frequencies is successfully captured in both simulation approaches.

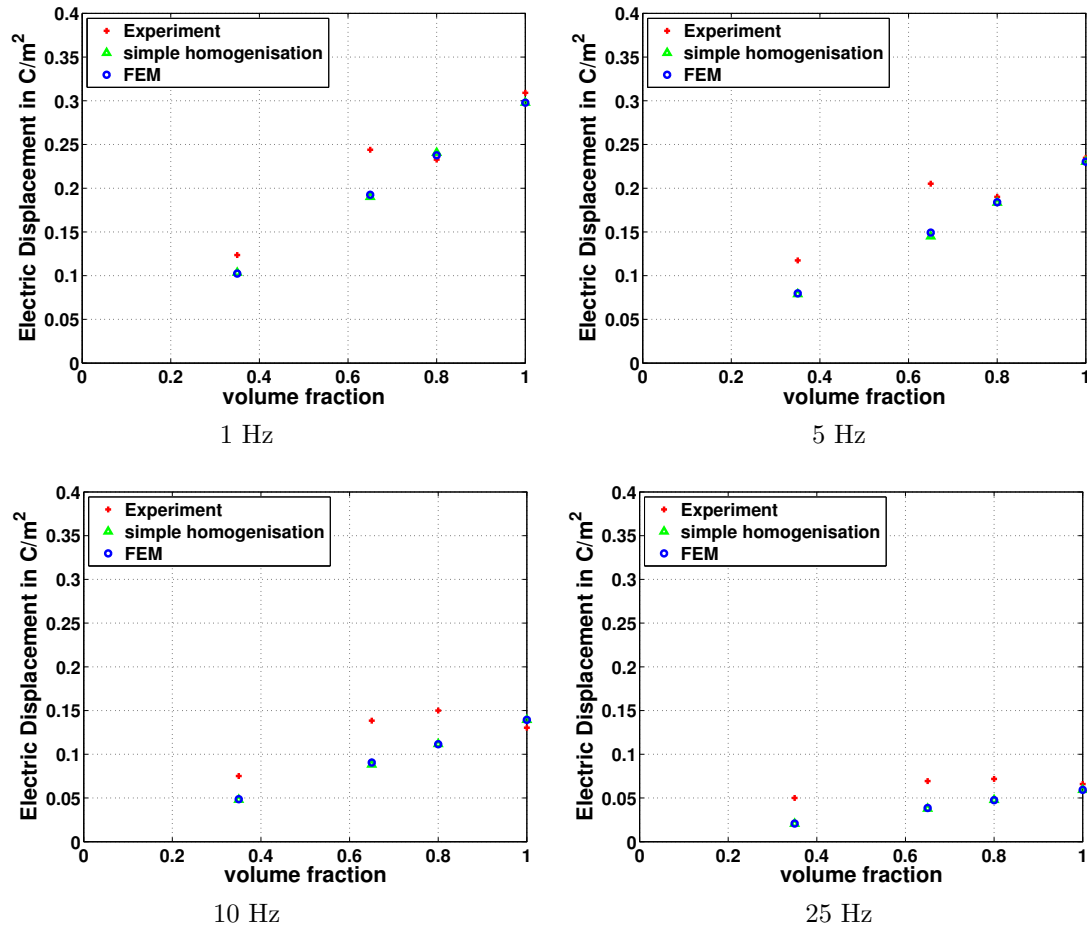


Figure 7.5: Comparison plot of maximum change in remnant polarisation between experiment, simple homogenisation and FEM for different frequencies and volume fractions.

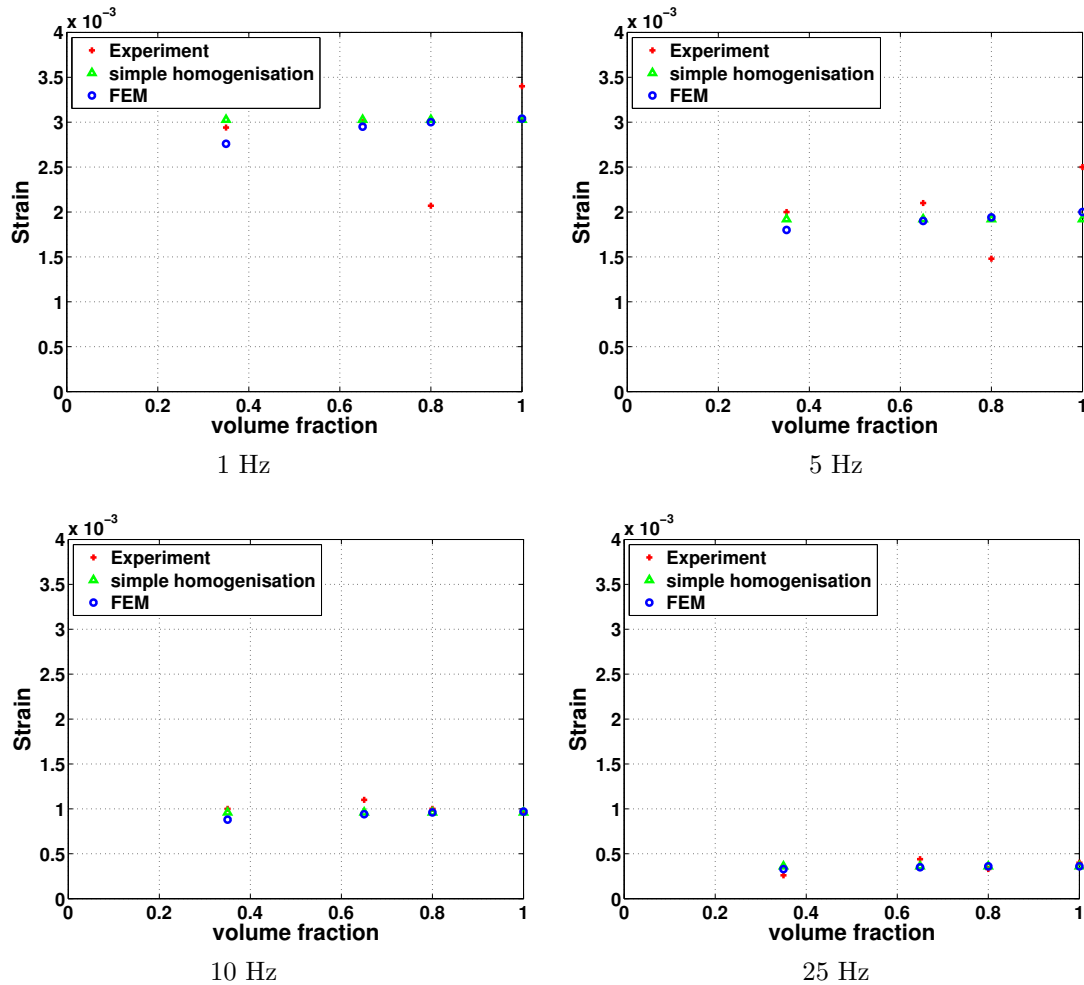


Figure 7.6: Comparison plot of maximum change in strain between experiment, simple homogenisation and FEM for different frequencies and volume fractions.

7.6 Summary and conclusion

In this chapter, a rate dependent constitutive model for ferroelectric material behaviour is used to capture the constitutive behaviour of PZT fibres in a piezocomposite and is combined with a simple homogenisation approach. Moreover, a finite element approach for a homogenisation approach is discussed. Thereafter, the experimental data for piezocomposites at different electrical loading frequencies and the results obtained for both simulation approaches are compared. The prediction of the simple homogenisation approach and finite element analysis for various volume fractions is in good agreement with the experimental results. The results of the simple homogenisation approach and the finite element analysis are almost identical. However, there is a notable difference for electrical loading 1 Hz and for 35% volume fraction, see Fig. 7.4(d,f). This difference results from the tensile stress exerted on the fibre material due to kinematic interactions with the matrix material in the lateral direction. In this chapter,

the matrix material used for the analysis is soft in nature as opposed to the fibre. In the case of a matrix material with higher stiffness, the effect of the tensile stress on the fibre in the lateral direction is expected to be more pronounced. This effect can, in general, be captured more appropriately within a finite element analysis than in the simple homogenisation approach. In addition to the effect of lateral stresses, the stresses can also cause mechanical depolarisation.

8 Summary and future work

The present work deals with the formulation and numerical implementation of phenomenological models of ferroelectric ceramics. At first, a thermodynamic framework for an electromechanical model along with the principle field theories is introduced. A rate dependent ferroelectric model was then developed and compared with experimental data. The results showed that the model was able to capture the effect of loading frequencies very well. A multisurface model was then introduced to capture the minor ferroelectric hysteresis as well as the asymmetric butterfly hysteresis which was observed in the experiments. The numerical results were then compared with experimental data. From the presented numerical results, it became evident that the model was able to capture different behaviour patterns due to the changes in maximum applied electric field. It was also shown that the model was able to capture a decreasing offset polarisation which has been observed in the ferroelectric material which was undergone electrical fatigue. Later, with the idea of extending the introduced model to capture additional phenomena such as ferroelastic hysteresis as well as mechanical depolarisation, a ferroelectric model was introduced with an additional internal variable. This model was formulated so as to be able to capture the anisotropic behaviour in ferroelectric switching. Simulation results were then compared qualitatively to experimental data taken from the literature. A rate independent ferroelectric model was then introduced. The model is formulated such that it was able to capture the ferroelectric behaviour for nonlinear hardening without an iteration procedure solving for the internal variables. Due to such an algorithmic formulation, the numerical efficiency of the model could be improved. The model was then implemented in a finite element framework and an inhomogeneous boundary value problem was solved. Later, this model was extended to capture the temperature dependent behaviour, especially the thermal depolarisation and antiferroelectric behaviour. Simulation results showed the model's capability of capturing these temperature dependent behaviour. Finally, the introduced rate dependent model was used in a homogenisation method to determine the behaviour of ferrocomposites. Two different methods were introduced where one was a semianalytical method and where the other one used the finite element method. The simulation results were then compared with experimental data for various loading frequencies and the results compared very well.

Various models introduced in this work are quite efficient and well capable of capturing different kinds of behaviour of ferroelectric ceramics. As a future work, the essential features of these models could be brought together into a single robust model in order to obtain an all purpose model for capturing various phenomena. The formulation of analytical tangent operator for all the introduced models within the implementation in a finite element framework will be a considerable improvement in numerical efficiency. In ferromagnetism, ferromagnetic hysteresis behaviour under external stress is very similar to anti-ferroelectric hysteresis behaviour [63]. Therefore, the model which can capture anti-ferroelectric behaviour could be extended to include ferromagnetic behaviour as well.

A Notes on the finite element formulation

In this appendix, a finite element formulation for the simulation of the composite is summarised. The global representation of the local balance equations (3.1,3.4) in weak form results in

$$\int_{\mathcal{B}} \mathbf{u}_* \cdot [\nabla \cdot \boldsymbol{\sigma} + \mathbf{b}] dv = 0, \quad \int_{\mathcal{B}} \phi_* [\nabla \cdot \mathbf{D} - q] dv = 0, \quad (\text{A.1})$$

wherein \mathbf{u}_* and ϕ_* denote suitable test functions; see, amongst others, Denzer and Menzel [33] and Dusthakar et al [28]. As this work proceeds, the body forces \mathbf{b} and charge densities q will be neglected. Straightforward application of integration by parts and the divergence theorem render the well-established representations

$$\int_{\mathcal{B}} \boldsymbol{\sigma} : \nabla \mathbf{u}_* dv - \int_{\partial \mathcal{B}} \mathbf{t} \cdot \mathbf{u}_* da = 0, \quad \int_{\mathcal{B}} \mathbf{D} \cdot \nabla \phi_* dv - \int_{\partial \mathcal{B}} d \phi_* da = 0, \quad (\text{A.2})$$

with $\mathbf{t} = \boldsymbol{\sigma} \cdot \mathbf{n}$ and $d = \mathbf{D} \cdot \mathbf{n}$, whereby \mathbf{n} is the outward normal unit vector.

Since both types of degrees of freedom, i.e. the displacement and the electric potential, enter the formulation in terms of their gradients in space only, identical shape functions are used to approximate these fields. On the level of an individual finite element one obtains

$$\begin{aligned} \mathbf{u}^h &= \sum_i^{n_{en}} N^i \mathbf{u}^i, & \mathbf{u}_*^h &= \sum_i^{n_{en}} N^i \mathbf{u}_*^i, \\ \phi^h &= \sum_i^{n_{en}} N^i \phi^i, & \phi_*^h &= \sum_i^{n_{en}} N^i \phi_*^i. \end{aligned} \quad (\text{A.3})$$

so that the gradients of these approximations follow straightforwardly. Moreover, an isoparametric framework is adopted.

Next, let $\mathbf{A}_{e=1}^{n_{el}}$ represent the assembly operation over all elements. This allows us to represent the coupled non-linear system of equations in residual form as

$$\begin{aligned} r_{\mathbf{u}}^I &= \mathbf{A}_{e=1}^{n_{el}} \int_{\mathcal{B}^e} \boldsymbol{\sigma} \cdot \nabla N^A dv - \mathbf{A}_{e=1}^{n_{el}} \int_{\partial \mathcal{B}^e} N^A \mathbf{t} da = \mathbf{0} \quad \forall I = 1, \dots, n_{np}, \\ r_{\phi}^J &= \mathbf{A}_{e=1}^{n_{el}} \int_{\mathcal{B}^e} \mathbf{D} \cdot \nabla N^C dv - \mathbf{A}_{e=1}^{n_{el}} \int_{\partial \mathcal{B}^e} N^C d da = 0 \quad \forall J = 1, \dots, n_{np}. \end{aligned} \quad (\text{A.4})$$

Application of a standard Newton scheme results in the iterative updates $\mathbf{r}_{\mathbf{u}l+1}^I = \mathbf{r}_{\mathbf{u}l}^I + \Delta\mathbf{r}_{\mathbf{u}}^I$ and $r_{\phi l+1}^J = r_{\phi l}^J + \Delta r_{\phi}^J$ with iteration index l and

$$\begin{aligned}\Delta\mathbf{r}_{\mathbf{u}}^I &= \sum_{K=1}^{n_{\text{np}}} \frac{d\mathbf{r}_{\mathbf{u}}^I}{d\mathbf{u}^K} \cdot \Delta\mathbf{u}^K + \sum_{L=1}^{n_{\text{np}}} \frac{d\mathbf{r}_{\mathbf{u}}^I}{d\phi^L} \Delta\phi^L, \\ \Delta r_{\phi}^J &= \sum_{K=1}^{n_{\text{np}}} \frac{dr_{\phi}^J}{d\mathbf{u}^K} \cdot \Delta\mathbf{u}^K + \sum_{L=1}^{n_{\text{np}}} \frac{dr_{\phi}^J}{d\phi^L} \Delta\phi^L.\end{aligned}\tag{A.5}$$

Bibliography

- [1] IEEE standard on piezoelectricity. *ANSI/IEEE Std 176-1987*, 1988. doi:[10.1109/IEEESTD.1988.79638](https://doi.org/10.1109/IEEESTD.1988.79638). 17
- [2] J. Aboudi. Micromechanical prediction of the effective coefficients of thermo-piezoelectric multiphase composites. *Journal of Intelligent Material Systems and Structures*, 9(9): 713–722, 1998. 24
- [3] G. Arlt. Twinning in ferroelectric and ferroelastic ceramics: stress relief. *Journal of Materials Science*, 25(6):2655–2666, 1990. doi:[10.1007/BF00584864](https://doi.org/10.1007/BF00584864). 8
- [4] G. Arlt, D. Hennings, and G. de With. Dielectric properties of fine-grained barium titanate ceramics. *Journal of Applied Physics*, 58(4), 1985. 18
- [5] A. Arockiarajan, B. Delibas, A. Menzel, and W. Seemann. Studies on rate-dependent switching effects of piezoelectric materials using a finite element model. *Computational Materials Science*, 37:306–317, 2006. 21
- [6] A. Arockiarajan, A. Menzel, B. Delibas, and W. Seemann. Computational modeling of rate-dependent domain switching in piezoelectric materials. *European Journal of Mechanics A/Solids*, 25:950–964, 2006. 21
- [7] A. Arockiarajan, S. M. Sivakumar, and C. Sansour. A thermodynamically motivated model for ferroelectric ceramics with grain boundary effects. *Smart Materials and Structures*, 19(1):015008, 2010. 21
- [8] Y. Bai, X. Han, X. Zheng, and L. Qiao. Both high reliability and giant electrocaloric strength in BaTiO₃ ceramics. *Scientific Reports*, 3:2895, 2013. 14, 19
- [9] H. Banno. Recent developments of piezoelectric ceramic products and composites of synthetic rubber and piezoelectric ceramic particles. *Ferroelectrics*, 50(1):3–12, 1983. doi:[10.1080/00150198308014425](https://doi.org/10.1080/00150198308014425). 24
- [10] E. Bassiouny and G. Maugin. Thermodynamical formulation for coupled electromechanical hysteresis effects-iii. parameter identification. *International Journal of Engineering Science*, 27(8):975–987, 1989. doi:[10.1016/0020-7225\(89\)90038-4](https://doi.org/10.1016/0020-7225(89)90038-4). 22
- [11] E. Bassiouny and G. Maugin. Thermodynamical formulation for coupled electromechanical hysteresis effects-iv. combined electromechanical loading. *International Journal of Engineering Science*, 27(8):989–1000, 1989. doi:[10.1016/0020-7225\(89\)90039-6](https://doi.org/10.1016/0020-7225(89)90039-6). 22
- [12] E. Bassiouny, A. Ghaleb, and G. Maugin. Thermodynamical formulation for coupled electromechanical hysteresis effects-i. basic equations. *International Journal of Engineering Science*, 26(12):1279–1295, 1988. doi:[10.1016/0020-7225\(88\)90047-X](https://doi.org/10.1016/0020-7225(88)90047-X).
- [13] E. Bassiouny, A. Ghaleb, and G. Maugin. Thermodynamical formulation for coupled electromechanical hysteresis effects-ii. poling of ceramics. *International Journal of En-*

- gineering Science*, 26(12):1297–1306, 1988. doi:[10.1016/0020-7225\(88\)90048-1](https://doi.org/10.1016/0020-7225(88)90048-1). 22
- [14] Y. Benveniste. A new approach to the application of mori-tanaka’s theory in composite materials. *Mechanics of Materials*, 6(2):147 – 157, 1987. doi:[http://dx.doi.org/10.1016/0167-6636\(87\)90005-6](http://dx.doi.org/10.1016/0167-6636(87)90005-6). 25
- [15] Y. Benveniste. Universal relations in piezoelectric composites with eigenstress and polarization fields, part ii: Multiphase media-effective behavior. *J. Appl. Mech.*, 60:270–275, 1993. 25
- [16] G. Bonnet. Effective properties of elastic periodic composite media with fibers. *Journal of the Mechanics and Physics of Solids*, 55(5):881 – 899, 2007. doi:<http://dx.doi.org/10.1016/j.jmps.2006.11.007>. 25
- [17] T. H. Brockmann. *Theory of Adaptive Fiber Composites: From Piezoelectric Material Behavior to Dynamics of Rotating Structures*. Springer Publishing Company, Incorporated, 2009. 14
- [18] H. Cao and A. G. Evans. Nonlinear deformation of ferroelectric ceramics. *Journal of the American Ceramic Society*, 76(4):890–896, 1993. doi:[10.1111/j.1151-2916.1993.tb05312.x](https://doi.org/10.1111/j.1151-2916.1993.tb05312.x). 18
- [19] P. J. Chen. Three dimensional dynamic electromechanical constitutive relations for ferroelectric materials. *International Journal of Solids and Structures*, 16(12):1059 – 1067, 1980. doi:[http://dx.doi.org/10.1016/0020-7683\(80\)90063-3](http://dx.doi.org/10.1016/0020-7683(80)90063-3). 22
- [20] P. Chen and M. Madsen. One dimensional polar responses of the electrooptic ceramic plzt 7/65/35 due to domain switching. *Acta Mechanica*, 41(3-4):255–264, 1981. doi:[10.1007/BF01177351](https://doi.org/10.1007/BF01177351).
- [21] P. Chen and P. Peercy. One dimensional dynamic electromechanical constitutive relations of ferroelectric materials. *Acta Mechanica*, 31(3-4):231–241, 1979. doi:[10.1007/BF01176851](https://doi.org/10.1007/BF01176851). 22
- [22] W. Chen and C. S. Lynch. A model for simulating polarization switching and a-f phase changes in ferroelectric ceramics. *Journal of Intelligent Material Systems and Structures*, 9(6):427–431, 1998. 20
- [23] W. Chen and C. Lynch. A micro-electro-mechanical model for polarization switching of ferroelectric materials. *Acta Materialia*, 46(15):5303–5311, 1998. doi:[10.1016/S1359-6454\(98\)00207-9](https://doi.org/10.1016/S1359-6454(98)00207-9). 20
- [24] Z.-X. Chen, Y. Chen, and Y.-S. Jiang. DFT study on ferroelectricity of BaTiO₃. *The Journal of Physical Chemistry B*, 105(24):5766–5771, 2001. doi:[10.1021/jp0032558](https://doi.org/10.1021/jp0032558). 19
- [25] A. C. Cocks and R. M. McMeeking. A phenomenological constitutive law for the behaviour of ferroelectric ceramics. *Ferroelectrics*, 228(1):219–228, 1999. doi:[10.1080/00150199908226136](https://doi.org/10.1080/00150199908226136). 22
- [26] B. Coleman and W. Noll. The thermodynamics of elastic materials with heat conduction and viscosity. *Archive of Rational Mechanics and Analysis*, 13:167–178, 1963. 34, 46
- [27] C. N. Della and D. Shu. The performance of 1-3 piezoelectric composites with a porous non-piezoelectric matrix. *Acta Materialia*, 56(4):754 – 761, 2008. doi:<http://dx.doi.org/10.1016/j.actamat.2007.10.022>. 25

- [28] R. Denzer and A. Menzel. Configurational forces for quasi-incompressible large strain electro-viscoelasticity application to fracture mechanics. *European Journal of Mechanics A/Solids*, 48:3–15, 2014. 99
- [29] A. Devonshire. XCVI. Theory of barium titanate. *Philosophical Magazine*, 40(309):1040–1063, 1949. 22
- [30] A. Devonshire. CIX. Theory of barium titanate-part ii. *Philosophical Magazine*, 42(333):1065–1079, 1951. 22
- [31] M. L. Dunn and M. Taya. An analysis of piezoelectric composite materials containing ellipsoidal inhomogeneities. *Proceedings: Mathematical and Physical Sciences*, 443(1918): pp. 265–287, 1993. 25
- [32] M. Dunn and M. Taya. Micromechanics predictions of the effective electroelastic moduli of piezoelectric composites. *International Journal of Solids and Structures*, 30(2):161 – 175, 1993. doi:[http://dx.doi.org/10.1016/0020-7683\(93\)90058-F](http://dx.doi.org/10.1016/0020-7683(93)90058-F). 25
- [33] D. Dusthakar, A. Menzel, and B. Svendsen. Comparison of phenomenological and laminate-based models for rate-dependent switching in ferroelectric continua. *GAMM Mitteilungen*, 38(1):147–170, 2015. 99
- [34] M. Elhadrouz, T. B. Zineb, and E. Patoor. Constitutive law for ferroelastic and ferroelectric piezoceramics. *Journal of Intelligent Material Systems and Structures*, 16(3):221–236, 2005. doi:[10.1177/1045389X05049650](https://doi.org/10.1177/1045389X05049650). 21
- [35] J. D. Eshelby. The Determination of the Elastic Field of an Ellipsoidal Inclusion, and Related Problems. *Proceedings of The Royal Society A: Mathematical, Physical and Engineering Sciences*, 241:376–396, 1957. doi:[10.1098/rspa.1957.0133](https://doi.org/10.1098/rspa.1957.0133). 25
- [36] D. Fang and C. Li. Nonlinear electric-mechanical behavior of a soft PZT-51 ferroelectric ceramic. *Journal of Materials Science*, 34(16):4001–4010, 1999. 17
- [37] T. Fett, S. Muller, D. Munz, and G. Thun. Nonsymmetry in the deformation behaviour of PZT. *Journal of Materials Science Letters*, 17(4):261–265, 1998. 18
- [38] A. Garcia and D. Vanderbilt. Electromechanical behavior of BaTiO₃ from first principles. *Applied Physics Letters*, 72(23), 1998. 19
- [39] J. E. Garcia, D. A. Ochoa, V. Gomis, J. A. Eiras, and R. Pérez. Evidence of temperature dependent domain wall dynamics in hard lead zirconate titanate piezoceramics. *Journal of Applied Physics*, 112(1):014113, 2012. doi:<http://dx.doi.org/10.1063/1.4736582>. 18
- [40] P. Gaudenzi and K. Bathe. An iterative finite element procedure for the analysis of piezoelectric continua. *Journal of Intelligent Material Systems and Structures*, 6(2):266–273, 1995. 24
- [41] Y. González-Abreu, A. Peláiz-Barranco, A. C. Garcia-Wong, and J. D. S. Guerra. The pyroelectric behavior of lead free ferroelectric ceramics in thermally stimulated depolarization current measurements. *Journal of Applied Physics*, 111(12):124102, 2012. doi:<http://dx.doi.org/10.1063/1.4729918>. 18
- [42] M. Grewe, T. Gururaja, T. R. Shrout, and R. E. Newnham. Acoustic properties of particle/polymer composites for ultrasonic transducer backing applications. *IEEE Transactions on Ultrasonics, Ferroelectrics, and Frequency Control*, 37(6):506–514, 1990.

- doi:[10.1109/58.63106](https://doi.org/10.1109/58.63106). 19
- [43] D. J. Griffiths. *Introduction to Electrodynamics (3rd Edition)*. Benjamin Cummings, 1998. 30
- [44] N. W. Hagood, R. Kindel, K. Ghandi, and P. Gaudenzi. Improving transverse actuation of piezoceramics using interdigitated surface electrodes. *Proc. SPIE*, 1917:341–352, 1993. 14
- [45] T. Hiroshi and C. Nakaya. PZT/polymer composites for medical ultrasonic probes. *Ferroelectrics*, 68(1):53–61, 1986. doi:[10.1080/00150198608238737](https://doi.org/10.1080/00150198608238737). 19
- [46] J. A. Hossack and G. Hayward. Finite-element analysis of 1-3 composite transducers. *IEEE Transactions on Ultrasonics Ferroelectrics and Frequency Control*, 38:618–629, 1991. doi:[10.1109/58.108860](https://doi.org/10.1109/58.108860). 25
- [47] J. H. Huang and W.-S. Kuo. Micromechanics determination of the effective properties of piezoelectric composites containing spatially oriented short fibers. *Acta Materialia*, 44(12):4889 – 4898, 1996. doi:[http://dx.doi.org/10.1016/S1359-6454\(96\)00090-0](http://dx.doi.org/10.1016/S1359-6454(96)00090-0). 25
- [48] J. Huber and N. Fleck. Multi-axial electrical switching of a ferroelectric: theory versus experiment. *Journal of the Mechanics and Physics of Solids*, 49:785 – 811, 2001. 17, 21
- [49] J. Huber, N. Fleck, C. Landis, and R. McMeeking. A constitutive model for ferroelectric polycrystals. *Journal of the Mechanics and Physics of Solids*, 47(8):1663–1697, 1999. doi:[10.1016/S0022-5096\(98\)00122-7](https://doi.org/10.1016/S0022-5096(98)00122-7). 20
- [50] Y. Huo and Q. Jiang. Modeling of domain switching in polycrystalline ferroelectric ceramics. *Smart Materials and Structures*, 86(4):441–447, 1997. 21
- [51] S. Hwang, J. Huber, R. McMeeking, and N. Fleck. The simulation of switching in polycrystalline ferroelectric ceramics. *Journal of Applied Physics*, 84(3):1530–1540, 1998. doi:[10.1063/1.368219](https://doi.org/10.1063/1.368219). 17, 20
- [52] S. C. Hwang, J. E. Huber, R. M. McMeeking, and N. A. Fleck. The simulation of switching in polycrystalline ferroelectric ceramics. *Journal of Applied Physics*, 84(3), 1998. 20
- [53] B. Jaffe, W. R. Cook, and H. L. Jaffe. *Piezoelectric Ceramics*. 1971. 5
- [54] K. Jayabal, A. Menzel, A. Arockiarajan, and S. M. Srinivasan. Micromechanical modelling of switching phenomena in polycrystalline piezoceramics: Application of a polygonal finite element approach. *Comput. Mech.*, 48(4):421–435, October 2011. doi:[10.1007/s00466-011-0595-4](https://doi.org/10.1007/s00466-011-0595-4). 21
- [55] R. Jayendiran and A. Arockiarajan. Non-linear electromechanical response of 1-3 type piezocomposites. *International Journal of Solids and Structures*, 50(14-15):2259 – 2270, 2013. doi:<http://dx.doi.org/10.1016/j.ijsolstr.2013.03.032>. 19, 43
- [56] R. Jayendiran and A. Arockiarajan. Investigations on non-linear temperature-dependent electro-mechanical response of 1-3 type piezocomposites. *Sensors and Actuators A: Physical*, 201:23 – 35, 2013. 17, 19
- [57] R. Jayendiran and A. Arockiarajan. Modeling and experimental characterization on temperature-dependent ferroelastic switching of 1-3 type piezocomposites. *International*

- Journal of Engineering Science*, 68:61 – 74, 2013. 11
- [58] N. Jeyaganesh, S. Maniprakash, L. Chandrasekaran, S. M. Srinivasan, and A. R. Srinivasa. Design and development of a sun tracking mechanism using the direct SMA actuation. *ASME. J. Mech. Des.*, 133(7):832 – 836, 2011. 3
- [59] M. Kamlah. Ferroelectric and ferroelastic piezoceramics - modeling of electromechanical hysteresis phenomena. *Continuum Mechanics and Thermodynamics*, 13:219–268, 2001. doi:[10.1007/s001610100052](https://doi.org/10.1007/s001610100052). 6, 22, 45
- [60] M. Kamlah and U. Böhle. Finite element analysis of piezoceramic components taking into account ferroelectric hysteresis behavior. *International Journal of Solids and Structures*, 38(4):605–633, 2001. doi:[10.1016/S0020-7683\(00\)00055-X](https://doi.org/10.1016/S0020-7683(00)00055-X). 23, 24
- [61] M. Kamlah and C. Tsakmakis. Phenomenological modeling of the non-linear electro-mechanical coupling in ferroelectrics. *International Journal of Solids and Structures*, 36(5):669–695, 1999. doi:[10.1016/S0020-7683\(98\)00040-7](https://doi.org/10.1016/S0020-7683(98)00040-7). 22
- [62] R. Kar-Gupta and T. Venkatesh. Electromechanical response of 1-3 piezoelectric composites: An analytical model. *Acta Materialia*, 55(3):1093 – 1108, 2007. doi:<http://dx.doi.org/10.1016/j.actamat.2006.09.023>. 25
- [63] R. A. Kellogg, A. B. Flatau, A. E. Clark, M. Wun-Fogle, and T. A. Lograsso. Temperature and stress dependencies of the magnetic and magnetostrictive properties of fe_{0.81}ga_{0.19}. *Journal of Applied Physics*, 91(10), 2002. 97
- [64] S.-J. Kim and Q. Jiang. A finite element model for rate-dependent behavior of ferroelectric ceramics. *International Journal of Solids and Structures*, 39(4):1015 – 1030, 2002. doi:[http://dx.doi.org/10.1016/S0020-7683\(01\)00126-3](http://dx.doi.org/10.1016/S0020-7683(01)00126-3). 21
- [65] S. Klinkel. A phenomenological constitutive model for ferroelastic and ferroelectric hysteresis effects in ferroelectric ceramics. *International Journal of Solids and Structures*, 43(22-23):7197–7222, 2006. doi:[10.1016/j.ijsolstr.2006.03.008](https://doi.org/10.1016/j.ijsolstr.2006.03.008). 23, 24, 45, 46, 63, 65
- [66] E. Koray Akdogan, M. Allahverdi, and A. Safari. Piezoelectric composites for sensor and actuator applications. *IEEE Transactions on Ultrasonics, Ferroelectrics, and Frequency Control*, 52(5):746–775, 2005. doi:[10.1109/TUFFC.2005.1503962](https://doi.org/10.1109/TUFFC.2005.1503962). 14
- [67] H. H. A. Krueger and D. Berlincourt. Effects of high static stress on the piezoelectric properties of transducer materials. *The Journal of the Acoustical Society of America*, 33(10):1339–1344, 1961. 18
- [68] H. H. A. Krueger. Stress sensitivity of piezoelectric ceramics: Part 1. sensitivity to compressive stress parallel to the polar axis. *The Journal of the Acoustical Society of America*, 42(3):636–645, 1967. doi:<http://dx.doi.org/10.1121/1.1910635>. 18
- [69] W.-S. Kuo and J. H. Huang. On the effective electroelastic properties of piezoelectric composites containing spatially oriented inclusions. *International Journal of Solids and Structures*, 34(19):2445 – 2461, 1997. doi:[http://dx.doi.org/10.1016/S0020-7683\(96\)00154-0](http://dx.doi.org/10.1016/S0020-7683(96)00154-0). 25
- [70] C. M. Landis. A new finite-element formulation for electromechanical boundary value problems. *International Journal for Numerical Methods in Engineering*, 55(5):613–628, 2002. doi:[10.1002/nme.518](https://doi.org/10.1002/nme.518). 24

- [71] C. M. Landis and R. M. McMeeking. A phenomenological constitutive law for ferroelastic switching and a resulting asymptotic crack tip solution. *Journal of Intelligent Material Systems and Structures*, 10(2):155–163, 1999. doi:[10.1177/1045389X9901000209](https://doi.org/10.1177/1045389X9901000209). 22
- [72] C. Landis. Fully coupled, multi-axial, symmetric constitutive laws for polycrystalline ferroelectric ceramics. *Journal of the Mechanics and Physics of Solids*, 50(1):127–152, 2002. doi:[10.1016/S0022-5096\(01\)00021-7](https://doi.org/10.1016/S0022-5096(01)00021-7). 23, 46
- [73] D. Li and K. Duan. 1-3 piezocomposite for vibration accelerometer applications. *Ferroelectrics*, 466(1):86–91, 2014. 15
- [74] F. X. Li, R. K. N. D. Rajapakse, D. Mumford, and M. Gadala. Quasi-static thermo-electro-mechanical behaviour of piezoelectric stack actuators. *Smart Materials and Structures*, 17, 2008. 18
- [75] L. Li and N. R. Sottos. Improving hydrostatic performance of 1-3 piezocomposites. *Journal of Applied Physics*, 77(9):4595–4603, 1995. 15
- [76] J. S. Liu, S. R. Zhang, H. Z. Zeng, C. T. Yang, and Y. Yuan. Coercive field dependence of the grain size of ferroelectric films. *Phys. Rev. B*, 72:172101, 2005. doi:[10.1103/PhysRevB.72.172101](https://doi.org/10.1103/PhysRevB.72.172101). 18
- [77] D. C. Lupascu. *Fatigue in Ferroelectric Ceramics and Related Issues*. Springer, 2004. 43, 44, 52
- [78] B. Ma, Z. Hu, S. Liu, M. Narayanan, and U. (Balu) Balachandran. Temperature dependent polarization switching properties of ferroelectric $\text{Pb}_{0.92}\text{La}_{0.08}\text{Zr}_{0.52}\text{Ti}_{0.48}\text{O}_5$ films grown on nickel foils. *Applied Physics Letters*, 102(7):072901, 2013. doi:<http://dx.doi.org/10.1063/1.4793304>. 13, 19, 82
- [79] S. Maniprakash, A. Arockiarajan, and A. Menzel. A multi-surface model for ferroelectric ceramics - application to cyclic electric loading with changing maximum amplitude. *Philosophical Magazine*, 2016. doi:<http://dx.doi.org/10.1080/14786435.2016.1161861>. 42
- [80] S. Maniprakash, R. Jayendiran, A. Menzel, and A. Arockiarajan. Experimental investigation, modelling and simulation of rate-dependent response of 1-3 ferroelectric composites. *Mechanics of Materials*, 94:91 – 105, 2016. doi:<http://dx.doi.org/10.1016/j.mechmat.2015.11.018>. 61
- [81] R. M. McMeeking and S. C. Hwang. On the potential energy of a piezoelectric inclusion and the criterion for ferroelectric switching. *Ferroelectrics*, 200(1):151–173, 1997. doi:[10.1080/00150199708008603](https://doi.org/10.1080/00150199708008603). 20
- [82] R. McMeeking and C. Landis. A phenomenological multi-axial constitutive law for switching in polycrystalline ferroelectric ceramics. *International Journal of Engineering Science*, 40(14):1553–1577, 2002. doi:[10.1016/S0020-7225\(02\)00033-2](https://doi.org/10.1016/S0020-7225(02)00033-2). 23
- [83] T. Michelitsch and W. Kreher. A simple model for the nonlinear material behavior of ferroelectrics. *Acta Materialia*, 46(14):5085 – 5094, 1998. doi:[http://dx.doi.org/10.1016/S1359-6454\(98\)00178-5](http://dx.doi.org/10.1016/S1359-6454(98)00178-5). 20
- [84] C. Miehe and D. Rosato. A rate-dependent incremental variational formulation of ferroelectricity. *International Journal of Engineering Science*, 49:466–496, 2011. 24, 35, 46, 64

- [85] C. Miehe, D. Rosato, and B. Kiefer. Variational principles in dissipative electro-magneto-mechanics: A framework for the macro-modeling of functional materials. *International Journal for Numerical Methods in Engineering*, 86:1225–1276, 2011. 24
- [86] T. Mori and K. Tanaka. Average stress in matrix and average elastic energy of materials with misfitting inclusions. *Acta Metallurgica*, 21(5):571 – 574, 1973. doi:[http://dx.doi.org/10.1016/0001-6160\(73\)90064-3](http://dx.doi.org/10.1016/0001-6160(73)90064-3). 25
- [87] Z. Mroz. On the description of anisotropic work hardening. *Journal of the Mechanics and Physics of Solids*, 15:163–175, 1967. 43
- [88] A. H. Muliana. A micromechanical formulation for piezoelectric fiber composites with nonlinear and viscoelastic constituents. *Acta Materialia*, 58(9):3332 – 3344, 2010. doi:<http://dx.doi.org/10.1016/j.actamat.2010.02.007>. 26
- [89] R. Newnham, D. Skinner, and L. Cross. Connectivity and piezoelectric-pyroelectric composites. *Materials Research Bulletin*, 13(5):525 – 536, 1978. doi:[http://dx.doi.org/10.1016/0025-5408\(78\)90161-7](http://dx.doi.org/10.1016/0025-5408(78)90161-7). 14, 24, 25
- [90] J. Nuffer, D. Lupascu, and J. Roedel. Damage evolution in ferroelectric {PZT} induced by bipolar electric cycling. *Acta Materialia*, 48(14):3783 – 3794, 2000. ISSN 1359-6454. doi:[http://dx.doi.org/10.1016/S1359-6454\(00\)00173-7](http://dx.doi.org/10.1016/S1359-6454(00)00173-7). 43
- [91] G. Odegard. Constitutive modeling of piezoelectric polymer composites. *Acta Materialia*, 52(18):5315 – 5330, 2004. doi:<http://dx.doi.org/10.1016/j.actamat.2004.07.037>. 26
- [92] S.-E. Park and T. R. Shrout. Relaxor based ferroelectric single crystals for electro-mechanical actuators. *Material Research Innovations*, 1(1):20–25, 1997. doi:[10.1007/s100190050014](http://dx.doi.org/10.1007/s100190050014). 20
- [93] H. E. Pettermann and S. Suresh. A comprehensive unit cell model: a study of coupled effects in piezoelectric 1-3 composites. *International Journal of Solids and Structures*, 37(39):5447 – 5464, 2000. doi:[http://dx.doi.org/10.1016/S0020-7683\(99\)00224-3](http://dx.doi.org/10.1016/S0020-7683(99)00224-3). 26
- [94] C. Poizat and M. Sester. Effective properties of composites with embedded piezoelectric fibres. *Computational Materials Science*, 16(1-4):89 – 97, 1999. doi:[http://dx.doi.org/10.1016/S0927-0256\(99\)00050-6](http://dx.doi.org/10.1016/S0927-0256(99)00050-6). 25
- [95] K. S. Ramadan, D. Sameoto, and S. Evoy. A review of piezoelectric polymers as functional materials for electromechanical transducers. *Smart Materials and Structures*, 23(3):033001, 2014. 15
- [96] J. Rödel and W. S. Kreher. Self-consistent modelling of non-linear effective properties of polycrystalline ferroelectric ceramics. *Computational Materials Science*, 19(1-4):123 – 132, 2000. doi:[http://dx.doi.org/10.1016/S0927-0256\(00\)00147-6](http://dx.doi.org/10.1016/S0927-0256(00)00147-6). 21
- [97] J. Rödel and W. S. Kreher. Modelling linear and nonlinear behavior of polycrystalline ferroelectric ceramics. *Journal of the European Ceramic Society*, 23(13):2297 – 2306, 2003. doi:[http://dx.doi.org/10.1016/S0955-2219\(03\)00084-0](http://dx.doi.org/10.1016/S0955-2219(03)00084-0). 21
- [98] D. Schrade, R. Mueller, B. Xu, and D. Gross. Domain evolution in ferroelectric materials: A continuum phase field model and finite element implementation. *Computer Methods in Applied Mechanics and Engineering*, 196(41-44):4365 – 4374, 2007. 21

- [99] J. Schröder and D. Gross. Invariant formulation of the electromechanical enthalpy function of transversely isotropic piezoelectric materials. *Archive of Applied Mechanics*, 73: 533–552, 2004. doi:[10.1007/s00419-003-0294-5](https://doi.org/10.1007/s00419-003-0294-5). 23
- [100] J. Schröder and H. Romanowski. A thermodynamically consistent mesoscopic model for transversely isotropic ferroelectric ceramics in a coordinate-invariant setting. *Archive of Applied Mechanics*, 74:863–877, 2005. doi:[10.1007/s00419-005-0412-7](https://doi.org/10.1007/s00419-005-0412-7). 23, 46
- [101] K. Schulgasser. Relationships between the effective properties of transversely isotropic piezoelectric composites. *Journal of the Mechanics and Physics of Solids*, 40(2):473 – 479, 1992. doi:[http://dx.doi.org/10.1016/S0022-5096\(05\)80022-5](http://dx.doi.org/10.1016/S0022-5096(05)80022-5). 24
- [102] M. Senousy, R. Rajapakse, and M. Gadala. A temperature-dependent two-step domain-switching model for ferroelectric materials. *Acta Materialia*, 57(20):6135 – 6145, 2009. doi:<http://dx.doi.org/10.1016/j.actamat.2009.08.039>. 18
- [103] O. Sigmund and S. Torquato. Design of smart composite materials using topology optimization. *Smart Materials and Structures*, 8:365–379, 1999. 25
- [104] O. Sigmund, S. Torquato, and I. A. Aksay. On the design of 1-3 piezocomposites using topology optimization. *Journal of Materials Research*, 13:1038–1048, 1998. doi:[10.1557/JMR.1998.0145](https://doi.org/10.1557/JMR.1998.0145). 15
- [105] E. C. N. Silva, J. S. O. Fonseca, and N. Kikuchi. Optimal design of periodic piezocomposites. *Computer Methods in Applied Mechanics and Engineering*, 159(1-2):49 – 77, 1998. doi:[http://dx.doi.org/10.1016/S0045-7825\(98\)80103-5](http://dx.doi.org/10.1016/S0045-7825(98)80103-5). 25
- [106] J. Simo and T. Hughes. *Computational Inelasticity*. Springer-Verlag, New-York, 1998. 24
- [107] W. Smith. Modeling 1-3 composite piezoelectrics: hydrostatic response. *IEEE Transactions on Ultrasonics, Ferroelectrics, and Frequency Control*, 40(1):41–49, 1993. doi:[10.1109/58.184997](https://doi.org/10.1109/58.184997). 25
- [108] W. Smith and B. Auld. Modeling 1-3 composite piezoelectrics: thickness-mode oscillations. *IEEE Transactions on Ultrasonics, Ferroelectrics, and Frequency Control*, 38(1): 40–47, 1991. doi:[10.1109/58.67833](https://doi.org/10.1109/58.67833). 24
- [109] R. Steinhausen, T. Hauke, W. Seifert, H. Beige, W. Watzka, S. Seifert, D. Sporn, S. Starke, and A. Schönecker. Finescaled piezoelectric 1-3 composites: properties and modeling. *Journal of the European Ceramic Society*, 19(6-7):1289 – 1293, 1999. doi:[http://dx.doi.org/10.1016/S0955-2219\(98\)00422-1](http://dx.doi.org/10.1016/S0955-2219(98)00422-1). 19
- [110] M. Stewart, M. Cain, and D. Hall. Ferroelectric hysteresis measurement and analysis. *NPL-R-CMMT/A-152*, 1999. doi:[NPL-R-CMMT/A-152](https://doi.org/10.1016/NPL-R-CMMT/A-152). 17
- [111] Y. Su and C. M. Landis. Continuum thermodynamics of ferroelectric domain evolution: Theory, finite element implementation, and application to domain wall pinning. *Journal of the Mechanics and Physics of Solids*, 55(2):280 – 305, 2007. 21
- [112] E. C. Subbarao, M. C. McQuarrie, and W. R. Buessem. Domain effects in polycrystalline barium titanate. *Journal of Applied Physics*, 28(10):1194–1200, 1957. 18
- [113] K. F. Takeo Furukawa and E. Fukada. Electromechanical properties in the composites of epoxy resin and PZT ceramics. *Japanese Journal of Applied Physics*, 15:2119–2129,

1976. [19](#)
- [114] S. Timoshenko. *Theory of Elasticity*. Engineering Societies Monographs. McGraw-Hill, 1951. [29](#)
- [115] R. Y. Ting, A. a. Shaulov, and W. A. Smith. Evaluation of the properties of 1-3 piezocomposites of a new lead titanate in epoxy resins. *Ferroelectrics*, 132(1):69–77, 1992. [15](#)
- [116] M. Uludogan and T. Cagin. First principles approach to BaTiO₃. *Turkish Journal of Physics*, 30(4), 2006. [19](#)
- [117] K. Webber, E. Aulbach, T. Key, M. Marsilius, T. Granzow, and J. Roedel. Temperature-dependent ferroelastic switching of soft lead zirconate titanate. *Acta Materialia*, 57(15):4614–4623, 2009. doi:<http://dx.doi.org/10.1016/j.actamat.2009.06.037>. [18](#)
- [118] R. B. Williams, G. Park, D. J. Inman, and W. K. Wilkie. An overview of composite actuators with piezoceramic fibers. *Proceeding of IMAC XX*, pages 4–7, 2002. [14](#)
- [119] B. Xu, D. Schrade, R. Mueller, and D. Gross. Micromechanical analysis of ferroelectric structures by a phase field method. *Computational Materials Science*, 45(3):832 – 836, 2009. [21](#)
- [120] G. Zhang and M. Wu. Connectivity and shape effects on the effective properties of piezoelectric-polymeric composites. *International Journal of Engineering Science*, 48(1):37 – 51, 2010. doi:<http://dx.doi.org/10.1016/j.ijengsci.2009.06.006>. [26](#)
- [121] W. Zhang and K. Bhattacharya. A computational model of ferroelectric domains. part i: model formulation and domain switching. *Acta Materialia*, 53(1):185 – 198, 2005. [21](#)
- [122] W. Zhang and K. Bhattacharya. A computational model of ferroelectric domains. part ii: grain boundaries and defect pinning. *Acta Materialia*, 53(1):199 – 209, 2005. [21](#)
- [123] Z. Zhao, V. Buscaglia, M. Viviani, M. T. Buscaglia, L. Mitoseriu, A. Testino, M. Nygren, M. Johnsson, and P. Nanni. Grain-size effects on the ferroelectric behavior of dense nanocrystalline batio₃ ceramics. *Phys. Rev. B*, 70:024107, Jul 2004. doi:[10.1103/PhysRevB.70.024107](http://dx.doi.org/10.1103/PhysRevB.70.024107). [18](#)
- [124] D. Zhou. Experimental investigation of non-linear constitutive behaviour of PZT piezoceramics. *Ph.D. Thesis, Universitaet Karlsruhe*, 2003. [9](#), [10](#), [11](#), [17](#), [19](#), [69](#), [70](#), [71](#)
- [125] D. Zhou, M. Kamlah, and D. Munz. Rate dependence of soft PZT ceramics under electric field loading. *Proc. SPIE*, 4333:64–70, 2001. [12](#)
- [126] D. Zhou, M. Kamlah, and D. Munz. Effects of uniaxial prestress on the ferroelectric hysteretic response of soft PZT. *Journal of the European Ceramic Society*, 25(4):425 – 432, 2005. doi:<http://dx.doi.org/10.1016/j.jeurceramsoc.2004.01.016>. [18](#)
- [127] D. Zhou, M. Kamlah, and B. Laskewitz. Multi-axial non-proportional polarization rotation tests of soft PZT piezoceramics under electric field loading. *Proc. SPIE*, 6170:617009–617009–9, 2006. [65](#), [72](#), [73](#)

Curriculum Vitae

Personal Data

Name	Maniprakash Subramanian
Date of Birth	June 10, 1985
Place of Birth	Karur, India
Nationality	Indian

Professional Occupation

10/2011 – onwards	Scientific Assistant, Institute of Mechanics, TU Dortmund University
09/2009 – 07/2011	Development Manager, Tatamotors corporation Ltd, Pune, India, Chassis design Department
05/2009 – 08/2009	Project associate, Applied Mechanics, IIT Madras, Chennai

University Education

06/2009	Master of Technology, Applied Mechanics, IIT Madras
05/2007	Bachelor of Engineering, Mechanical Engineering Department, Anna University, Chennai

School Education

06/2003	Higher Secondary School Certificate, Sri kamakshi Vidyalaya Matriculation School, Thoothukudi
---------	---

